POLITECNICO DI TORINO

Corso di Laurea Magistrale in Ingegneria Energetica e Nucleare

Tesi di Laurea Magistrale

Assessment of Hydrogen Embrittlement Susceptibility in Nickel 725 Under Various Surface Conditions

Relatore

Prof. Xu Lu (NTNU)
Prof. Massimo Santarelli
Prof. Yiliu Liu (NTNU)
Mr. Kerem Can Dizdar (NTNU)

Laureando

Mohamed Aseem Shazahan

LUGLIO 2026

Mohamed Aseem Shazahan

Assessment of Hydrogen Embrittlement Susceptibility in Ni 725 Under Various Surface Conditions

Master's thesis in Mechanical and Industrial Engineering
Supervisor: Xu Lu
Co-supervisor: Massimo Santarelli (PoliTo), Yiliu Liu, Kerem Can Dizdar
June 2026

Norwegian University of Science and Technology
Department of Mechanical and Industrial Engineering
Faculty of Engineering

NTNU

ABSTRACT

This thesis investigates the influence of surface condition on hydrogen embrittlement (HE) susceptibility in Ni 725 under controlled electrochemical cathodic charging. Five surface conditions were evaluated: a 2000-grit ground reference, EDM-finished, peened, gold-sputtered, and electrodeposited nickel-coated specimens; the latter was deposited at 50 °C and a current density of 0.15 A/cm^2. Specimens were pre-charged for 24 h in a glycerol–phosphoric acid electrolyte at 50 °C, with an additional 72 h condition applied to the ground reference to assess the effect of extended hydrogen exposure. Mechanical behaviour was characterised by in-situ tensile testing inside a scanning electron microscope (SEM). Hydrogen charging significantly reduced ductility across all conditions. The ground reference showed a fracture strain of 35.99% in air, dropping to 16.01% after 24 h and 9.35% after 72 h charging. Among the 24 h conditions, the electrodeposited Ni-coated specimen exhibited the most severe embrittlement, with a fracture strain of 10.73% and the highest hydrogen content by thermal desorption spectrometry (56.83 wppm) approximately twice that of the uncoated specimens. The EDM and gold-sputtered specimens retained the highest ductility after charging (21% elongation), while the shot-peened specimen showed intermediate behaviour. Brittle zone depth measurements showed hydrogen penetration depths of 70–89 µm for all 24 h conditions, with surface condition primarily governing the spatial uniformity of hydrogen entry rather than the total depth. Fractographic and EDS analyses identified quasi-cleavage and intergranular fracture as the dominant failure modes, consistent with combined HEDE and HELP mechanisms. The results show that the electrodeposited Ni coating acted as a hydrogen reservoir rather than a protective barrier under the conditions tested.

PREFACE

This master's thesis is submitted to Politecnico di Torino as a part of the Master's degree in Energy and Nuclear Engineering at the Department of Energy. The work included in this thesis was carried out with the Materials & Manufacturing Group, Department of Mechanical and Industrial Engineering, Norwegian University of Science and Technology (NTNU). Professor Xu Lu has supervised this work with Professor Massimo Santarelli (PoliTo), Yiliu Liu (NTNU), and Kerem Can Dizdar (NTNU) as co-supervisors.

I would like to express my sincere gratitude to my supervisors for generously sharing their expertise and for always making time for both brief consultations and in-depth discussions throughout the semester. Their continuous guidance, support, and regular meetings kept me motivated and significantly contributed to improving the quality of this work.

I would like to express my deepest gratitude to my parents and my family for their unconditional support throughout my studies and during this thesis work. I am also sincerely grateful to my friend and mentor, Alessio Arrighini, for his constant encouragement and guidance throughout my studies. Lastly, I would like to express my sincere gratitude to the HySET Erasmus Mundus Consortium at Politecnico di Torino for their continuous support and encouragement throughout the Master's degree.

Mohamed Aseem Shazahan

Contents

List of Figures

List of Tables

ABBREVIATIONS

List of all abbreviations in alphabetic order:

- **BCC** Body-Centered Cubic (crystal structure)
- **c-BN** Cubic boron nitride
- **CMSX-4** Single-crystal Ni-based superalloy CMSX-4
- **Co-Cr** Cobalt–chromium alloys
- **CVD** Chemical Vapor Deposition
- **D** Diffusion coefficient (hydrogen)
- **DED** Directed Energy Deposition
- **DLC** Diamond-Like Carbon
- **Ea** Activation energy for diffusion
- **FCC** Face-Centered Cubic (crystal structure)
- **GB** Grain boundary
- **H** Atomic hydrogen
- **H_2** Molecular hydrogen
- **HE** Hydrogen embrittlement
- **HEDE** Hydrogen Enhanced Decohesion
- **HE index** Hydrogen embrittlement index (ductility-loss based)
- **HELP** Hydrogen Enhanced Localized Plasticity
- **HESIV** Hydrogen-Enhanced Strain-Induced Vacancy formation
- **HISC** Hydrogen-Induced Stress Cracking
- **HVOF** High Velocity Oxy-Fuel (thermal spraying)
- **J** Hydrogen flux

- **KAM** Kernel Average Misorientation
- **Ni** Nickel
- **Ni725** Nickel alloy 725 (Alloy 725)
- **NiAl** Nickel aluminide (-NiAl phase)
- **NiP** Electroless nickel–phosphorus coating
- **Ni-Zn-P** Nickel–zinc–phosphorus amorphous coating
- **PVD** Physical Vapor Deposition
- **PS-PVD** Plasma Spray–Physical Vapor Deposition
- **PRF** Permeation Reduction Factor
- **R** Universal gas constant
- **S** Solubility of hydrogen
- **SEM** Scanning Electron Microscopy / Microscope
- **SiC** Silicon carbide
- **SiN** Silicon nitride
- **SSRT** Slow Strain Rate Testing
- **STP** Standard Temperature and Pressure
- **T** Absolute temperature
- **TiAlN** Titanium aluminium nitride
- **TiMoN** Titanium molybdenum nitride
- **TiN** Titanium nitride
- **UTS** Ultimate Tensile Strength
- **YS** Yield Strength

CHAPTER

ONE

INTRODUCTION

The transition towards a hydrogen-based energy infrastructure has intensified the demand for structural materials capable of operating reliably in hydrogen-rich environments. Nickel-based alloys remain the primary material choice for critical offshore components fasteners, connectors, and wellbore completion hardware for their superior resistance to hydrogen-induced stress cracking (HISC), pitting, and crevice corrosion in chloride-rich environments [1, 2]. Hydrogen embrittlement (HE) remains one of the most critical material integrity challenges for nickel-based alloys deployed in hydrogen-rich environments from subsea oil and gas infrastructure to nuclear fusion reactors, hydrogen transport pipelines, and gas turbine components [3].

Hydrogen embrittlement occurs when atomic hydrogen enters the metallic lattice, diffuses through it, and accumulates at microstructural features such as dislocations, grain boundaries, inclusions, and phase interfaces [4]. This promotes crack nucleation and propagation at stress levels that would otherwise be safe. The interaction between hydrogen transport, microstructure, and stress remains complex and material-dependent, and no single universal mechanism fully describes the process in all alloys [5].

1.1 Motivation

Nickel alloys have inherently lower hydrogen diffusivity than ferritic steels due to their face-centred cubic lattice structure. They are not, however, immune to hydrogen embrittlement, particularly at grain boundaries in precipitation-hardened conditions [6, 7].

Barrier coatings, both metallic and ceramic are a common engineering strategy to reduce hydrogen ingress [8]. Recent work shows that the near-surface region, including its roughness, residual stress state, and interfacial microstructure, strongly influences how much hydrogen enters and where it is trapped [9]. Surface engineering has therefore become an important approach to reduce hydrogen-induced degradation without changing the bulk alloy composition. Metal-based surface deposition offers particular advantages: localised microstructural modification, good

metallurgical bonding, and the potential to act as a hydrogen diffusion barrier [10].

Beyond coatings, the condition of the substrate surface itself plays a decisive role in governing hydrogen ingress, trapping, and crack initiation [11]. The manufacturing or finishing route produces a characteristic near-surface layer with a specific roughness, residual stress, dislocation density, and defect population, all of alters the hydrogen adsorption mechanism at the atomic scale [12]. Rougher or more damaged surfaces provide a higher density of entry sites and shallow traps, which can accelerate the onset of embrittlement compared with smoother, compressively stressed, or chemically passivated surfaces [13].

This thesis considers five surface conditions. Grinding to 2000-grit SiC produced a smooth reference surface with shallow deformation and serves as the baseline for all comparisons. Electrical discharge machining (EDM) produced a thermally affected recast layer with elevated tensile residual stress and a high microcrack density.Surface Peening using an IEPCO Peenmatic 750 system introduced a compressive residual stress field and a high near-surface dislocation density. Gold sputter coating was used to deposit a thin noble-metal layer with intrinsically low hydrogen solubility, representing a surface-level permeation barrier. Finally, electrodeposited nickel coating is applied as the primary surface treatment of interest, intended to act as a hydrogen diffusion barrier. By comparing the tensile response and hydrogen-induced ductility loss across these conditions, the thesis aims to separate the contributions of surface state, residual stress, surface chemistry, and coating architecture to the overall HE susceptibility of Ni 725.

Taken together, the available literature highlights a lack of systematic studies directly linking surface condition, hydrogen exposure, and fracture behaviour in Ni 725. This thesis addresses that gap by combining controlled electrochemical hydrogen pre-charging with in-situ tensile testing inside an SEM and post-mortem microstructural characterisation (SEM, EDS, FIB, and TDS) to establish structure–property–hydrogen interaction relationships and to evaluate whether common surface treatments and metallic coatings can enhance or reduce resistance to hydrogen-induced degradation.

1.2 Project Description

This project systematically investigates the hydrogen embrittlement behaviour of Ni 725 and evaluates the effectiveness of an electrodeposited nickel coating as a surface engineering strategy to mitigate hydrogen-induced degradation. Five surface conditions were studied: a 2000-grit ground reference, EDM-finished, Peened, gold-sputtered, and electrodeposited Ni-coated specimens. Both coated and uncoated specimens were electrochemically pre-charged in a glycerol–phosphoric acid electrolyte at 50 °C for 24 h. The ground reference was also tested after 72 h hydrogen charging to capture the effect of extended hydrogen exposure. Air-tested (uncharged) specimens were produced for the ground, EDM and shot-peened conditions to serve as mechanical baselines.

Mechanical performance was evaluated through in-situ slow-strain-rate tensile testing inside a scanning electron microscope (SEM), which allowed direct observation of crack initiation and surface damage during loading. Key parameters extracted from the stress–strain curves include yield strength, ultimate tensile strength (UTS), fracture strain, and the hydrogen embrittlement index I_{HE}.

To understand the underlying damage mechanisms, a range of characterisation techniques was employed. Fractographic analysis by SEM identified the transition from ductile dimple fracture to quasi-cleavage and intergranular failure with increasing hydrogen exposure. EDS cross-section mapping on FIB-prepared cross-sections revealed the near-surface elemental state of the EDM and peened conditions after charging. Brittle zone depth measurements from SEM overview images provided a quantitative estimate of hydrogen penetration depth across all surface conditions. Thermal desorption spectrometry (TDS) was used on selected specimens to measure the total extractable hydrogen content retained after charging and tensile testing. These observations are used together to identify the operative hydrogen-assisted damage mechanisms primarily HELP and HEDE and to relate them to the surface condition and charging history of each specimen.

CHAPTER

TWO

THEORY

2.1 Hydrogen Embrittlement

Hydrogen embrittlement (HE) is the loss of ductility, toughness, or fracture resistance in a metal due to the ingress, diffusion, and accumulation of hydrogen, leading to premature crack initiation and brittle or quasi-brittle fracture under stresses that would otherwise be safely carried [14, 15]. In practical terms, a hydrogen-embrittled component fails at lower strain and with a more brittle fracture morphology than a hydrogen-free component of the same alloy, geometry, and loading condition. The phenomenon spans length scales from the atomic (hydrogen–lattice interactions) to the structural (macroscopic cracking), and it depends sensitively on microstructure, stress state, environment, and surface condition [14].

For austenitic and precipitation-hardened nickel-based alloys such as Ni 725, HE typically manifests as a reduction in uniform elongation, formation of secondary surface cracks, and the appearance of quasi-cleavage and intergranular facets in the fracture surface when the alloy is exposed to hydrogen-rich environments under stress [16]. Although Ni alloys have intrinsically lower hydrogen diffusivity than ferritic steels, they remain susceptible to hydrogen-induced stress cracking (HISC) and delayed failure, particularly at grain boundaries and precipitate interfaces under cathodic protection or high-pressure hydrogen service [14, 17].

At a mechanistic level, HE normally occurs if three conditions are satisfied:

- **Hydrogen entry**: atomic hydrogen is generated at the surface by electrochemical or gaseous reactions and is absorbed into the metal.
- **Hydrogen transport and trapping**: hydrogen diffuses and is trapped at microstructural defects in regions of high stress or plastic strain.
- **Hydrogen–mechanics interaction**: hydrogen alters the local mechanical response via mechanisms such as Hydrogen-Enhanced Localised Plasticity (HELP), Hydrogen-Enhanced Decohesion (HEDE), Hydrogen-Enhanced Strain-Induced Vacancy formation (HESIV), or Adsorption-Induced Dislocation Emission (AIDE) [18, 14].

2.2 Hydrogen Uptake in Metals

Hydrogen enters a metallic lattice through two principal routes depending on the service environment: gaseous uptake from high-pressure molecular hydrogen or hydrocarbon gases, and electrochemical uptake from an aqueous electrolyte under cathodic polarisation [14]. Both routes deliver the same species to the lattice—atomic hydrogen, H_{abs} but their kinetics, surface coverage, and dependence on environmental variables differ substantially. In gaseous environments, molecular H_2 first physisorbs and then dissociatively chemisorbs on the metal surface:

$$H_2 \longrightarrow 2\,H_{ads} \tag{2.1}$$

The adsorbed hydrogen atoms then undergo absorption, entering from surface-adsorbed states into subsurface interstitial sites [19]:

$$H_{ads} \longrightarrow H_{abs} \tag{2.2}$$

The absorbed hydrogen concentration is then set by Sievert's law, $C_s = K_S\sqrt{p_{H_2}}$, where K_S is the Sievert constant and H_2 is the partial pressure of hydrogen gas [14]. While this relationship applies directly to bulk materials exposed to high-pressure gaseous hydrogen, such as the carbon steel walls of pipelines and storage vessels. In nickel-based alloys such as Ni 725, where hydrogen ingress occurs primarily via cathodic protection-driven electrochemical charging or by solid-state diffusion of atomic hydrogen from adjacent steel members rather than through direct gaseous exposure [20]. In electrochemical environments, hydrogen entry proceeds through a sequence of reduction reactions collectively described by the Volmer–Tafel–Heyrovsky mechanism [21]. The discussion below is therefore focused on this pathway; however, the subsequent transport and trapping framework (Section 2.3.3) applies equally to both entry routes.

2.2.1 Surface Electrochemical Reactions: Volmer, Heyrovsky, and Tafel Steps

Hydrogen entry into a metallic material from an aqueous environment is governed by a sequence of interfacial electrochemical steps that occur at the metal surface before any bulk diffusion takes place. The overall process can be divided into three stages: (i) transport of protons or water molecules to the surface, (ii) electrochemical reduction and adsorption of atomic hydrogen, and (iii) subsurface absorption and entry into the lattice. The competition between surface recombination and absorption at step (iii) is the main factor controlling the steady-state hydrogen flux into the material under cathodic polarisation [22, 23]. In an acidic or near-neutral aqueous electrolyte, hydrogen entry begins with the Volmer discharge step, in which a proton from solution is reduced at the metal surface to produce an adsorbed hydrogen atom H_{ads}:

$$H^+ + e^- \rightarrow H_{ads} \tag{2.3}$$

Once adsorbed, the surface hydrogen either recombines to evolve molecular gas or is absorbed into the subsurface lattice. Recombination may proceed via two

competing pathways. In the electrochemical Heyrovsky step, an adsorbed atom reacts with a second proton and electron:

$$H_{ads} + H^+ + e^- \rightarrow H_2 \tag{2.4}$$

Alternatively, in the chemical Tafel step two adsorbed atoms combine:

$$H_{ads} + H_{ads} \rightarrow H_2 \tag{2.5}$$

Whereas, in alkaline environments ($pH > 7$), the proton donor changes from H^+ to water, since the concentration of free protons is negligible at high pH [24, 25]. The Volmer step accordingly becomes:

$$H_2O + e^- \rightarrow H_{ads} + OH^- \tag{2.6}$$

Similarly, the alkaline Heyrovsky step involves water as the proton source:

$$H_{ads} + H_2O + e^- \rightarrow H_2 + OH^- \tag{2.7}$$

The Tafel recombination step (2.5) is unchanged, as it involves no proton transfer. The net consequence of the alkaline pathway is that water dissociation introduces an additional energy barrier, making the overall reaction kinetics significantly slower than in acidic media [25, 26]. For cathodic charging experiments conducted in near-neutral glycerol–H_3PO_4 electrolyte, contributions from both the acidic and alkaline pathways may be active depending on the local pH at the electrode surface.

The dominant pathway depends on the applied potential and the fractional surface coverage θ_H. In acidic and near-neutral solutions, at low θ_H the Volmer–Tafel sequence dominates; as θ_H increases the Volmer–Heyrovsky route becomes preferred [27]. In alkaline media, however, the need to split water in the Volmer step introduces an additional kinetic barrier, so the Volmer step often becomes rate-determining and the relative importance of the Tafel and Heyrovsky pathways can differ from the acidic case [25, 26]. For nickel and its alloys under cathodic charging conditions relevant to this study (glycerol–H_3PO_4 electrolyte, 50 °C), surface coverage is the key variable linking the applied current density to the subsurface hydrogen concentration [28]. The rate of absorption is proportional to θ_H and is additionally influenced by the local surface stress, which lowers the chemical potential of hydrogen [23].

Surface condition profoundly alters the effective hydrogen uptake rate through the following effects. First, a rougher or more defective surface presents a larger real contact area per unit projected area, increasing the total number of active Volmer sites and therefore the absorbed flux at any given nominal current density [22]. Second, near-surface lattice damage dislocations, vacancies, and grain-boundary intersections provides a high density of reversible traps immediately beneath the entry surface, effectively increasing the local solubility and reducing the apparent activation barrier for absorption [28, 23].

2.3 Hydrogen Diffusion and Trapping in Metals

Once absorbed beneath the surface, hydrogen migrates through the crystal lattice by thermally activated diffusion and interacts with microstructural features that can temporarily or permanently immobilise it [7]. The macroscopic transport behaviour is described by Fick's laws, while trapping theory accounts for the retardation introduced by microstructural defects.

2.3.1 Fick's Laws and Permeability

The fundamental description of hydrogen movement down a concentration gradient is given by Fick's First Law:

$$J = -D\frac{dC}{dx} \tag{2.8}$$

where J is the hydrogen flux ($\mathrm{mol\,m^{-2}s^{-1}}$), D is the diffusion coefficient ($\mathrm{m^2\,s^{-1}}$), and dC/dx is the concentration gradient. The negative sign indicates diffusion from regions of higher to lower concentration. Under non-steady-state conditions such as the initial charging transient or post-charge hydrogen redistribution during tensile testing Fick's Second Law governs the evolution of the concentration profile:

$$\frac{\partial C}{\partial t} = D\frac{\partial^2 C}{\partial x^2} \tag{2.9}$$

The overall capacity of a material to transmit hydrogen is quantified by the permeability Φ, defined as the product of the diffusion coefficient and the equilibrium solubility S:

$$\Phi = D \cdot S \tag{2.10}$$

A material with low Φ is an effective hydrogen barrier even if D alone is moderate, provided S is also low. In the context of surface coatings for hydrogen embrittlement mitigation, reducing Φ is the primary design objective; reducing D (kinetic barrier) and S (thermodynamic barrier) are the two independent levers available [29].

2.3.2 Temperature Dependence: Arrhenius Relationship

Both D and S depend strongly on temperature. The diffusion coefficient follows an Arrhenius relationship:

$$D = D_0 \exp\left(-\frac{E_a}{RT}\right) \tag{2.11}$$

where D_0 is the pre-exponential factor, E_a is the activation energy for diffusion, R is the universal gas constant ($8.314\,\mathrm{J\,mol^{-1}\,K^{-1}}$), and T is the absolute temperature. A higher E_a implies slower diffusion at a given temperature. In nickel-based alloys, alloying elements and microstructural features such as γ'' precipitates and grain boundaries increase E_a relative to pure Ni, thereby reducing hydrogen mobility [27, 30].

2.3.3 Trapping: Reversible and Irreversible Sites

Alloys, in reality contain a spectrum of microstructural features grain boundaries, dislocations, vacancies, precipitates, and inclusions that interact with diffusing hydrogen [31]. These features are classified as trapping sites, which retard the effective transport of hydrogen beyond the predictions of simple lattice diffusion [22]. Trapping sites are broadly categorised by the binding energy E_b between the trap and a hydrogen atom:

- **Reversible (weak) traps** ($E_b \lesssim 30$ kJ/mol): Dislocations, elastic stress fields, and low-angle grain boundaries [32]. Hydrogen at these sites is in quasi-equilibrium with the lattice and is released upon unloading or at moderately elevated temperature (typically 50–200 °C), as evidenced by low-temperature desorption peaks in thermal desorption spectroscopy [33, 34]. The effective diffusion coefficient in the presence of reversible traps is given by the Oriani relation [22]:

$$D_{\text{eff}} = \frac{D_L}{1 + K_T} \tag{2.12}$$

  where D_L is the lattice diffusion coefficient and $K_T = N_T/N_L \cdot \exp(E_b/RT)$ is the trapping parameter (N_T and N_L are the trap and lattice site densities, respectively).

- **Irreversible (strong) traps** ($E_b \gtrsim 60$ kJ/mol): Carbides, nitrides, incoherent precipitates, and oxide inclusions are major causes for stronger traps [32]. Hydrogen bound at irreversible sites remains permanently trapped and does not contribute to crack-driving hydrogen flux [35, 28].

The interplay between diffusion and trapping has been noted to be particularly important during loading: as plastic strain accumulates, dislocation density increases, enhancing reversible trap density and locally concentrating hydrogen at regions of highest stress triaxiality [36].

2.3.4 Hydrogen Diffusion & Trapping in Nickel Alloys

Nickel and its alloys crystallise in the face-centred cubic (FCC) structure. The close-packed FCC lattice presents a higher energy barrier to interstitial migration than the more open body-centred cubic (BCC) structure of ferritic steels, resulting in hydrogen diffusion coefficients in Ni alloys that are typically four to six orders of magnitude lower than in low-alloy steels [37, 30]. Table 2.3.1 summarises published hydrogen transport data for common Ni-based alloys. The strong dependence on microstructural condition is evident: precipitation-hardened Inconel 718 shows a diffusion coefficient roughly 50–60% lower than the solutionised form, reflecting the additional trapping provided by the fine γ'' precipitate dispersion [38]. Ni 725, which shares the same γ'' strengthening mechanism and a similar Ni–Cr–Mo–Nb chemistry (Table 2.3.2), is expected to behave analogously: the high density of γ'' and δ-phase precipitates at grain boundaries provides strong reversible trapping sites, promoting local accumulation of hydrogen in the vicinity of grain boundaries, where environmentally assisted cracking can initiate [39].

Table 2.3.1: Baseline hydrogen transport properties of nickel-based alloys.

Alloy	Diffusion / Permeability Data	Temp.	Condition	Ref.
Pure Ni	$D \approx 5 \times 10^{-11}$ m^2/s	RT	Polycrystalline	[40]
Inconel 718 (solutionised)	$D = 5.3$–6.8×10^{-11} cm^2/s	RT	Solutionised	[38]
Inconel 718 (aged)	$D = 2.1$–2.9×10^{-11} cm^2/s	RT	Precipitation hardened	[38]
Inconel 625	$D = 1.81$–2.86×10^{-15} m^2/s	10–23 °C	Cathodic protection	[41]
Incoloy 800H	$\Phi_0 = 0.359$ $_{\mathrm{cm^3(STP)\,cm^{-1}\,s^{-1}\,atm^{-1/2}}}$; $E_a = 21.6$ kcal/mol	700–950 °C	Gaseous H_2	[42]
Inconel 617	∼50% higher Φ than 800H	700–950 °C	Gaseous H_2	[42]

Table 2.3.2: Major chemical composition of common nickel-based alloys (wt%).

Alloy	Major composition (wt%)
Ni 725	Ni (balance, ∼55–59), Cr (19–21.5), Fe (9–11), Mo (7–9), Nb+Ta (4–5), Ti (1–1.7), Al (0.2–0.35) [43]
Inconel 718	Ni (50–55), Cr (17–21), Fe (balance, ∼18), Nb (4.75–5.5), Mo (2.8–3.3), Ti (0.65–1.15), Al (0.2–0.8) [44]
Incoloy 903	Fe (∼40), Ni (∼38), Co (∼15), Nb (∼3), Ti (∼1.5) [45]
Inconel 625	Ni (∼58), Cr (20–23), Mo (8–10),Nb (3–4), Fe (<5) [46]

2.4 Hydrogen Embrittlement Mechanisms

Despite decades of research, hydrogen embrittlement in metallic alloys is not governed by a single universal mechanism. Four distinct mechanistic models HELP, HEDE, HESIV, and AIDE have each accumulated substantial experimental support, and in precipitation- hardened nickel alloys such as Alloy 725, all four may operate simultaneously depending on the local hydrogen concentration, stress state, temperature, and deformation history [30, 47]. The integrated, multiscale nature of HE is illustrated schematically in Figure 2.4.1.

2.4.1 HELP: Hydrogen-Enhanced Localised Plasticity

The HELP mechanism, first articulated by Beachem (1972) [49] and developed in detail by Birnbaum et al. [36], proposes that dissolved hydrogen increases dislocation mobility rather than suppressing it. The physical basis lies in hydrogen's elastic shielding effect: hydrogen atmospheres segregated to dislocation stress fields reduce the repulsive elastic interaction between neighbouring dislocations,

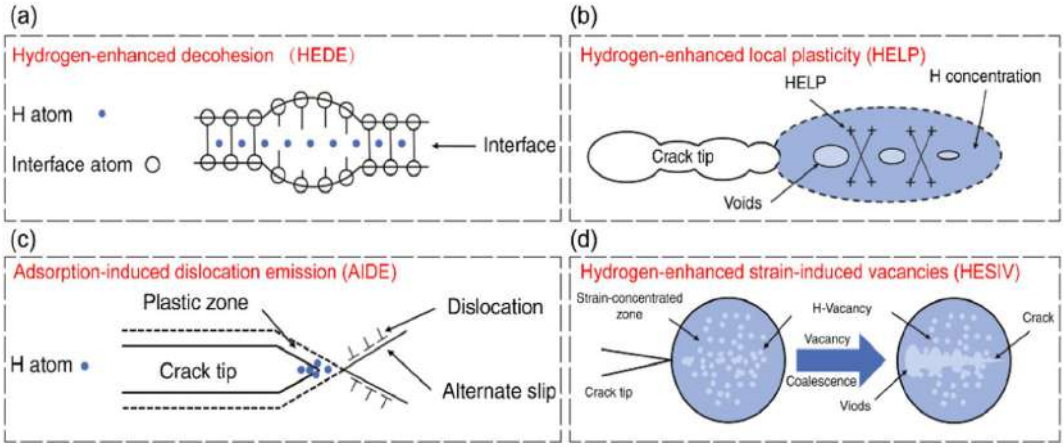

Figure 2.4.1: Multiscale depiction of hydrogen embrittlement: the classical trio of mechanisms (HELP, HESIV, HEDE) [48].

thereby lowering the stress required for dislocation glide. This enhanced mobility is localised to regions of elevated hydrogen concentration typically the plastic zone ahead of a crack tip or near a stress concentrator. Macroscopically, the material appears to undergo intense local plasticity (dimple-like features in fracture surfaces) while failing at an overall lower macroscopic strain than an uncharged counterpart. Specifically:

- Hydrogen lowers the activation energy for dislocation nucleation and cross-slip, concentrating plastic deformation into narrow slip bands [36].
- The local slip concentration promotes rapid crack advance along slip planes or sub-grain boundaries, producing the quasi-cleavage facets and transgranular crack paths frequently observed in hydrogen-charged Ni-based alloys [30].
- In-situ TEM observations have directly confirmed that dislocation velocity increases measurably under hydrogen atmosphere at concentrations well below the solubility limit [36].

In Ni 725 and related precipitation-hardened systems, the HELP mechanism is considered to operates through hydrogen-enhanced dislocation mobility on activated slip planes. As hydrogen reduces the local barrier to dislocation glide, plastic deformation localises onto crystallographically favourable slip planes, producing the observable surface slip steps and secondary cracking features characteristic of HELP-driven embrittlement [50, 30].

2.4.2 HEDE: Hydrogen-Enhanced Decohesion

The HEDE mechanism, formalised by Oriani [22], proposes that dissolved hydrogen reduces the cohesive strength of interatomic bonds at the crack tip or at grain boundaries. Hydrogen atoms segregating to regions of high tensile stress (grain boundaries, phase interfaces, precipitate–matrix interfaces) lower the work of separation, γ_s, required to create two new surfaces. From an energy balance perspective, this is equivalent to a reduction in the Griffith fracture toughness K_{Ic}:

$$K_{Ic} \propto \sqrt{2E\gamma_s} \tag{2.13}$$

A reduction in γ_s caused by hydrogen accumulation at grain boundaries therefore directly lowers the stress intensity required for crack initiation and propagation [22, 30]. HEDE predicts intergranular fracture as the dominant mode, which is indeed observed in hydrogen-charged Alloy 725 and Inconel 718 specimens where δ-phase or Laves phase particles decorate grain boundaries, providing both preferential segregation sites for hydrogen and pre-existing interfacial weakness [39]. First-principles density-functional-theory (DFT) calculations have confirmed that hydrogen at Ni grain boundaries reduces the ideal work of separation by 20–40% depending on boundary character and hydrogen coverage, providing direct atomistic support for the HEDE model [30].

2.4.3 HESIV: Hydrogen-Enhanced Strain-Induced Vacancy Formation

The HESIV mechanism, proposed by Nagumo and collaborators [47], identifies hydrogen-stabilised vacancies rather than dislocations or cohesion loss as the primary damage carriers. During plastic deformation, dislocation intersections generate individual vacancies at a rate that normally allows them to annihilate rapidly by diffusion to free surfaces or sinks. Dissolved hydrogen, however, binds strongly to these vacancies (binding energy $\sim$0.1–0.4 eV in Ni [47]), reducing their mobility and preventing annihilation. The key consequences are:

- Stabilised vacancy–hydrogen (V–H) complexes accumulate within deformed slip bands at concentrations orders of magnitude higher than the thermal equilibrium value [47].
- Vacancy clusters nucleate nanovoids, which coalesce along preferred crystallographic planes or grain boundaries to form a planar damage zone.
- The material subsequently fractures at a far lower total plastic strain than an uncharged specimen because the vacancy cluster network has already created a pre-damaged microstructure ahead of the macroscopic crack [47].

Experimental evidence for HESIV includes positron annihilation lifetime spectroscopy (PALS) measurements showing that hydrogen charging elevates the vacancy-cluster density in deformed austenitic steels and Ni alloys by one to two orders of magnitude compared with uncharged controls [47]. In the context of Alloy 725, the high dislocation densities introduced by shot peening, has been observed to make the near-surface layer particularly susceptible to HESIV-type damage accumulation under subsequent hydrogen charging [51, 52].

2.4.4 AIDE: Adsorption-Induced Dislocation Emission

The AIDE mechanism, proposed by Lynch [30], focuses on the crack tip rather than the bulk plastic zone. Lynch proposes that hydrogen adsorbed at the crack-tip surface not absorbed in the bulk, weakening the interatomic bonds at the surface just enough to facilitate the nucleation and emission of dislocations from the crack tip at stresses well below those required in an inert environment. AIDE differs conceptually from both HELP and HEDE in that hydrogen acts at the *surface* as an adsorbed species rather than as a dissolved lattice solute, and its operative mode is dislocation *emission* from the crack tip rather than the acceleration of pre-existing bulk dislocations that characterises HELP. When H_{ads} is present at a crack tip, it reduces the Peierls barrier for nucleating new dislocations from the surface atomic layer, allowing the crack to advance by the successive emission of dislocations on inclined slip planes ahead of the tip; these dislocations create a void sheet that links back to the main crack front and produces the characteristic fractographic signature of AIDE transgranular fracture surfaces decorated with shallow dimples and fine slip steps, reflecting crack advance by void-sheet coalescence rather than by lattice cleavage or grain-boundary decohesion [30].

The study by Lynch et.al [30] provided experimental evidence supporting the Adsorption-Induced Dislocation Emission (AIDE) mechanism, demonstrating that hydrogen chemisorbed on FCC metal surfaces significantly reduces the local shear strength measured by nanoindentation and promotes extensive dislocation emission from crack-tip regions. Surface-science investigations revealed that hydrogen adsorption lowers the energy barrier for dislocation nucleation, facilitating crack advance through repeated cycles of dislocation emission and localized plastic deformation rather than by purely brittle cleavage. Similar observations have been reported from in-situ environmental electron microscopy and fracture studies of nickel- and iron-based alloys, where enhanced dislocation activity was detected ahead of hydrogen-exposed crack tips [53, 54, 50, 18]. Although AIDE is often considered secondary to HELP and HEDE in FCC nickel alloys, it is believed to contribute to crack initiation and early-stage crack propagation under conditions of high surface hydrogen coverage, particularly in cathodically charged specimens where continuous hydrogen adsorption occurs at surface defects, slip bands, and crack-tip regions [30, 18]. Consequently, AIDE may operate concurrently with HELP and HEDE, especially during the initial stages of hydrogen-assisted damage accumulation in Ni 725.

2.4.5 Deformation Under Hydrogen Charging

In practice, the four mechanisms described above are not mutually exclusive. As a hydrogen-charged specimen is loaded to failure, the sequence of events typically proceeds as follows:

1. **Elastic regime**: Hydrogen redistributes within the lattice driven by stress gradients (Gorsky effect), accumulating at high-triaxiality regions such as grain boundaries [36].

2. **Yield and early plastic flow**: HELP lowers the local yield stress [55], causing slip to initiate earlier and to localise more severely than in an un-

charged specimen. Simultaneously, dislocation intersections begin generating excess vacancies (HESIV) that are stabilised by the available dissolved hydrogen [47].

3. **Crack initiation**: Hydrogen accumulated at grain boundaries reaches a critical coverage that reduces the cohesive strength below the local stress (HEDE), nucleating microcracks. In the grain interior, hydrogen-enhanced dislocation activity on activated slip planes promotes dislocation pile-ups and slip band intersections; when the local stress at these intersections exceeds the lattice cohesive strength, transgranular microcracks nucleate along slip planes [50, 30]. At the same time, AIDE may initiate crack advance from pre-existing surface defects (machining marks, peening indentations) by facilitating dislocation emission [30].

4. **Crack propagation and fracture**: Once a crack advances, the triaxial stress field ahead of the tip concentrates hydrogen further, accelerating all four mechanisms in a self-reinforcing feedback loop until final fracture [48].

The fracture mode transitions from ductile dimple fracture in air to intergranular or transgranular fracture under hydrogen reflects the changing dominance of HEDE over HELP as the local hydrogen concentration increases.

2.4.6 Hydrogen Embrittlement Index

The ductility of a material under tensile loading is quantified by the reduction of area (%RA), which describes the relative decrease in cross-sectional area at the fracture plane:

$$\%\mathrm{RA} = \frac{A_0 - A_f}{A_0} \times 100 \tag{2.14}$$

where A_0 is the initial cross-sectional area and A_f is the cross-sectional area at the fracture location. Higher %RA values reflect substantial plastic deformation prior to fracture, while lower value means brittle fracture behaviour [4]. Compared with elongation-based measures, %RA is particularly sensitive to localised deformation in the necking region and is therefore a frequently used ductility metric in tensile testing. To isolate the influence of hydrogen on ductility, the reduction of area ratio (%RAR) is introduced:

$$\%\mathrm{RAR} = \frac{\mathrm{RA}_H}{\mathrm{RA}_{\mathrm{air}}} \times 100 \tag{2.15}$$

where RA_H and $\mathrm{RA}_{\mathrm{air}}$ denote the reduction of area for the hydrogen-charged and the uncharged reference specimen, respectively. The %RAR provides a relative measure of hydrogen-induced ductility loss and is widely employed to compare hydrogen embrittlement (HE) susceptibility across material conditions [56]. A %RAR approaching 100% indicates negligible hydrogen effect on ductility.

HE susceptibility can additionally be expressed through a strain-based indicator, the hydrogen embrittlement index (HEI):

$$\mathrm{HEI} = \frac{\varepsilon_{\mathrm{air}} - \varepsilon_H}{\varepsilon_{\mathrm{air}}} \times 100 \tag{2.16}$$

where ε_H and $\varepsilon_{\mathrm{air}}$ are the strains to fracture for the hydrogen-charged and reference specimens, respectively. The HEI quantifies the relative reduction in strain capacity attributable to hydrogen and is a widely applied indicator of hydrogen-assisted degradation [57]. %RA and %RAR give information on localised plastic deformation at the fracture surface, whereas, HEI reflects the overall reduction in strain capacity.

2.5 Surface Engineering Methods

Surface engineering modifies the outermost layer of a component to alter its chemical, physical, or mechanical properties. The effectiveness of a surface treatment depends on how it influences hydrogen adsorption, absorption, diffusion, trapping, and crack initiation processes [10]. The surface conditions considered in this study includes Electrical discharge machining (EDM), Surface peening, Nickel electrodeposition, and Gold sputtering methods and are therefore discussed in the following sections.

2.5.1 Electrical Discharge Machining and the Recast Layer

EDM is a non-contact material removal process in which the workpiece and a continuously fed wire electrode are submerged in a dielectric fluid typically de-ionised water and held at a precisely controlled gap. A pulsed voltage applied across this gap causes repeated dielectric breakdown, generating individual micro-arc discharges that last on the order of microseconds. Each discharge locally melts and vaporises a small volume of the workpiece surface; the dielectric fluid simultaneously flushes the expelled debris away and quenches the melt pool [58]. Figure 2.5.1 illustrates the principal components of a wire EDM machine: the wire is fed continuously from an upper pulley through the workpiece and recovered at a lower guide pulley, with the dielectric fluid supplied and filtered in a closed loop. The inset detail shows the spark gap between wire and workpiece and the kerf width that results from the discharge zone.

A fraction of the molten material resolidifies on the workpiece surface before it can be swept away by the dielectric. This thin, resolidified zone known as the recast layer or white layer is typically 1–30 μm thick and is chemically and microstructurally distinct from the underlying bulk alloy in three important respects [58, 60]. First, the extreme cooling rate ($\sim 10^7$ K/s) produced by rapid quenching of the melt pool against the cooler substrate yields a fine-grained to partially amorphous microstructure with an elevated dislocation density and a network of thermal microcracks generated by differential contraction during solidification. Second, the recast layer carries tensile residual stresses arising from the melt-quench thermal cycle, in direct contrast to the compressive surface state produced by shot peening. Third, decomposition of the de-ionised water dielectric

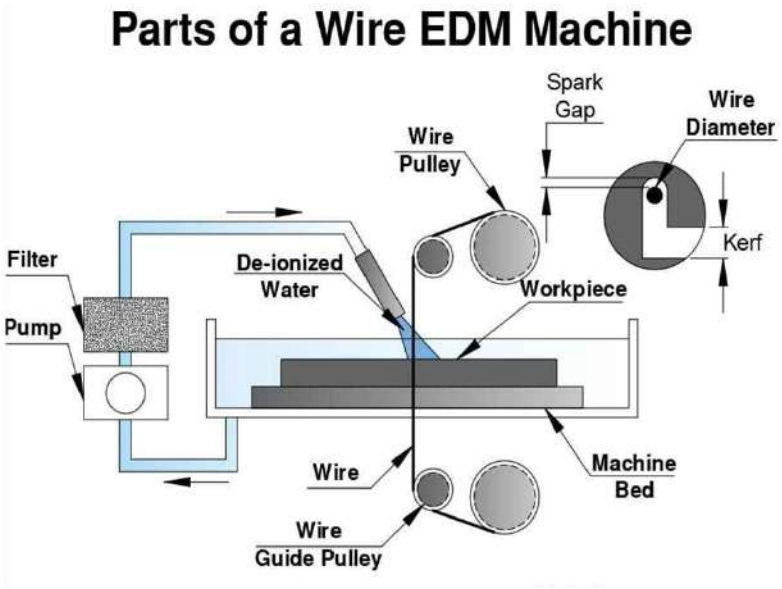

Figure 2.5.1: Principal components of a wire electrical discharge machining system [59].

and partial evaporation of alloying elements during the discharge deposit carbon, oxygen, and electrode material on the surface, altering the near-surface chemistry relative to the bulk alloy composition [60].

The near-surface state produced by wire EDM on any material is therefore characterised by a thin, thermally modified, chemically heterogeneous, and crack-seeded layer sitting under a tensile residual stress field. The consequences of this surface condition for hydrogen uptake, diffusion, and crack initiation are discussed in Section 2.6. Under typical process parameters, the average surface roughness of wire-EDM machined metallic surfaces ranges from $R_a \approx 0.8$–3.5 µm depending on pulse energy, wire feed rate, and number of passes [61, 62].

2.5.2 Peening & Compressive Residual Stress Fields

Peening is a cold-working surface treatment in which a stream of hard spherical media steel shot, glass beads, or ceramic particles is propelled at high velocity onto the component surface. Each individual impact plastically deforms a small hemispherical volume of near-surface material. Because the plastically stretched surface layer is constrained by the surrounding elastic bulk, it cannot expand freely upon unloading, and a biaxial compressive residual stress is locked into the surface layer as a result [63]. The depth and magnitude of this compressive zone are controlled by the shot size, hardness, velocity, and coverage (defined as the percentage of surface area subjected to at least one impact).

Figure 2.5.2 illustrates the working principle of peening: pressurised air or a centrifugal wheel accelerates the spherical media through a nozzle directed at the component surface. The incident angle, standoff distance, and nozzle traversal speed collectively control the spatial uniformity of impact coverage, while the air

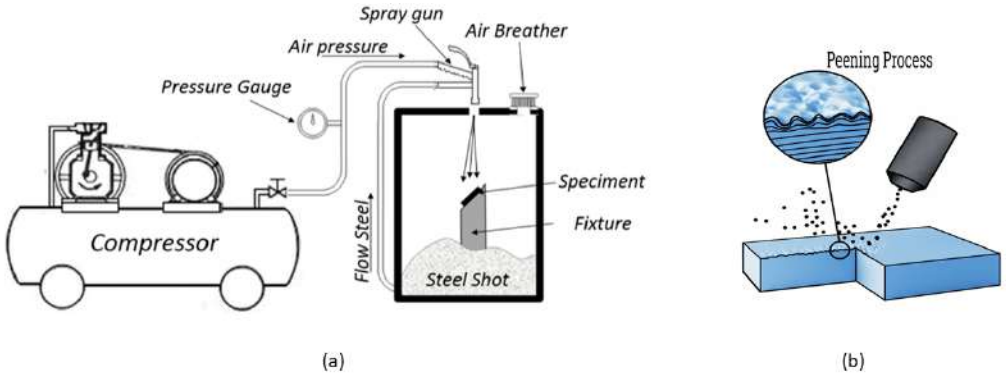

Figure 2.5.2: (a) Schematics of the Peening process set-up [64] (b) showing the nozzle, media stream, near-surface plastic deformation zone [65]

pressure and media size determine the kinetic energy delivered per impact and therefore the depth of the compressive zone [64, 63]. The surface roughness and affected layer depth produced by shot peening are strongly dependent on the shot media size and shape. Spherical ceramic beads (125–250 µm) and steel shot (400–900 µm) both yield arithmetical mean roughness values of $S_a \approx 6.9$ µm on metallic substrates, while angular nutshell granules (450–800 µm) produce higher roughness ($S_a \approx 7.8$ µm) due to their sharp-edged morphology [66]. The plastic deformation zone induced by ceramic beads extends to approximately 60 µm below the surface, compared with 25–30 µm for steel and nutshell media at equivalent pressure [66].

2.5.3 Nickel Electrodeposition

Nickel electrodeposition is an electrochemical process in which Ni^{2+} ions from an aqueous electrolyte are reduced at the cathode surface to form a metallic Ni coating [67, 68]. The overall cathodic half-reaction in an acidic Watts-type bath is:

$$Ni^{2+} + 2e^- \rightarrow Ni \tag{2.17}$$

In practice, this reaction competes with the hydrogen evolution reaction (HER):

$$2H^+ + 2e^- \rightarrow H_2 \tag{2.18}$$

Revankar et.al. [69] have cautioned that the hydrogen evolution reaction (HER) at the cathode competes directly with nickel deposition, reducing current efficiency and co-depositing atomic hydrogen into the growing coating. This co-deposited hydrogen promotes residual tensile stresses, microcracking, and porosity within the deposit [68, 69] defects that are particularly detrimental when the nickel layer is intended to function as a hydrogen permeation barrier, since even isolated through-thickness pores provide direct pathways for hydrogen ingress to the substrate. Minimising hydrogen evolution during plating is therefore not merely a processing concern but a barrier-performance requirement. Minimising hydrogen evolution is therefore critical when the nickel deposit is intended as a hydrogen barrier layer.

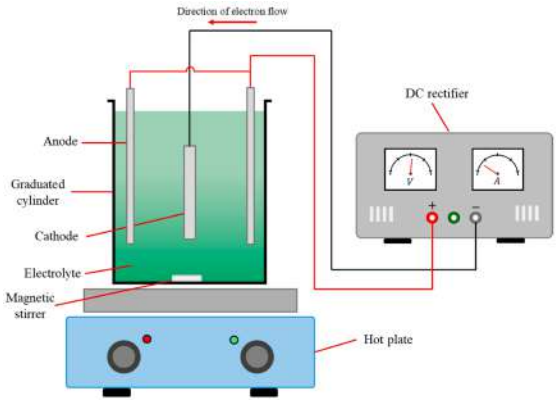

Figure 2.5.3: Schematic illustration of the electrochemical cell used for Watts-bath nickel electrodeposition

The classical electrolyte formulation that achieves this balance is the Watts bath, first systematically characterised by Watts in 1916 and subsequently optimised for industrial deposition of structural nickel coatings [67]. Löwenheim [67] established that the three-component system nickel sulfate ($NiSO_4 \cdot 6H_2O$, primary Ni^{2+} source), nickel chloride ($NiCl_2 \cdot 6H_2O$, which improves anode dissolution and bath conductivity), and boric acid (H_3BO_3, which buffers the pH in the cathodic boundary layer) provides the necessary combination of high current efficiency and deposit quality unattainable with single-salt baths. Microchemicals plating process guidelines [70] further specify that maintaining bulk bath pH within 4.5–5.0 and temperature between 40–65 °C is essential to suppress burnt deposits, excessive internal stress, and the coarse columnar grain morphology that would otherwise compromise coating continuity and barrier effectiveness [69]. Figure 2.5.3 illustrates the electrochemical cell configuration typically used in Ni plating.

2.5.4 Gold and Noble-Metal Surface Layers

Sputtering is a physical vapour deposition (PVD) technique in which material is transferred from a solid source, termed the target, to a substrate entirely through physical momentum exchange rather than chemical reaction or thermal evaporation [71]. In DC magnetron sputtering, an inert working gas typically argon, is introduced into an evacuated chamber and ionised by a sustained glow discharge maintained between a negatively biased target (cathode) and the grounded chamber walls [72]. The resulting Ar^+ ions are accelerated toward the target by the applied electric field and collide with the target surface, ejecting atoms and clusters through a sequence of momentum- transfer collisions within the near-surface lattice. The superimposed magnetic field of the magnetron confines secondary electrons to the target region, sustaining the plasma at lower operating pressures (typically 0.1–1 Pa) than conventional diode sputtering and greatly increasing the ionisation efficiency and deposition rate [71]. The ejected target atoms traverse the low-pressure gas phase and condense on the substrate, where they nucleate and grow into a thin, dense film. Figure 2.5.4 illustrates this working principle.

A key process advantage relevant to the deposition of barrier coatings is the low substrate temperature as the energy input to the substrate comes from the kinetic energy of arriving atoms rather than from radiant or conductive heat, sub-

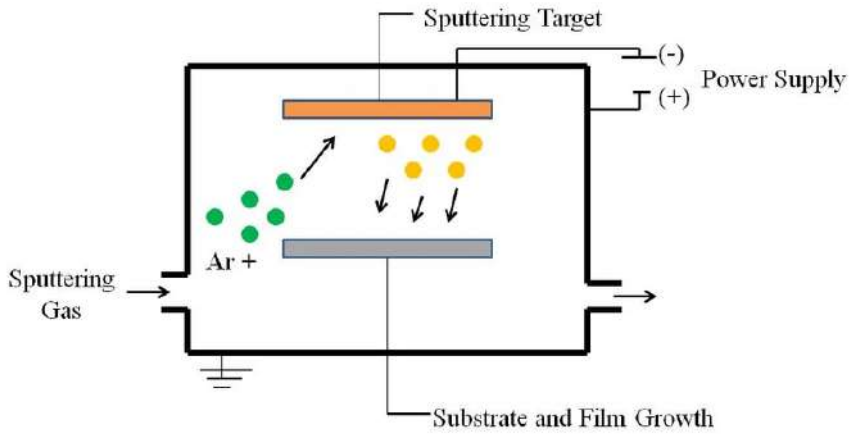

Figure 2.5.4: Working principle of DC magnetron sputtering [73].

strate temperatures typically remain below 100 °C throughout deposition. This is significantly lower than the processing temperatures required for Chemical vapor deposition, pack cementation, or thermal spraying, and it ensures that the substrate microstructure, residual stress state, and precipitate morphology are undisturbed by the coating process [72]. Film thickness is determined by deposition time and target power density, and coatings from a few nanometres to several micrometres can be deposited with high spatial uniformity.

2.6 Effect of Surface Modification on HE Behaviour

Surface modification are known to alter hydrogen uptake through two principal pathways by changing the entry kinetics at the surface–electrolyte interface, and changes to the near-surface trap density that influences the subsurface concentration profile [74]. The following subsections examine how each of the surface engineering techniques introduced in Section 2.5 influences these two pathways, and how the resulting near-surface hydrogen distribution translates into measurable changes in mechanical performance under hydrogen charging.

2.6.1 EDM Recast Layer and Crack Initiation

The surface left by wire EDM has tensile residual stresses and many small cracks in the recast layer. Under hydrogen charging, this combination lets hydrogen enter more easily and means cracks can start at a lower hydrogen concentration than on a smoothly ground surface.

The morphology of EDM-machined surfaces on nickel-based alloys is illustrated in Figure 2.6.1. Paswan et al. [75] compared the surface morphology of aluminium, brass, and Inconel 617 after identical wire EDM conditions, demonstrating that Inconel and other Ni-based alloys develop characteristically wide, irregular craters with a prominent redeposited layer and surface globules of resolidified material. The crater geometry is a direct consequence of the higher melting point and lower thermal conductivity of Ni-based alloys relative to aluminium or brass: less melt is expelled by the dielectric flush, so a thicker and more heterogeneous recast layer is

left behind on the crater wall. This thicker recast layer on Ni-based alloys implies a deeper tensile residual stress zone and a denser pre-crack population compared to more machinable alloys, making EDM-finished Ni alloy surfaces inherently more susceptible to hydrogen-assisted crack initiation.

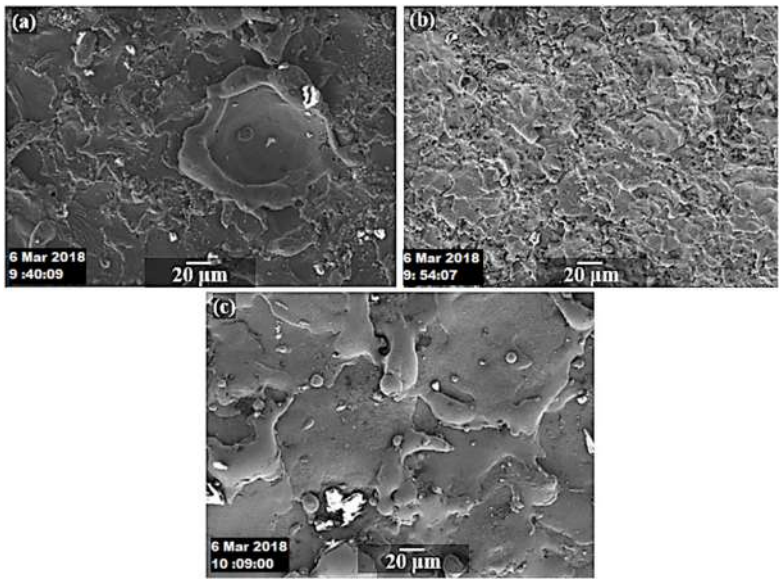

Figure 2.6.1: SEM micrographs at 500× of wire EDM-machined surfaces of (a) aluminium, (b) brass, and (c) Inconel 617 under identical discharge conditions [75].

The tensile residual stresses and pre-existing microcracks in the EDM recast layer are expected to reduce both the fracture strain and the HEI threshold relative to the ground reference. Microcracks formed during the rapid melt-quench cycle act as pre-existing crack initiators at which hydrogen rapidly accumulates, lowering the applied stress required for decohesion (HEDE) or dislocation emission (AIDE) to begin [76, 60]. This is illustrated in Figure 2.6.2, which shows a hydrogen-assisted crack in a Ni-based superalloy with an EDM-machined surface: the crack originates at a discrete surface site on the inner wall of a discharge crater, where the recast layer is thinnest and the tensile residual stress is highest and propagates inwards through the hydrogen-enriched near-surface zone [77]. The surrounding smooth, featureless annular zone is characteristic of fast, hydrogen-assisted crack propagation driven by the concentrated stress field at the recast-layer boundary [60, 78].

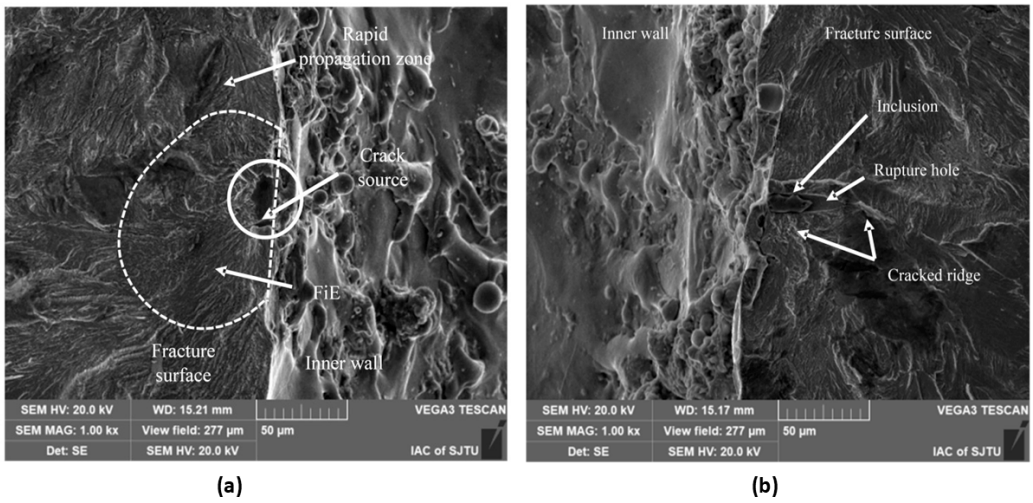

Figure 2.6.2: Hydrogen-assisted crack initiation at the inner wall of an EDM discharge crater in GH3536 (Hastelloy X), showing in (a) the crack source and rapid propagation zone on the fracture surface and in (b)view highlighting the inclusion, rupture hole, and cracked ridges along the recast layer boundary. Adapted from Zhang et al. [77].

2.6.2 Peening-Induced Residual Stress

Peening imposes a biaxial compressive residual stress layer in the near-surface region by plastically deforming the surface with high-velocity spherical impacts. The depth profile of the resulting stress field is intrinsically coupled to the dislocation microstructure generated during impact. The compressive stress field introduced by shot peening directly opposes mode-I crack opening under applied tension, raising the threshold stress intensity for hydrogen-assisted cracking and delaying crack initiation [79, 13]. This protective effect has been documented in pressure-vessel steels, where higher peening coverage levels progressively reduce hydrogen uptake and increase the critical hydrogen concentration for cracking. The opposing effect increased near-surface dislocation density and surface roughness means that the net benefit of peening on HE resistance depends on the relative contributions of stress shielding and enhanced trapping, which in turn depend on the specific alloy, peening intensity, and charging conditions [13].

The cross-sectional morphology of the Inconel 718 deformed layer from the study by [80] at different condtitions shows increasing peening severity deepens and densifies the plastically affected zone, expanding the population of both the compressive stress carriers and the reversible hydrogen trapping sites described in the preceding analysis.

Zhang et al. [81] identified four microstructurally distinct regions beneath the peened surface, illustrated in Figure 2.6.4: a severely deformed outermost layer containing stacking faults and dislocation tangles (1st region); a sub-surface zone of high dislocation density with persistent slip bands (2nd region); a transition zone

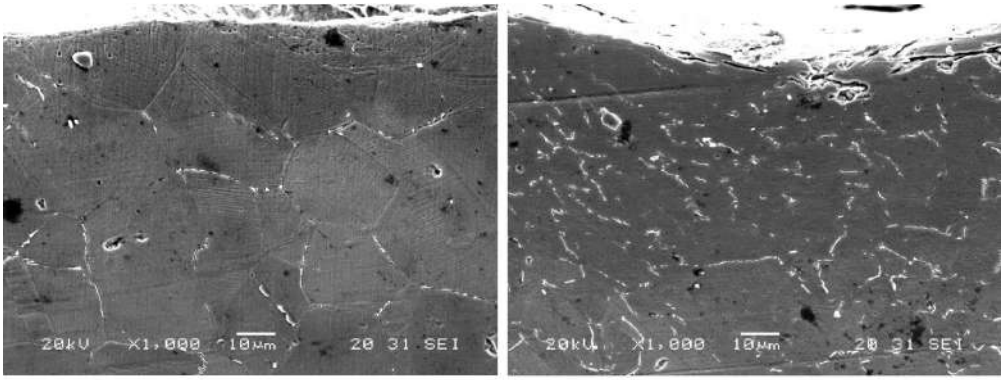

(a) Conventional shot peened material (b) Severe shot peened material

Figure 2.6.3: Cross-sectional SEM images at 1,000× of Inconel 718 after different surface peening[80].

where dislocation cells and residual network dislocations coexist (3rd region); and a lightly perturbed lattice approaching bulk material behaviour (4th region). The dislocation density and plastic strain decay monotonically with depth, while the residual stress transitions from compressive at the surface to a tensile sub-surface peak before relaxing to the unperturbed bulk value.

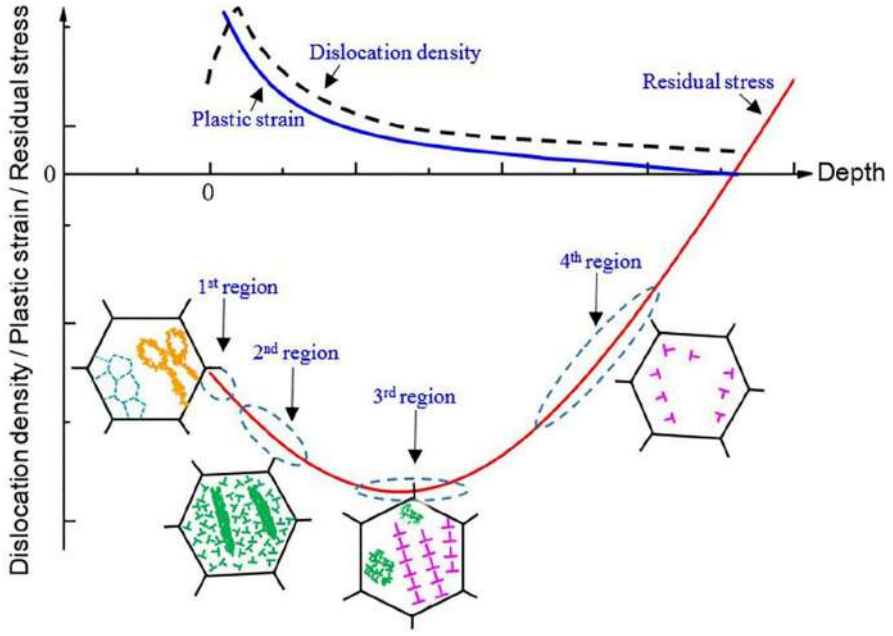

Figure 2.6.4: Schematic of the four microstructurally distinct regions beneath a peened surface, showing the correlated depth profiles of dislocation density (blue), plastic strain (dashed black), and residual stress (red). Adapted from Zhang et al. [81].

For hydrogen embrittlement, these two gradients compressive stress and elevated dislocation density act in opposing directions. Immediately at the surface (1st region), the extreme plastic deformation produces stacking faults and densely entangled dislocations the highest-energy microstructural state. Moving inward, the 2nd region contains a high density of newly generated dislocations organised

into slip bands, where plastic strain is still significant but the structure begins to organise. In the 3rd region, the dislocation population transitions into a mixed arrangement of dislocation cells and planar networks, reflecting the reduced local strain energy at greater depth. Finally, in the 4th region, only isolated, widely spaced dislocations remain, and the microstructure approaches that of the unperturbed bulk alloy. The Dislocation density and Plastic strain both peak at the surface and decay monotonically with depth, while the residual stress follows the opposite sign conventioncompressive at the surface and transitioning to a subsurface tensile peak before returning to zero in the bulk. This profile is central to the hydrogen embrittlement response of the peened surface: the compressive zone suppresses crack opening, while the dense dislocation structure in the 1st and 2nd regions simultaneously provides the highest reversible trap density for hydrogen, making the near-surface region both the most protective and the most hydrogen-retentive zone in the specimen.

2.6.3 Nickel Coatings as Hydrogen Barriers

Hydrogen permeation through a coated metal substrate proceeds through a sequence of distinct physical steps, illustrated schematically in Figure 2.6.5: molecular adsorption of H_2 on the coating surface, dissociation into atomic hydrogen, absorption into the film lattice, solid-state atomic diffusion through the coating, transfer across the coating–substrate interface, continued diffusion through the substrate, and finally recombinative desorption as H_2 on the exit side [82, 71]. Each of these steps presents a potential rate-limiting resistance; an effective barrier coating must suppress at least one of them sufficiently to reduce the overall permeation flux. A noble-metal coating such as gold acts primarily at the first step, suppressing molecular adsorption and dissociation at the inert surface, whereas a dense ceramic or nanostructured Ni coating acts primarily by reducing the solid-state diffusivity within the film.

Dense, fine-grained nickel electrodeposits produced under well-controlled conditions have been widely investigated as hydrogen permeation barriers on steels and hard-metal substrates [84, 85, 69]. Key findings from the literature are:

- Relatively thin coatings (5–20 μm) can reduce the effective hydrogen diffusion coefficient by one to two orders of magnitude on steel substrates, provided pinholes and through-thickness cracks are minimised [84, 85].
- Amorphous or nanocrystalline electroless Ni–P and Ni–Zn–P coatings outperform crystalline electroplated Ni by a further one to two orders of magnitude in permeation reduction factor (PRF), owing to the absence of grain-boundary diffusion paths [86, 87].
- Microcracking being the principal defect mode in over-stressed deposits — can reduce the effective PRF by orders of magnitude and must be avoided by careful control of current density and bath pH [67, 68].

Table 2.6.1 compiles quantitative hydrogen permeation data for Ni-based coatings. Although the substrates in these studies are predominantly carbon or pipeline steel, the permeation reduction is primarily controlled by coating microstructure

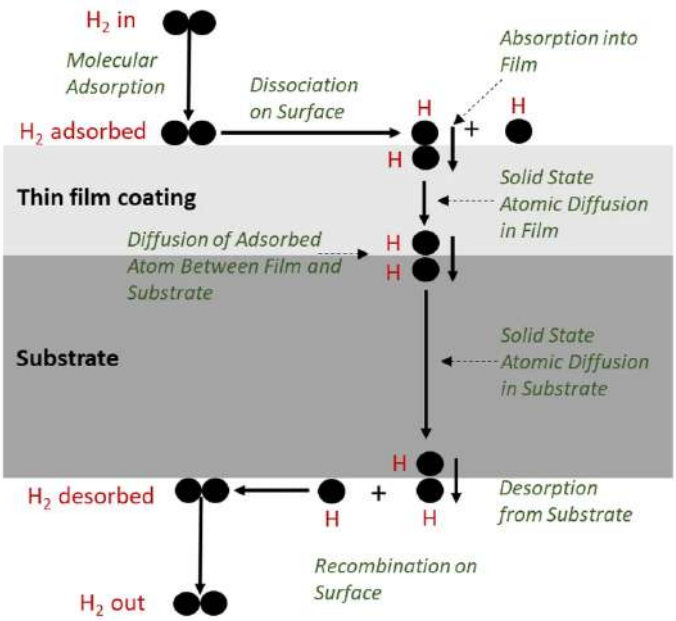

Figure 2.6.5: Schematic of the complete hydrogen permeation pathway through a coated substrate [83]

and continuity rather than substrate chemistry. Given that Ni 725 exhibits an intrinsic hydrogen diffusivity already six to seven orders of magnitude lower than ferritic steel [88], similar or greater reductions in hydrogen ingress are expected when dense Ni-based coatings are applied to Ni 725.

Table 2.6.1: Hydrogen permeation data for nickel-based coatings. D_{eff} and PRF are taken or derived from steady-state permeation measurements in the cited studies.

Coating	Deposition	Thickness / µm	D_{eff} / cm^2s^{-1}	PRF†
Bare steel (AISI 4340)	–	–	1.1×10^{-6}	1
Electroplated Ni on 4340	DC Ni plating	10	1.4×10^{-8}	79
Electroplated Ni on 4340	DC Ni plating	20	8.5×10^{-9}	129
Electroless Ni–P on steel	Ni–P, 9 wt% P	10	3.0×10^{-9}	370
Electroless Ni–P on steel	Ni–P, 11 wt% P	15	1.0×10^{-9}	1150
Ni–P on steel (annealed 400 °C)	Ni–P, amorph.→nano-cryst.	15	6.0×10^{-10}	1900
Nanostructured ZnNi on steel	DC ZnNi, nano-cryst.	7	2.0×10^{-9}	7
Microcrystalline ZnNi on steel	DC ZnNi, micro-cryst.	7	1.0×10^{-8}	1.4
Amorphous Ni–Zn–P on steel	DC Ni–Zn–P, amorph.	8	3.8×10^{-9}	950

†PRF = permeation reduction factor relative to the uncoated steel substrate, defined as PRF $= J_{\text{bare}}/J_{\text{coated}}$, using data from Refs. [37, 89, 90, 91, 92].

Figure 2.6.6 presents representative literature data for the normalised steady-state hydrogen permeation current as a function of coating thickness for three electrodeposited Ni-based systems on steel: crystalline electroplated Ni, electroless Ni–P, and amorphous Ni–Zn–P [90, 37, 93]. All three coatings reduce the permeation current monotonically with increasing thickness, consistent with a solid-state diffusion barrier mechanism. At a coating thickness of 10 µm, the amorphous Ni–Zn–P system reduces the normalised permeation current to approximately 8×10^{-3}

relative to bare steel, compared with $\sim 1.5 \times 10^{-2}$ for Ni–P and $\sim 1.4 \times 10^{-1}$ for crystalline Ni at the same thickness. The superior performance of the amorphous systems is attributed to the elimination of grain-boundary fast-diffusion paths, consistent with the microstructure-dependent diffusivity data compiled in Table 2.6.1. At 15 µm, the Ni–Zn–P coating achieves approximately one order of magnitude greater permeation reduction than crystalline Ni, underscoring the critical role of coating phase structure over thickness alone in determining barrier effectiveness [90, 37, 93].

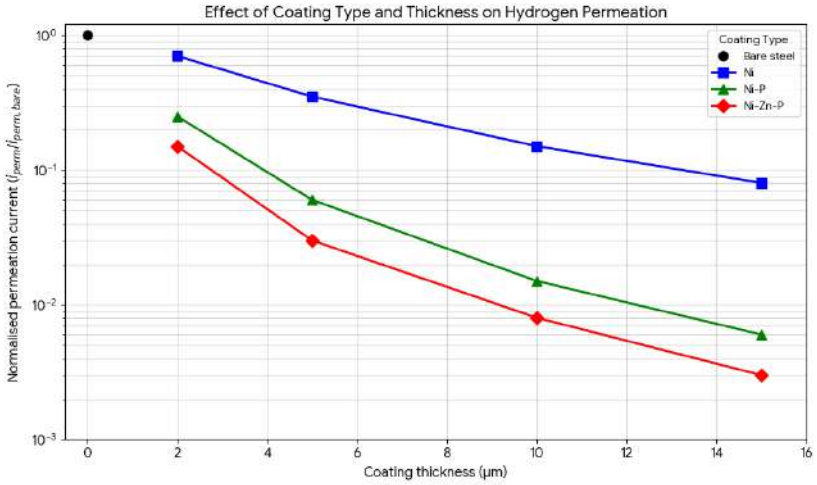

Figure 2.6.6: Representative literature trend for the reduction in steady-state hydrogen permeation current with increasing thickness of electrodeposited Ni, electroless Ni–P, and amorphous Ni–Zn–P coatings on steels [90, 37, 93].

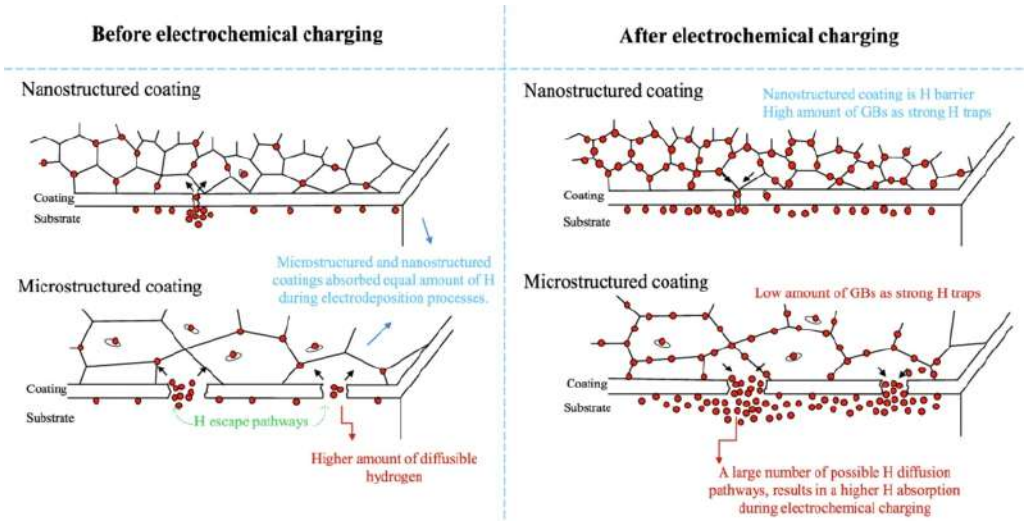

Figure 2.6.7: Schematic comparison of nanostructured and microstructured coatings before and after electrochemical hydrogen charging. In the nanostructured coating, the high density of grain boundaries acts as strong hydrogen traps, blocking through-thickness diffusion. In the microstructured coating, fewer grain boundaries provide open diffusion pathways, resulting in higher hydrogen absorption at the substrate during charging [90].

The role of coating grain size in determining barrier effectiveness is illustrated schematically in Figure 2.6.7: in a nanostructured deposit the high grain boundary density acts as a network of strong hydrogen traps that retards through-thickness diffusion, whereas a microstructured coating with fewer, wider grain boundary channels allows rapid hydrogen transport to the substrate [92, 90, 37].

2.6.4 Gold-Sputtered Surface

The barrier effect of a sputtered Au film arises primarily through the suppression of the Volmer adsorption step (Equation 2.3) at the inert gold surface [94], rather than through bulk diffusion resistance across a thick coating [95]. The consequences of these properties for hydrogen uptake and the embrittlement response of Ni 725 are discussed in Section 2.6. Gold is of particular interest as a model noble-metal hydrogen barrier for the following reasons:

- **Low hydrogen solubility**: Gold possesses one of the lowest hydrogen solubilities of any metal, arising from its filled *d*-band and noble electronic structure. The thermodynamic driving force for hydrogen absorption into the gold lattice is minimal, so the gold film acts as a kinetic barrier by preventing hydrogen from adsorbing in the first place rather than by slowing bulk diffusion [96, 82].

- **Chemical inertness**: Gold does not oxidise or corrode under ambient or aqueous conditions. This means the film surface stays chemically unchanged throughout the entire charging experiment, so the measured response reflects the substrate behaviour alone and is not complicated by oxide formation or surface degradation [72].

- **Dense, conformal film**: A sputtered Au film of approximately 100 nm is compact and follows the substrate surface closely, avoiding the through-thickness pores that limit thicker thermal-spray coatings. The key requirement is full surface coverage: a single pinhole is enough to create a direct channel for hydrogen to reach the substrate beneath, bypassing the barrier entirely [82].

In the hydrogen-technology literature, thin Au films have been explored as protective overlayers on palladium membranes and as barrier layers on steels, where they reduce the permeation flux and delay hydrogen-assisted failure [82]. In the present thesis, gold sputtering is used specifically as a model to isolate the role of surface chemistry from the mechanical effects of other treatments (EDM, peening), rather than as a directly industrially viable coating.

CHAPTER

THREE

METHODS

Ni 725 alloy was used as the base material and subjected to hydrogen charging under different conditions, both before and after surface treatment. Five surface preparation routes were investigated: grinding to 2000-grit SiC (reference), electrical discharge machining (EDM), Peening (IEPCO Peenmatic 750), gold sputter coating and nickel electrodeposited coating (Watts bath) was applied to a set of ground specimens as the primary protective coating condition. Samples with identical nominal gauge-section geometry were hydrogen pre-charged for 24 h prior to tensile testing, with the ground 2000-grit specimens additionally tested in air as uncharged references. The effect of surface state and hydrogen exposure on yield strength, fracture behaviour, and microstructural response was evaluated by combining in-situ tensile testing inside the SEM with post-mortem fractography and EDS imaging.

For each specimen, the experimental work was done in the following sequence:

1. Grinding and polishing of the tensile specimen.
2. Surface treatments (where applicable).
3. Electrochemical hydrogen pre-charging.
4. Tensile testing inside the SEM (in-situ).
5. Post-fracture SEM characterization.
6. FIB cross-sectioning on selected samples.

3.1 Material composition and Specimen Geometry

Ni-725 alloy was used as the substrate material and its chemical composition and the functional role of the main alloying elements are summarized in Table 3.1.1.

Table 3.1.1: Chemical composition of Ni 725 alloy in wt% and functional role of each element.

Element	wt%	Role in the alloy
Ni	55.0–59.0	Base element; provides high-temperature strength and corrosion resistance.
Cr	19.0–22.5	Improves resistance to oxidizing environments and pitting corrosion.
Mo	7.0–9.5	Enhances resistance to pitting and crevice corrosion.
Nb	2.75–4.0	Forms γ'' strengthening precipitates during aging.
Ti	1.0–1.7	Works with Nb to enable precipitation hardening.
Fe	balance	Cost-effective filler; contributes to overall structural integrity.
Al	0.35 max	Acts as a deoxidizer; assists in hardening.
C	0.03 max	Kept very low to limit carbide sensitization.

The tensile specimens were EDM machined from Ni725 bar stock according to the dimensions shown in Figure 3.1.1. The geometry was chosen to fit the in-situ tensile stage while providing a uniform gauge section for imaging.

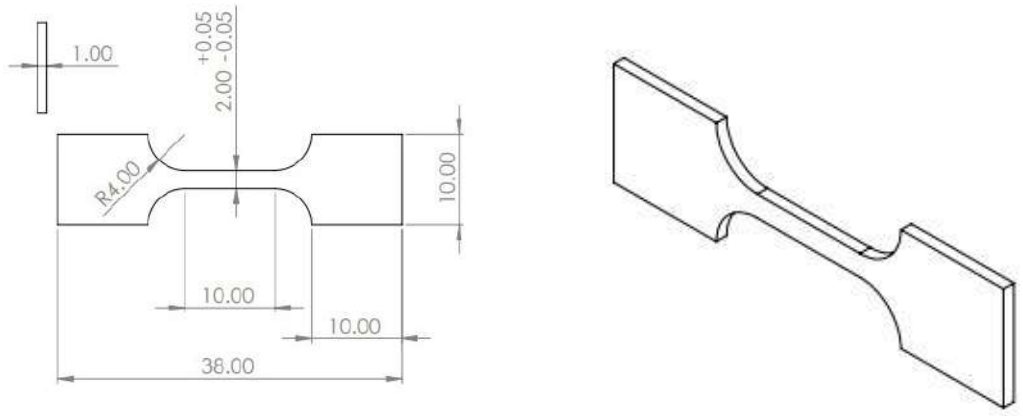

(a) Front view of the tensile specimen. **(b)** Side view of the tensile specimen.

Figure 3.1.1: Schematic of the tensile specimen showing shape and dimensions (mm).

3.2 Sample Preparation

All tensile specimens underwent surface preparation prior to coating and/or hydrogen charging. Grinding was performed on both faces using a Buehler MetaServ-250 machine with Struers SiC paper in the sequence 220, 500 and 1000 grit. The specimens were held manually against the rotating disc and periodically rotated to maintain uniform material removal. After grinding, all specimens were rinsed with distilled water, cleaned with ethanol and air-dried. The cross-sectional area

of the gauge section, used for engineering stress calculations, was measured optically before testing. If required for EBSD or coating adhesion, additional fine polishing steps (down to colloidal silica) were applied on selected specimens.

3.3 Surface Modification

3.3.1 Electrical discharge machined (EDM) Specimen

A set of specimens produced directly from bulk Ni725 stock by wire electrical discharge machining (EDM) was reserved. The complete tensile geometry shown in Figure 3.1.1 was cut by wire EDM. No subsequent grinding or mechanical polishing was applied to the gauge section, so the as-cut EDM surface, including its thermally affected recast ("white") layer, was preserved for testing. The cross-sectional area and gauge length of each EDM specimen were measured using a calibrated optical microscope before hydrogen charging and tensile testing.

3.3.2 Grinding to 2000-Grit SiC Specimen

For specimens designated as the ground reference condition, an additional grinding step to 2000 grit SiC was applied following the initial preparation sequence described in Section 3.2. This produces a smooth, reproducible surface (estimated $R_a < 0.5$ μm) free of recast layers, peening-induced deformation, or coatings, and serves as the baseline against which the embrittlement susceptibility of all other surface conditions is benchmarked.

3.3.3 Peened Surface Specimen

Peening was performed on the gauge section of selected ground specimens using an IEPCO Peenmatic 750 system using ceramic particles. The peening was applied to both broad faces of the gauge section. After peening, specimens were cleaned with ethanol and air-dried. The peened surface condition is expected to introduce a compressive residual stress layer to a depth of approximately an estimated near-surface plastic deformation depth of approximately 25 µm to 75 µm, as is typical for this class of system.

Surface roughness and defect density:

Surface roughness establishes a direct relationship with hydrogen embrittlement susceptibility: rougher surfaces accumulate a higher density of lattice defects principally dislocations and vacancy clusters that act as reversible hydrogen traps and preferential nucleation sites for hydrogen-assisted microcracks [97, 98]. The flux of hydrogen absorbed at a rough surface is enhanced both by the larger real contact area and by the stress concentration at asperities, which lowers the activation barrier for surface hydrogen dissociation and subsurface diffusion [97]. In the context of electrochemical charging, a surface ground to 2000-grit SiC provides a reproducible, lightly worked reference condition; EDM and shot-peened surfaces

increase trap density and surface area progressively, while Ni-plated and gold-sputtered surfaces interpose a physical barrier that fundamentally decouples the substrate surface from the electrolyte [99, 17].

3.3.4 Gold sputter coated Specimen

A thin gold film was deposited on selected specimens by magnetron sputtering using a sputter coater. The gauge section was sputter coated for yielding an estimated film thickness of approximately 100 nm. Sputtering was performed at room temperature in an argon atmosphere. The gold-coated specimens were handled carefully to avoid film damage prior to hydrogen charging. Gold sputtering was used as a model noble-metal surface layer to probe the effect of a chemically inert, low-hydrogen-solubility interface on hydrogen embrittlement susceptibility.s

3.3.5 Nickel electroplating procedure

A nickel electrodeposit was applied to selected Ni725 tensile specimens prior to hydrogen charging in order to act as a hydrogen diffusion barrier. The plating process followed a Watts-type electrolyte and was divided into four stages: surface pre-treatment, bath preparation, electroplating and post-plating handling.

Phase 1: Surface pre-treatment

Successful electrodeposition requires a chemically clean and oxide-free substrate surface. Even trace amounts of oil, grease or native oxides can inhibit nucleation and lead to poor adhesion or porous deposits. The following pre-treatment sequence was therefore applied to all specimens selected for coating:

1. **Mechanical polishing**: The gauge section was ground with SiC paper up to 1000–2000 grit in order to remove the native oxide layer. Grinding marks were aligned along the tensile axis to minimise stress concentrators.

2. **Ethanol degreasing**: The samples were soaked in ethanol and done with ultrasonication to remove the organic contaminants. After cleaning, the specimens were rinsed in de-ionised water to remove residual cleaner.

Phase 2: Watts bath preparation

Nickel deposition was carried out from a conventional Watts electrolyte. The bath was prepared in the following order to ensure complete dissolution of all constituents:

1. **Initial volume**: A glass beaker was filled with DI water to approximately 70 % of the desired final bath volume.

2. **Heating**: The solution was heated to 50 °C while being gently stirred.

3. **Nickel sulfate (135 g/L)**: $NiSO_4 \cdot 6H_2O$ was added gradually and dissolved completely. This salt provided the primary source of Ni^{2+} ions for deposition.

4. **Nickel chloride (30 g/L)**: $NiCl_2 \cdot 6H_2O$ was then added and dissolved. Nickel chloride improves anode dissolution and increases the electrical conductivity of the bath.

5. **Boric acid (18.5 g/L)**: H_3BO_3 was added last. Boric acid acts as a weak buffer in the cathodic boundary layer and stabilises the local pH during plating.

6. **Final dilution**: Finally, DI water was added up to the target volume and the solution was stirred until a clear, homogeneous green electrolyte was obtained.

Phase 3: Electroplating process

The nickel coating was deposited under galvanostatic conditions using the following configuration:

1. **Electrochemical setup**: The Ni725 tensile specimen was connected as the cathode (negative terminal), a platinum served as the inert anode (positive terminal) and Ag/AgCl reference electrode was used.

2. **Operating parameters**: The bath temperature was maintained in the range 50 °C. The applied current density was maintained at 0.15 A/cm^2, corresponding to a moderate deposition rate aimed at producing a dense, low-porosity coating. The bulk bath pH was controlled between 4.5 and 5.0; increases in pH were corrected using nickel carbonate, while decreases were adjusted with dilute sulfuric acid.

3. **Plating time**: For the present study a relatively thin nickel layer was targeted in order to act as a hydrogen barrier without introducing excessive residual stress. Plating time was 2 hours.

4. **Agitation**: The electrolyte was agitated using magnetic stirring. Agitation reduces the diffusion layer thickness, improves the supply of Ni^{2+} ions to the cathode and helps to detach hydrogen bubbles from the surface, thereby minimising pitting and hydrogen entrapment in the growing deposit.

Phase 4: Post-plating handling

Immediately after electroplating the specimens were removed from the bath and subjected to the following steps:

1. **Rinsing**: The coated samples were rinsed thoroughly with DI water to remove residual electrolyte and to stop further electrochemical reactions.

2. **Drying**: The specimens were dried either with a warm air gun to prevent water spots and to avoid corrosion before hydrogen charging.

Throughout the plating process, particular attention was paid to minimising hydrogen evolution, maintaining a stable current response without large transients

and keeping the bath pH within the specified range. Poor control of these parameters is known to promote microcracks, porosity and residual hydrogen in electrodeposited nickel coatings, which would degrade their performance as hydrogen barriers [100].

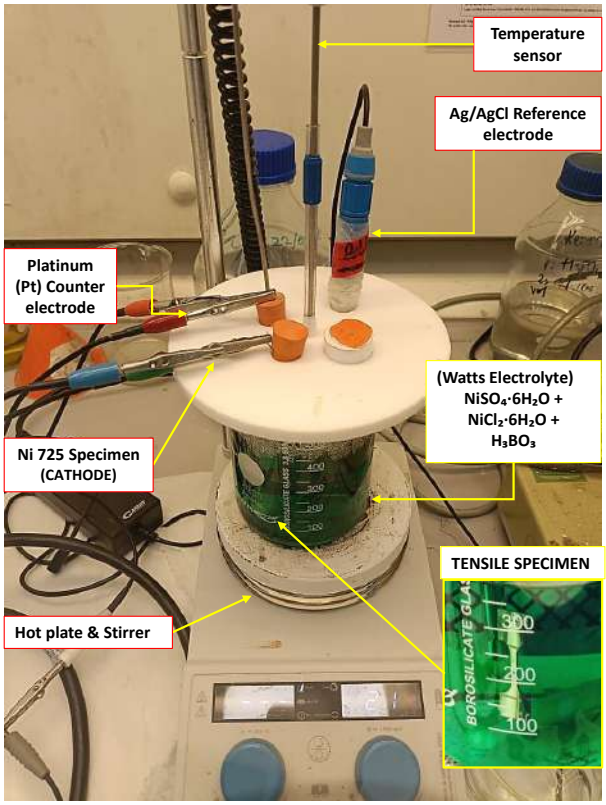

Figure 3.3.1: Schematic illustration of the electrochemical setup for Watts-type nickel electroplating on Ni725 tensile specimens.

3.4 Hydrogen Charging Procedures

After surface preparation (and coating deposition where applicable), both coated and uncoated specimens were electrochemically hydrogen charged. The charging was conducted at 50 °C in a 2:1 (vol.%) glycerol–H_3PO_4 electrolyte, with the temperature controlled by a hot plate and monitored using a thermocouple positioned close to the specimen. A dedicated electrochemical cell was used to provide stable galvanostatic charging and reproducible specimen mounting and electrical contact. The Ni 725 tensile specimen served as the working electrode, a platinum mesh as the counter electrode, and an Ag/AgCl electrode as the reference. Figure 3.4.1 depicts the charging set-up used for the samples. The counter and reference electrodes were immersed in the preheated electrolyte and connected to the potentiostat. Once the target temperature was stabilised, the specimen was immersed and the galvanostatic charging sequence was initiated under computer control.

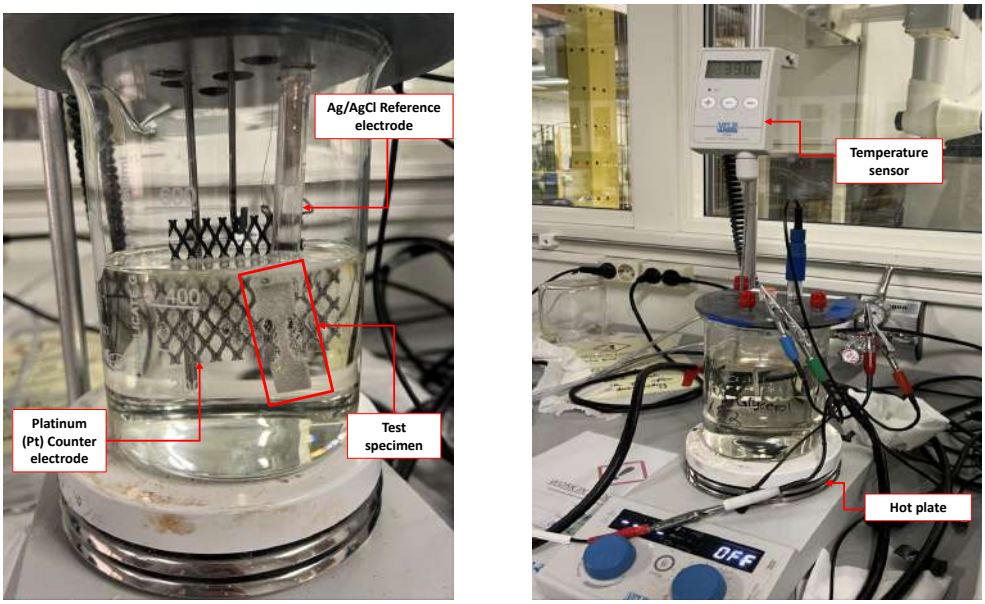

Figure 3.4.1: Electrochemical hydrogen charging setup (a) showing the Ni725 working electrode, Pt counter electrode, Ag/AgCl reference electrode (b) temperature-controlled electrolyte bath.

3.5 Tensile Testing with In-Situ SEM Observations

Tensile tests were carried out inside an FEI QUANTA 650 FEG SEM using a dedicated in-situ micro-tensile stage. The specimens were loaded in displacement control until fracture while the gauge section was continuously imaged to capture crack initiation and propagation. The mechanical response was recorded as stress–strain curves, and the synchronized SEM image sequences were subsequently used to correlate macroscopic behaviour with local damage evolution. The strain rate was set to 1 μm/s for all tests.

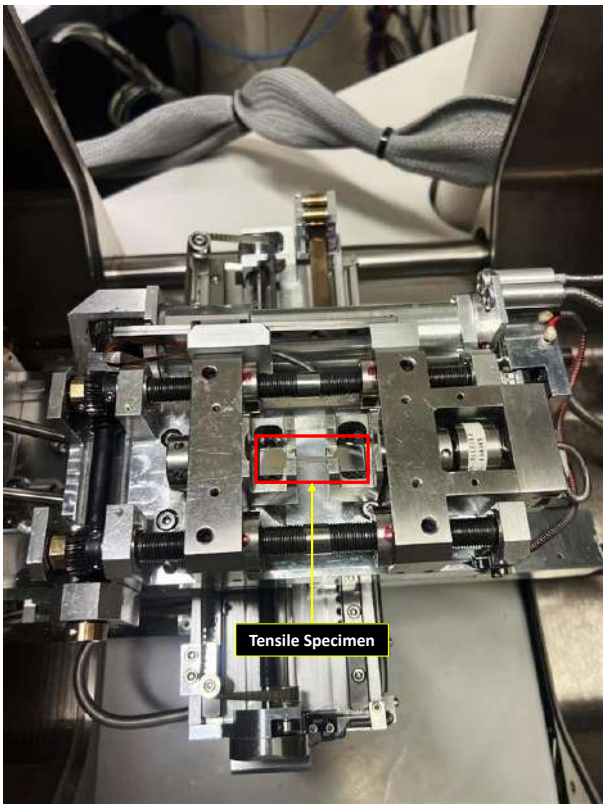

Figure 3.5.1: In-situ tensile test set-up mounted inside the SEM chamber.

3.6 Microstructural Characterization

Post-fracture microstructural characterization combined conventional SEM imaging, EDS, and FIB–SEM cross-sectioning. The goal was to link macroscopic embrittlement to fracture morphology, secondary surface damage and subsurface features.

3.6.1 Fracture and Surface Crack Examination

Fractography was first performed on all specimens. Cross-sectional overview images of the fracture were acquired at ∼110× magnification to document the overall fracture profile, followed by higher-magnification imaging to resolve local features such as dimples, quasi-cleavage facets, intergranular regions and secondary crack branching. Additional surface imaging was carried out along the gauge section to characterise secondary surface cracks, their density, orientation and interaction with machining marks, typically over the 200×–1500× magnification range.

3.6.2 EDS Cross-Section Analysis

EDS was performed on cross-sectioned specimens to characterise the near-surface elemental composition and verify the integrity of the surface treatment layers. Elemental maps were collected for the principal constituents of Ni-725 (Ni, Cr, Fe, Mo, Nb) as well as the specific coating/treatment elements (Au for the gold-sputtered surface). All cross-sections were prepared by FIB–SEM prior to analysis.

3.6.3 Thermal Desorption Mass Spectrometry

Diffusible hydrogen contents were measured using a Bruker G4 Phoenix thermal desorption spectrometer (TDS). The instrument couples a carrier-gas hot-extraction furnace with a single-quadrupole mass spectrometer (m/z range 1–100 amu) to selectively detect hydrogen ($m/z = 2$) at concentrations down to the sub-ppm range. Following tensile testing, a portion of the fractured specimen was weighed and loaded into the Thermal Desorption Spectroscopy (TDS) system.

Following tensile testing, a section of the fractured specimen was placed in the TDS chamber. Hydrogen released during heating was transported by an inert carrier gas to the detector and continuously monitored as a function of temperature. The specimens were heated from 30 to 800 °C at a constant heating rate of $25\,^{\circ}\mathrm{C}\,\mathrm{min}^{-1}$. The measured hydrogen content is reported in weight parts per million (wppm) and represents the total extractable hydrogen within the specimen.

CHAPTER

FOUR

RESULTS

4.1 Surface Microstructure Characterisation before Tensile Testing

4.1.1 EDM-Finished Surface

The as-machined EDM surface of the Ni 725 tensile specimen was characterised by SEM prior to hydrogen pre-charging and tensile testing. Figure 4.1.1 presents a low-magnification overview and a high-magnification view of the gauge surface in the as-EDM condition.

At low magnification (Figure 4.1.1a), the EDM surface shows a uniformly pitted, crater-dominated topography. Scattered globular and irregular debris particles are visible across the gauge section,, which could be attributed to re-deposited material expelled and re-solidified during the spark erosion process. At higher magnification (Figure 4.1.1b), the recast layer morphology is clearly resolved. The surface is covered by a convoluted network of re-solidified material comprising interconnected ridges, folded sheets, and spherical as well as elongated globules with diameters ranging from approximately 1 to 10 µm. Scattered circular pores and micro-pits ($<$5 µm) are distributed across the surface.

To complement the surface SEM observations, EDS elemental mapping was performed on the as-machined EDM gauge surface prior to tensile testing. The mapped region corresponds to the highly irregular recast layer morphology observed in Figure 4.1.1b. Figure 4.1.2 presents the SE overview, composite overlay, and six selected elemental maps. nd the quantitative composition from eZAF analysis is summarised in Table 4.1.1

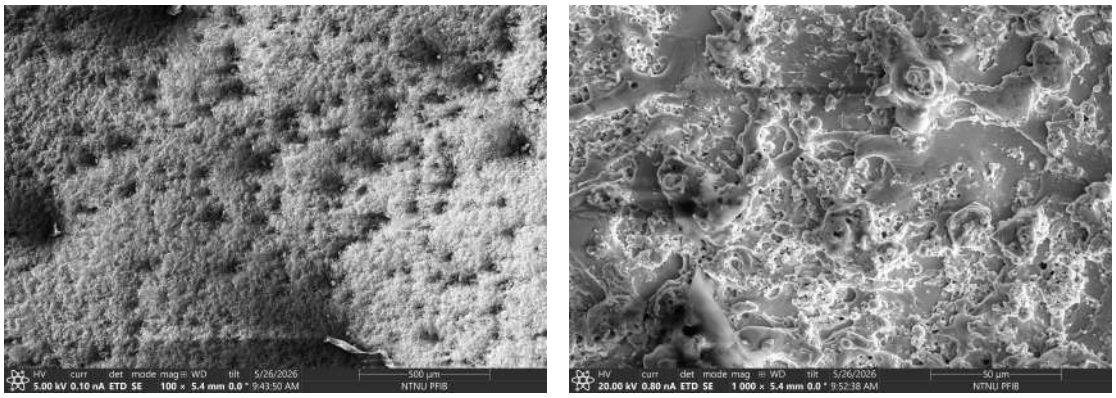

(a) **(b)**

Figure 4.1.1: SEM images of the EDM-finished Ni 725 gauge surface prior to hydrogen pre-charging and tensile testing. (a) Low-magnification overview (100×) showing the uniformly pitted, crater-dominated surface topography. (b) Higher-magnification view (1,000×) revealing the re-solidified recast layer morphology.

The oxygen map shows a non-uniform distribution, with higher concentrations at the raised globular features and ridges. The chromium map shows uniform Cr intensity with locally increased signals in certain regions. Nickel is broadly uniform across the mapped area, consistent with the bulk alloy beneath the recast layer. Mo distributions are seen to be uniform, with no evidence of segregation. The copper map shows localised Cu-rich patches on the surface; Zn was also detected at low levels. Both Cu and Zn could be the contamination from the brass electrode wire used during EDM. C and O together account for approximately 68.5 at% of the surface signal, reflecting the oxidised and carbon-enriched character of the recast layer as seen from the Table 4.1.1 .

Table 4.1.1: EDS quantitative analysis (eZAF, wt%) of the as-machined EDM surface prior to tensile testing (2,000×). Analysis uncertainty: 14.95%. Elements with signals below the minimum detection limit (MDL) are marked accordingly.

Element	Weight %	Atomic %
C K	20.4	48.6
O K	10.0	17.9
Ti K	1.7	1.0
Cr K	14.6	8.0
Fe K	4.4	2.3
Ni K	31.4	15.3
Cu K	7.2	3.3
Zn K	2.8	1.2
Nb L	2.7	0.8
Mo L	4.2	1.3

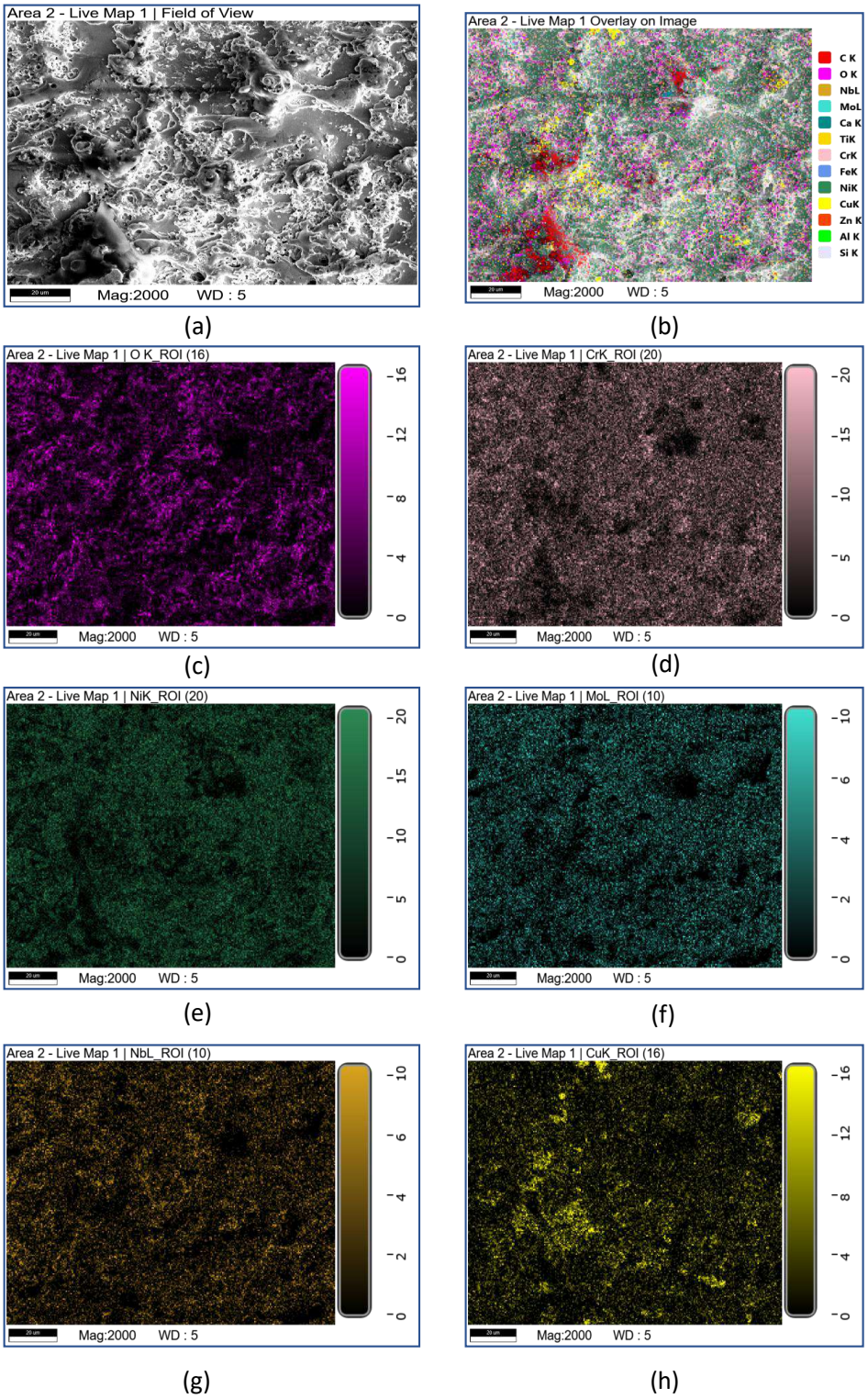

Figure 4.1.2: EDS elemental maps of the as-machined EDM surface of Ni 725 prior to tensile testing (2,000×). (a) SE overview of the EDM recast surface showing the highly irregular, globular recast morphology. (b) Composite overlay of all detected elements. (c) O map showing heterogeneous oxide distribution co-located with surface features. (d) Cr map showing local Cr depletion. (e) Ni map confirming broadly uniform bulk alloy signal. (f) Mo map. (g) Nb map. (h) Cu map showing localised Cu-rich patches.

4.1.2 Grinded Surface (2000-Grit SiC)

The SiC grit grinded reference surface of the Ni 725 tensile specimen was examined in plan view by SEM prior to hydrogen pre-charging and tensile testing, following the 2000-grit SiC grinding procedure described in the methods Section 3.3.2. The surface is dominated by a series of parallel grinding grooves running approximately along the tensile axis.

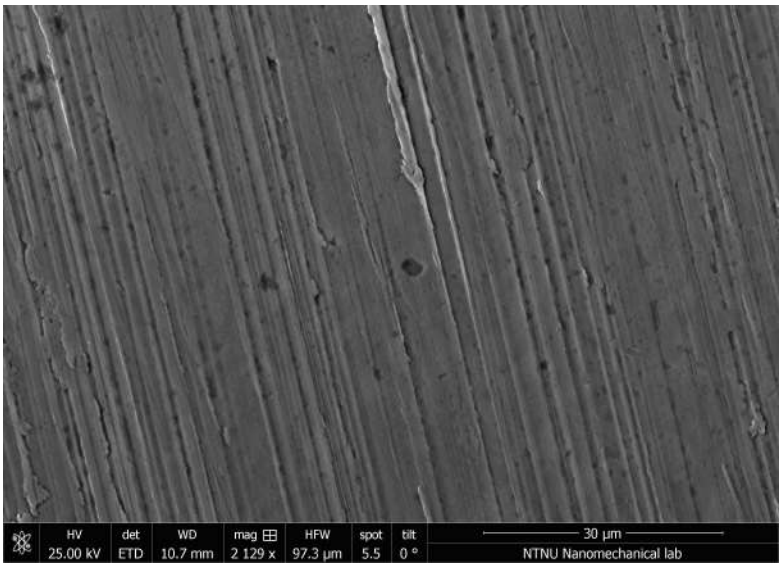

Figure 4.1.3: SEM image of the ground Ni 725 gauge surface prior to hydrogen pre-charging and tensile testing

4.1.3 Peened Surface

The peened surface of the Ni 725 tensile specimen was characterised by SEM prior to hydrogen pre-charging and tensile testing. Figure 4.1.4 presents the gauge surface in the as-peened condition. The surface exhibits a uniformly dimpled topography characterised by overlapping shallow hemispherical indentation craters distributed across the gauge section due to the impact of ceramic peening media. No thermal recast layer, resolidified globules are present, distinguishing the peened surface clearly from the EDM-finished condition.

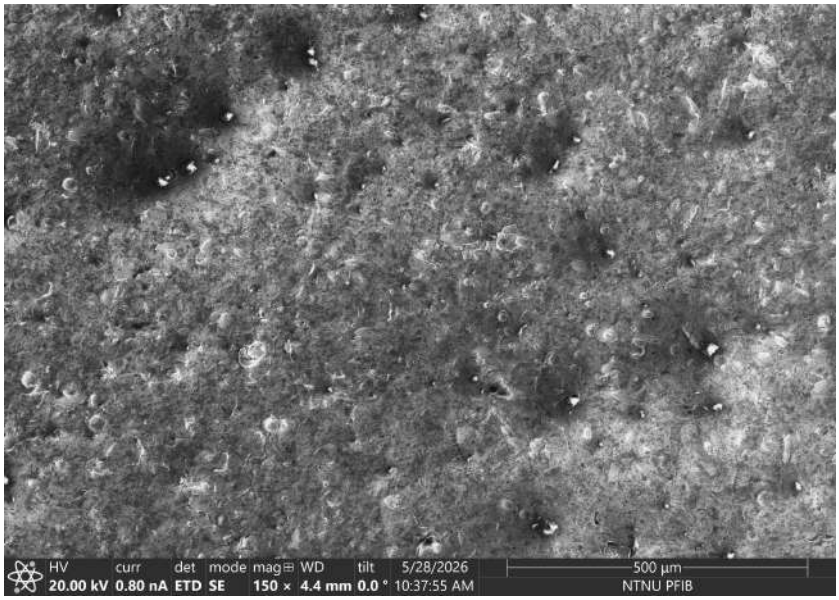

Figure 4.1.4: SEM secondary electron image of the as-peened Ni 725 gauge surface prior to hydrogen pre-charging and tensile testing.

EDS elemental mapping was performed on the as-peened Ni 725 gauge surface prior to tensile testing. The mapped region includes the bulk peened surface and a localised recessed feature visible in the SE overview. Figure 4.1.5 presents the SE overview, composite overlay, and six elemental maps. Across the majority of the mapped area, the Ni, Cr, and Mo maps show a uniform distribution. The oxygen map shows a low, spatially heterogeneous signal across the surface. A localised dark, recessed feature of approximately 10–15 µm is visible in the SE overview. This feature shows elevated Si and O signals, with simultaneous depletion in Ni, Cr, Fe, and Mo. Nb enrichment is also co-located at this site.

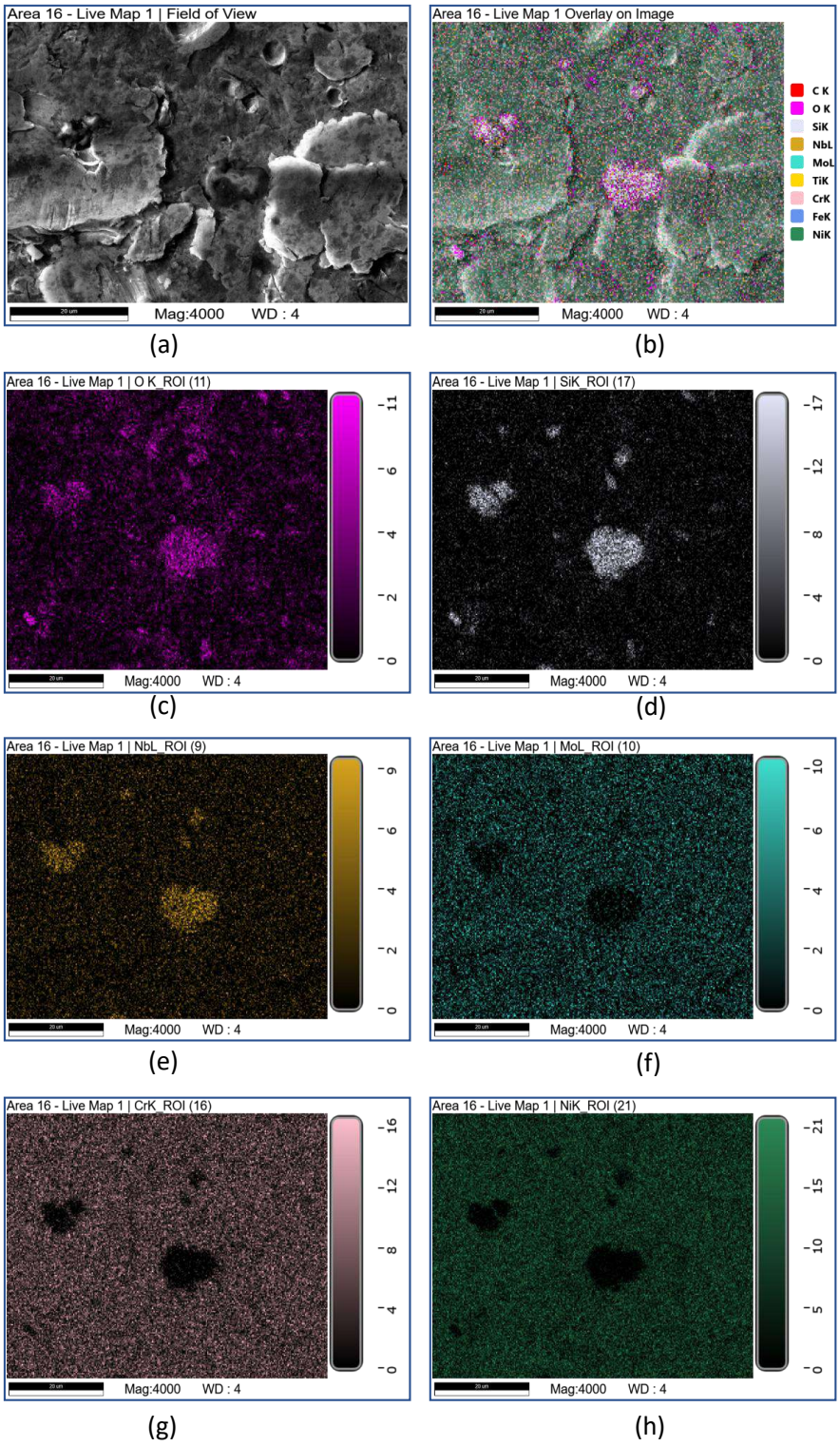

Figure 4.1.5: EDS elemental maps of the as-peened Ni 725 gauge surface prior to tensile testing (4,000×). a) SE overview (b) Composite overlay. (c) O map showing a localised O-rich cluster. (d) Si map showing pronounced Si enrichment. (e) Nb map showing Nb enrichment at the same localised site. (f) Mo map confirming a uniform Mo distribution across the alloy matrix. (g) Cr map showing Cr depletion at the embedded particle region. (h) Ni map confirming uniform Ni distribution in the bulk alloy with depletion at the particle site.

4.1.4 Electrodeposited Nickel-Coated Surface

Figure 4.1.6 shows the electrodeposited Ni-coated Ni 725 gauge surface prior to hydrogen pre-charging and tensile testing. The coating surface shows elongated parallel ridges separated by narrow grooves. Scattered spherical nodules of approximately 0.5–1 µm in diameter are present on the surface. The coating appears continuous and crack-free at this magnification, with no evidence of delamination or macroscopic porosity.

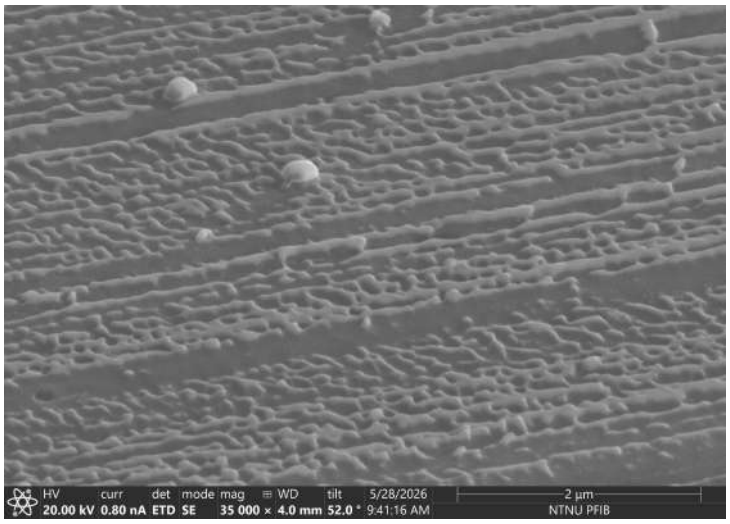

Figure 4.1.6: SEM secondary electron image (35,000×) of the electrodeposited Ni-coated Alloy 725 surface prior to hydrogen pre-charging and tensile testing.

EDS elemental mapping was performed on the FIB-prepared cross-section of the electrodeposited Ni-coated specimen prior to tensile testing. Figure 4.1.7 presents the SE overview, composite overlay, and four selected elemental maps. The SE image shows the Ni coating in the upper region and the Ni 725 substrate in the lower region. The Ni map shows a uniform signal throughout the electrodeposited layer, with no compositional gradients or depletion within the coating. The oxygen map shows a localised O-enriched band at the outermost surface of the Ni coating. The Cr and Mo maps show low, uniform signals confined to the substrate region.

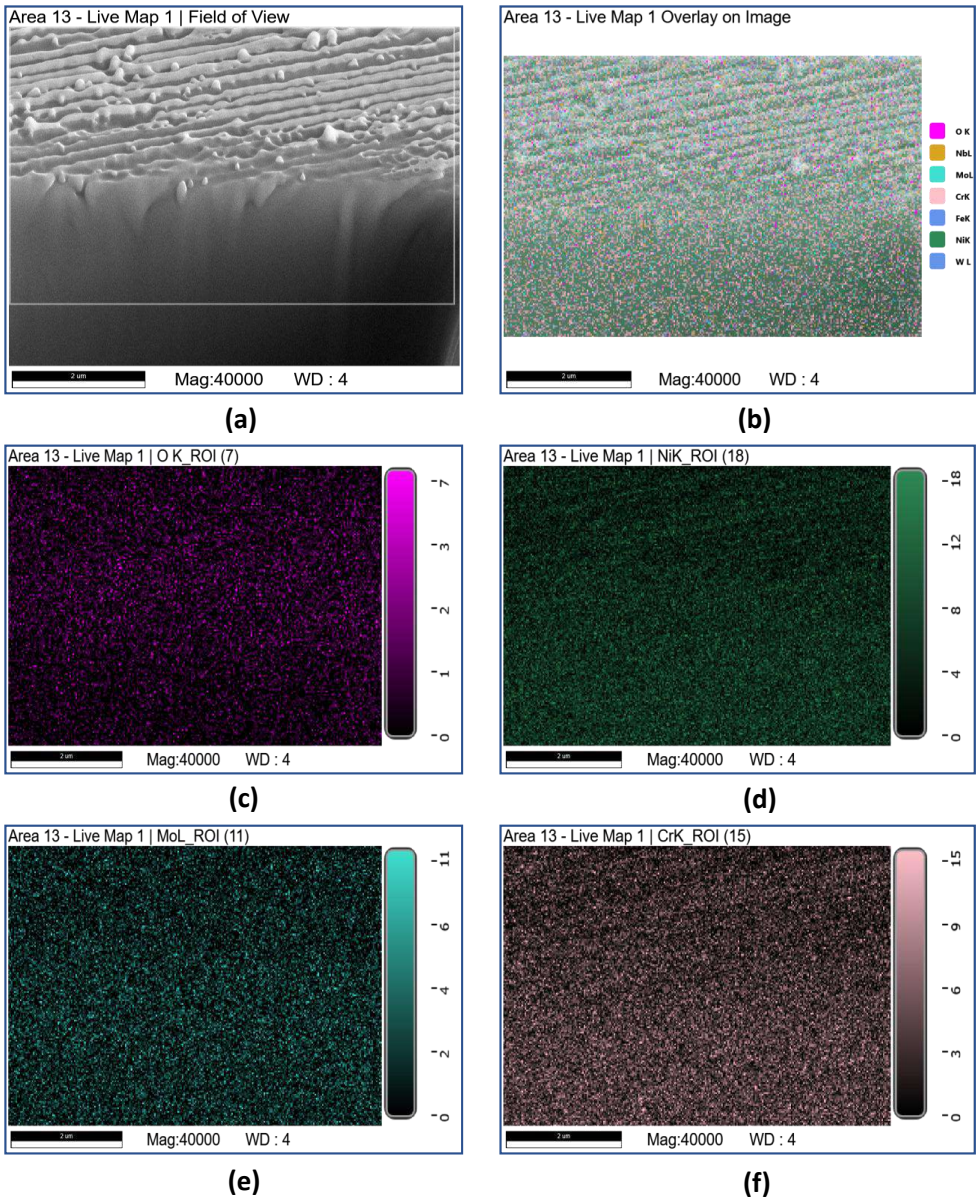

Figure 4.1.7: EDS elemental maps of the FIB-prepared cross-section of the electrodeposited Ni-coated Ni 725 specimen prior to tensile testing. (a) SE overview showing the columnar Ni coating (upper region). (b) Composite overlay of all detected elements. (c) O K map (d) Ni K map confirming uniform Ni distribution throughout the full coating thickness. (e) Mo L map showing low background signal from the substrate. (f) Cr K map showing uniform low-level Cr signal confined to the substrate region.

4.1.5 Gold-Sputtered Surface

Figure 4.1.8 shows the gold-sputtered Ni 725 gauge surface prior to hydrogen precharging and tensile testing. A thin Au film was deposited onto the ground gauge section by DC magnetron sputtering. The surface shows a finely textured, slightly nodular topography consisting of closely packed Au particles.

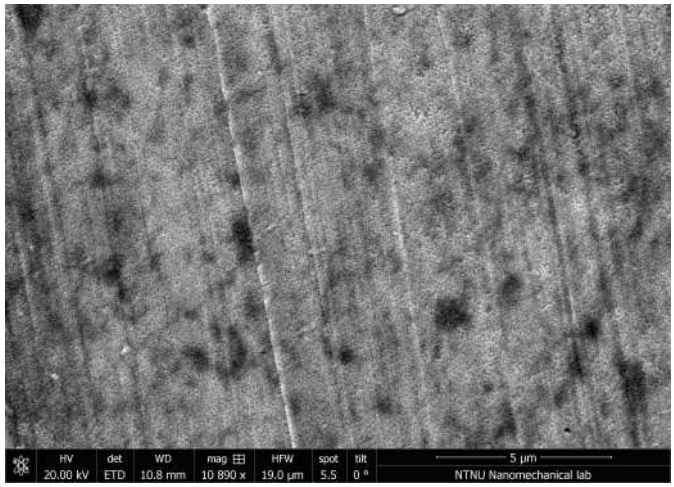

Figure 4.1.8: SEM image of the gold-sputtered Alloy 725 gauge surface

To complement the SEM observations, EDS elemental mapping was performed on the gold-sputtered surface prior to tensile testing. The analysed region shows predominance of the Au surface layer, the Au/Ni 725 interface, as a portion of the underlying substrate. No additional peaks from other metallic elements are detected above the background noise level in this spectrum. Figure 4.1.9 shows the Ni and Au distributions in this area.

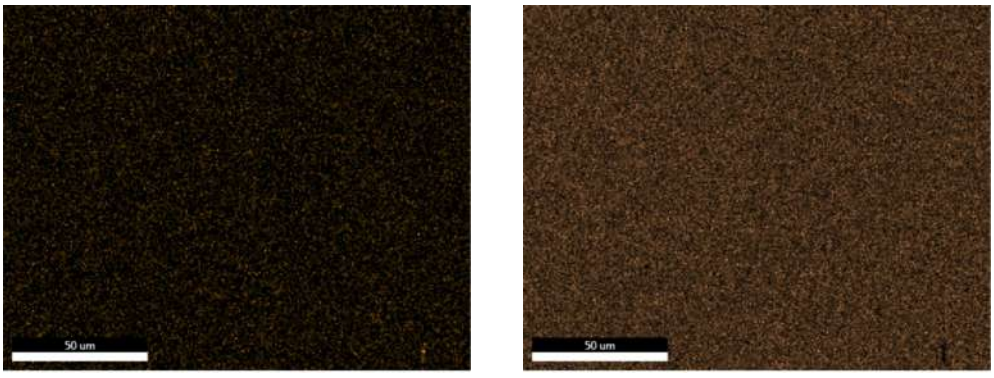

Figure 4.1.9: EDS elemental maps of the gold-sputtered Ni 725 gauge surface prior to tensile testing.(a) Ni map (b) Au map.

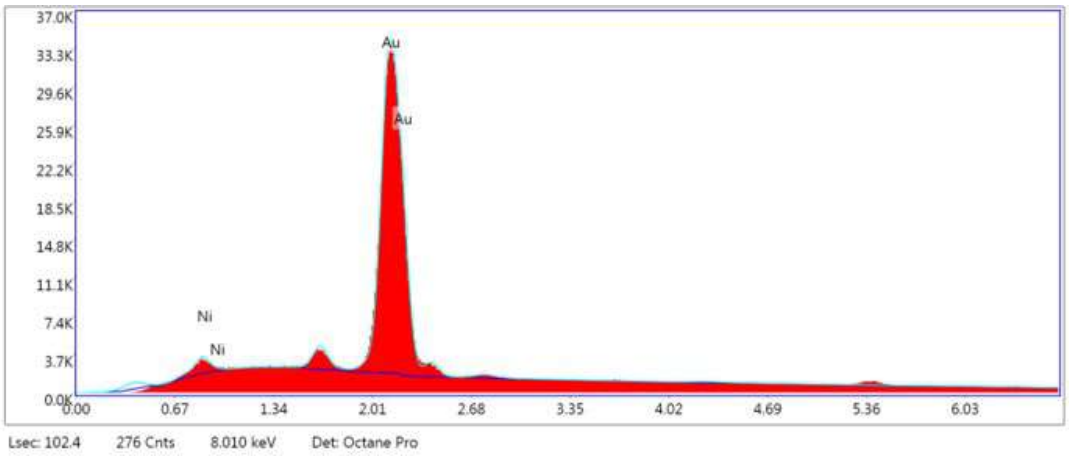

Figure 4.1.10: EDS elemental composition of the gold-sputtered Ni 725 gauge surface.

4.2 Tensile test results

This section presents the results obtained from the in-situ tensile tests performed inside the SEM. For each condition, both the stress–strain response and a video of the gauge section were recorded for each condition. The stress–strain curves for the air (uncharged), 24 h hydrogen-charged and 72 h hydrogen-charged conditions are shown in Figures 4.2.1–4.2.2.

4.2.1 Air & 24 h hydrogen-charged conditions

The stress–strain curves for all surface conditions are shown in Figure 4.2.1. Air-tested (uncharged) specimens are plotted with dashed lines and 24 h hydrogen-charged specimens with solid lines. The ground 2000-grit air condition serves as the primary uncharged reference. For the gold-sputtered and Ni-plated conditions, only hydrogen-charged specimens were tested; no uncharged air baseline was obtained for these two conditions.

All air-tested specimens show a clear elastic regime, a gradual yield transition, and plastic deformation extending to fracture strains between approximately 28 and 36%. The ground 2000-grit air specimen reaches the highest fracture strain at 35.99%, the EDM air specimen at 35.33%, and the peened air specimen at 27.99%.

After 24 h hydrogen pre-charging, all specimens show a reduction in fracture strain compared to the air condition. The UTS values remain broadly similar across the surface conditions except for Ground 2000 sample being higher. The Ni-plated specimen shows the lowest fracture strain of all 24 h charged conditions at 10.73%, with a UTS of 1082.8 MPa.

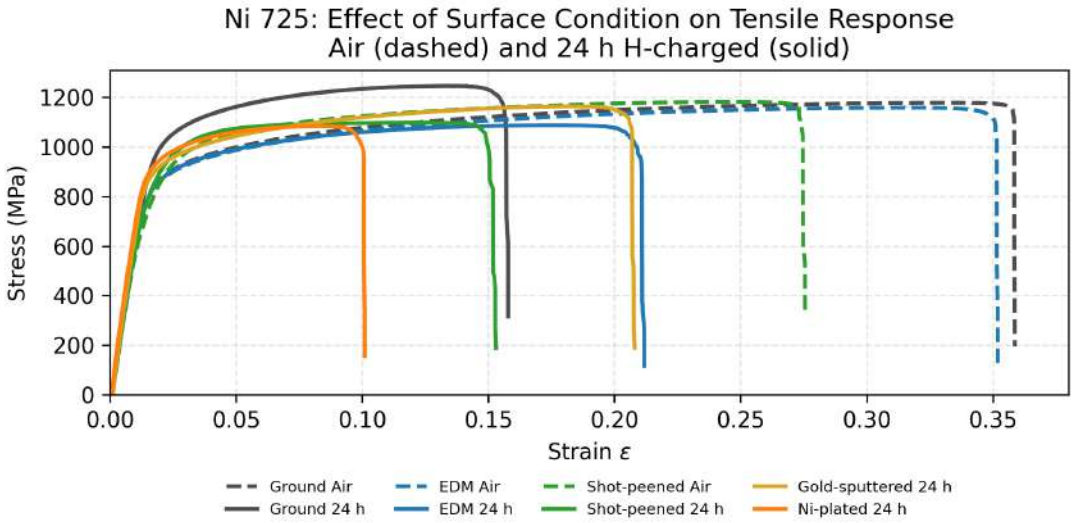

Figure 4.2.1: Stress–strain curves comparing the air (uncharged) condition with the 24 h hydrogen-charged of different surface condition.

4.2.2 72 h Hydrogen-Charged Condition: Ground 2000-Grit

A 72 h hydrogen pre-charging test was performed on the ground 2000-grit specimen only. Figure 4.2.2 compares the ground air reference with the ground 72 h charged specimen. The 72 h specimen shows a further reduction in fracture strain to 9.35%, compared with 16.01% at 24 h and 35.99% in air. The UTS drops to 1098.0 MPa, compared with 1245.2 MPa at 24 h. The post-UTS drop is steep and abrupt in the 72 h curve.

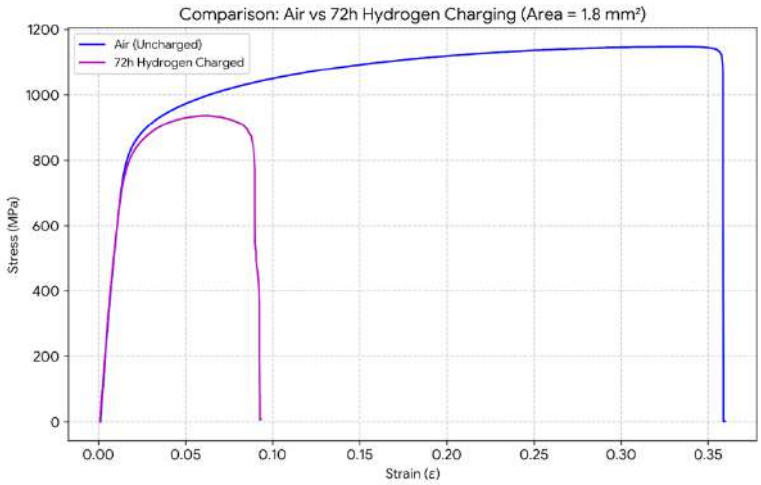

Figure 4.2.2: Stress–strain curves comparing the air (uncharged) condition with the 72 h hydrogen-charged condition.

4.2.3 Summary of tensile properties

The key tensile properties extracted from the stress–strain curves are collected in Table 4.2.1. Engineering stress was calculated as $\sigma = P/A$, where P is the applied load and A is the initial cross-sectional area, and engineering strain as $\varepsilon = \Delta L/L_0$, where ΔL is the change in gauge length and L_0 is the initial gauge length. The ultimate tensile strength (UTS) is given by $\sigma_{\max} = P_{\max}/A$, and the total elongation is expressed as

$$\%\mathrm{EL} = \frac{\Delta L_{\mathrm{fracture}}}{L_0} \times 100. \tag{4.1}$$

Table 4.2.1: Summary of tensile properties for Ni 725 under different surface conditions and hydrogen charging states.

Surface condition	**Charge state**	**UTS** (MPa)	**Elongation** (%)
Ground 2000-grit	Air (uncharged)	1177.2	35.99
Ground 2000-grit	24 h H-charged	1245.2	16.01
Ground 2000-grit	72 h H-charged	1098.0	9.35
EDM	Air (uncharged)	1157.6	35.33
EDM	24 h H-charged	1086.4	21.30
Shot-peened	Air (uncharged)	1181.4	27.99
Shot-peened	24 h H-charged	1097.5	15.92
Gold-sputtered	24 h H-charged	1162.8	20.98
Ni-plated	24 h H-charged	1082.8	10.73

The UTS values for all air-tested conditions are broadly consistent, ranging from 1157 to 1181 MPa. The ground 24 h charged specimen shows a slightly higher UTS of 1245.2 MPa compared to its air baseline. All 24 h charged conditions show a reduction in elongation compared to the air condition, with the Ni-plated condition showing the lowest elongation at 10.73%. The 72 h ground specimen shows a further reduction in both elongation (9.35%) and UTS (1098.0 MPa) compared to the 24 h charged condition.

4.2.4 Hydrogen embrittlement index

To calculate the loss in ductility, the hydrogen embrittlement index was calculated based on the loss of fracture strain relative to the air condition. The hydrogen embrittlement index, I_{HE}, is defined as

$$I_{\mathrm{HE}} = \frac{\varepsilon_{\mathrm{Air}} - \varepsilon_{\mathrm{H}}}{\varepsilon_{\mathrm{Air}}} \times 100\ \%, \tag{4.2}$$

where $\varepsilon_{\mathrm{Air}}$ is the fracture strain in the uncharged condition and ε_{H} is the fracture strain after hydrogen charging (24 h or 72 h). The index is therefore a dimensionless measure of the relative ductility loss attributable to hydrogen, with a value of 0% indicating no embrittlement and 100% indicating complete loss of ductility. For the gold-sputtered and Ni-plated conditions, no separate air baseline was

obtained. Since both coatings are applied at the nanometre scale and are not expected to alter the bulk mechanical response of the material, the ground 2000-grit air fracture strain (35.99%) was used as the reference for these two conditions.

The calculated values are listed in Table 4.2.2. Among the 24 h charged conditions, the Ni-plated specimen shows the highest I_{HE} of 70.2%, with a fracture strain reduced from 35.99% in air to 10.73% after charging. The ground 2000-grit specimen follows with an index of 55.5%, corresponding to a drop in fracture strain from 35.99% to 16.01%. The peened and gold-sputtered specimens show intermediate indices of 43.1% and 41.7%, with fracture strains of 15.92% and 20.98% respectively. The EDM specimen shows the lowest index of 39.7%, with a fracture strain of 21.30% after 24 h charging.

Table 4.2.2: Hydrogen embrittlement index for Ni 725 under different surface conditions.

Surface condition	$\varepsilon_{f,\mathrm{air}}$ (%)	$\varepsilon_{f,24\,\mathrm{h}}$ (%)	I_{HE} (%)
Ground 2000-grit	35.99	16.01	55.5
EDM	35.33	21.30	39.7
Shot-peened	27.99	15.92	43.1
Gold-sputtered	35.99*	20.98	41.7
Ni-plated	35.99*	10.73	70.2

*Ground 2000-grit air value used as reference.

4.3 Surface Microstructure Analysis

4.3.1 EDM-Finished Surface: Air-Tested (Uncharged)

Figure 4.3.1 shows the fracture surface of the EDM-finished Ni 725 specimen tested in air (uncharged) after tensile testing. The fracture cross-section shows visible necking across the gauge width. The surrounding gauge surface retains the as-machined EDM morphology. No large cracks originating from the gauge surface are observed but the surface is seen to have failed ductile.

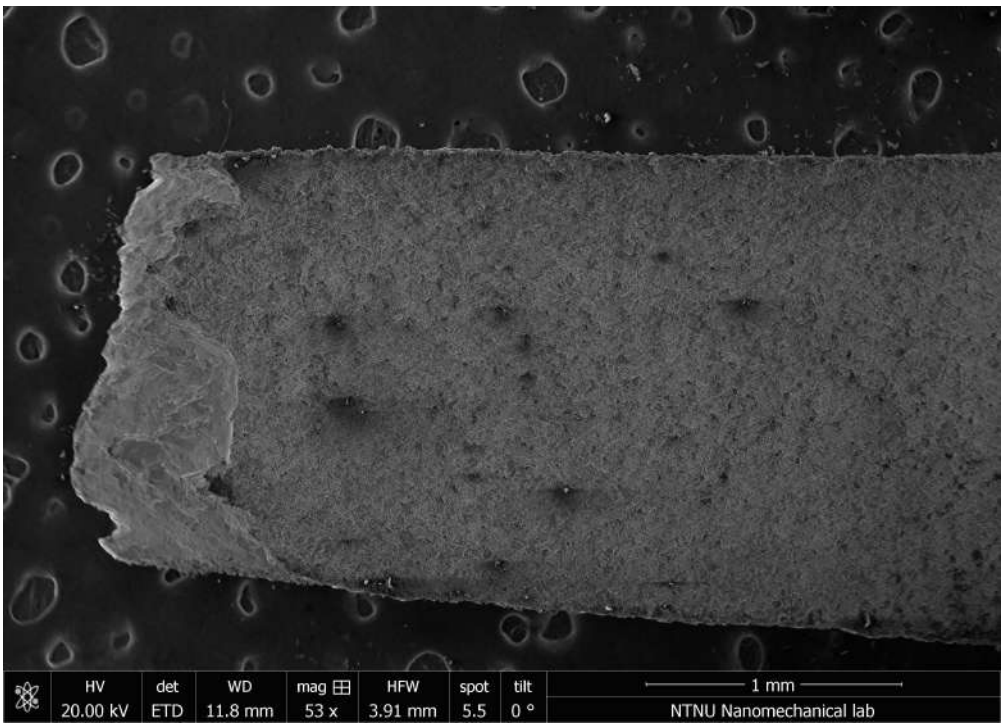

Figure 4.3.1: SEM overview of the EDM-finished Ni 725 fracture surface after tensile testing in air (uncharged) (53×).

4.3.2 EDM-Finished Surface: 24 h Hydrogen Pre-Charged

Figure 4.3.2 shows the fracture surface of the EDM-finished Ni 725 specimen after 24 h hydrogen pre-charging and tensile testing. The low-magnification overview (Figure 4.3.2a) shows a macroscopically flat cross-section with limited necking. No prominent shear lips are present along the specimen perimeter at this magnification. Figure 4.3.2b shows the crack initiation region at the specimen edge, where a step-like profile is visible from which the primary fracture plane propagates inward.Figure 4.3.2c presents a high-magnification view (2,577×) of the fracture surface. Two morphologically distinct zones are present, separated by a well-defined boundary. The left portion shows an irregular surface with deformed irregular fragments and open cracks. The right portion consists of flat, smooth facets with angular edges and minimal surface relief.

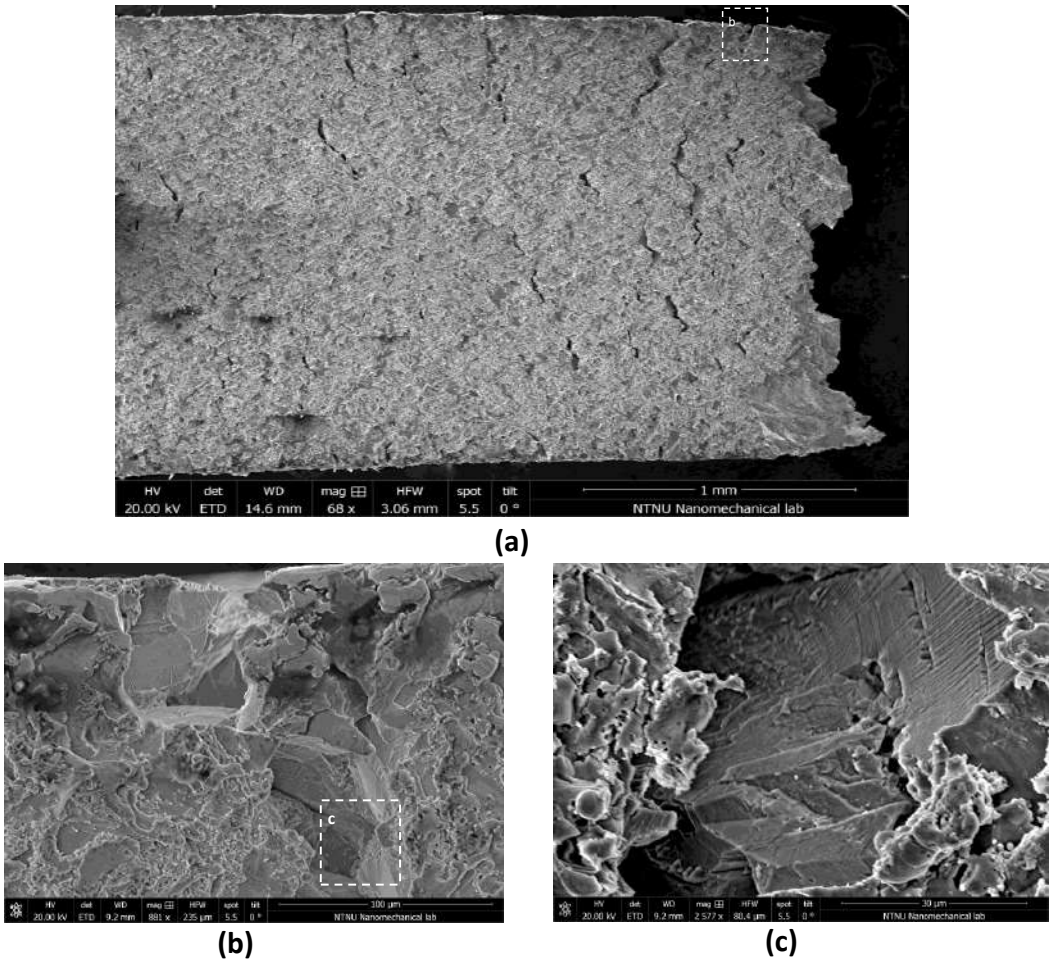

Figure 4.3.2: Fracture surface of the EDM-finished Ni 725 specimen after 24 h hydrogen pre-charging and tensile testing. (a) Low-magnification overview (68×). (b) Intermediate magnification of the region marked in (a) showing crack initiation site. (c) High-magnification SEM image (2577×) of the crack interior.

4.3.3 Grinded Surface: Air-Tested (Uncharged)

The SEM observations in Figures 4.3.3 and 4.3.4 shows the surface condition of the air-tested uncoated Ni 725 specimen after tensile testing. The 50× overview in Figure 4.3.3 shows the primary fracture face on the left-hand side of the gauge section. The adjacent gauge surface contains a broad region of pronounced surface rumpling along with shallow surface cavities and void-like features is visible. Several slip bands are notably visible from the overview image

Higher-magnification images in Figure 4.3.4 show typical features within this deformed zone. In image (a), several elongated surface cavities and step-like height offsets are observed along the gauge surface. Image (b) shows a cluster of coalesced void-like features located closer to the primary fracture, together with a dense network of slip bands. Image (c) reveals extensive slip traces and surface rumpling in the surrounding material.

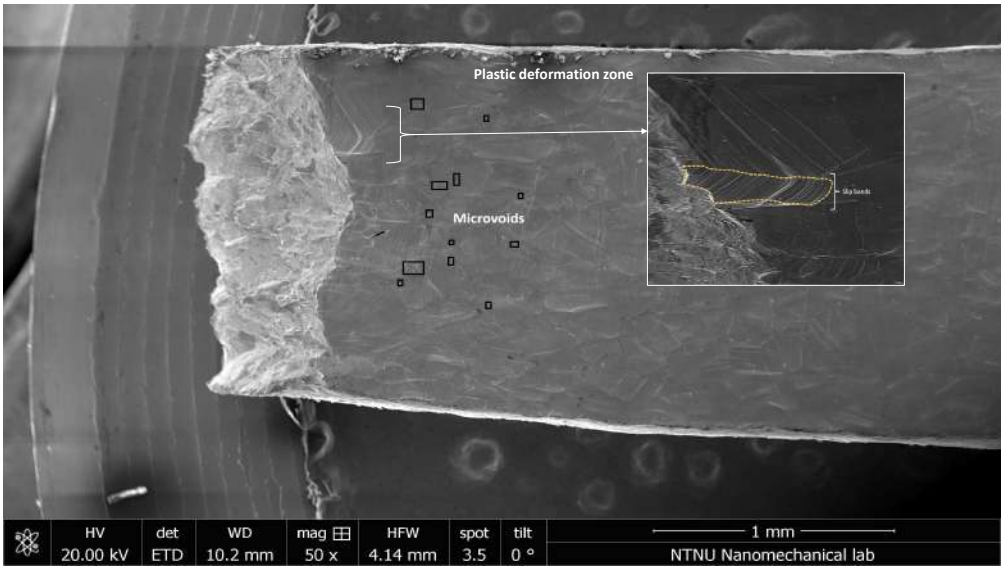

Figure 4.3.3: Overview of the air-tested uncoated Ni 725 specimen after tensile testing, showing the primary fracture face on the left and a broad plastic deformation zone extending into the gauge section.

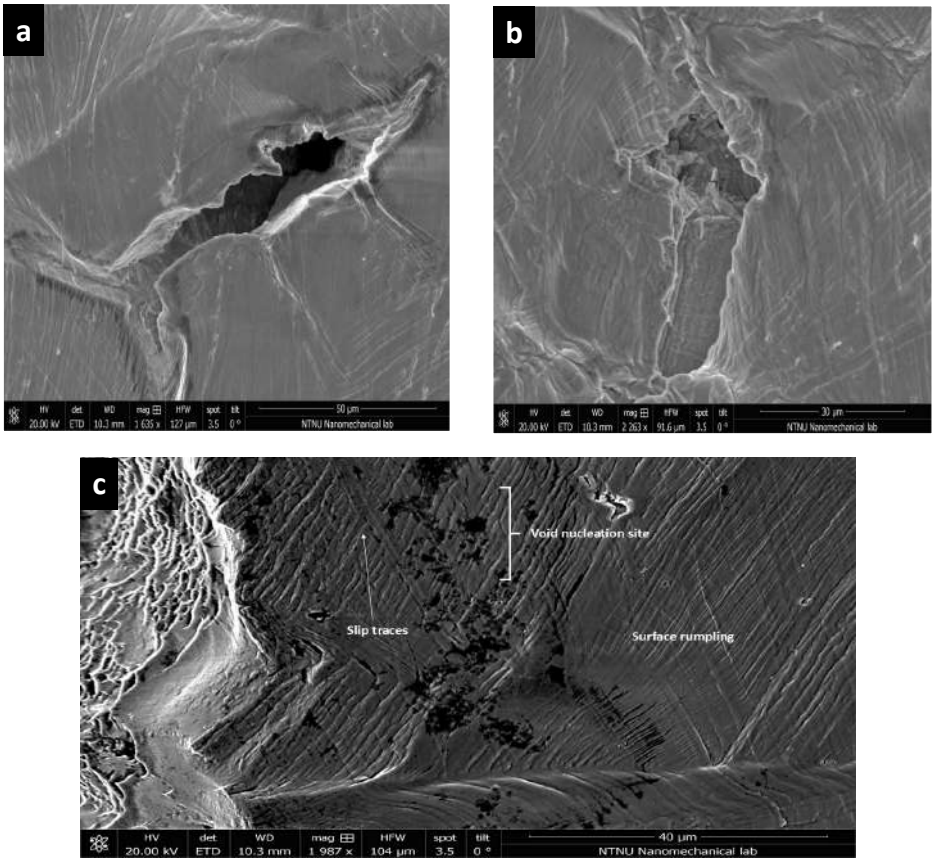

Figure 4.3.4: SEM surface analysis of the air-tested uncoated Ni 725 (a) Higher-magnification view showing elongated surface cavities and step-like offsets. (b) Region closer to the fracture with clustered void-like features and a dense slip-band network. (c) Slip traces and surface rumpling in the plastically deformed zone.

4.3.4 Grinded Surface: 24 h Hydrogen Pre-Charged

The SEM surface analysis in Figure 4.3.5 presents the gauge section of the Grinded Ni 725 specimen following 24 h electrochemical hydrogen pre-charging and tensile testing to fracture. At low magnification, the primary fracture face and the adjacent gauge surface are visible. The fracture edge has a moderately irregular profile, and a zone of surface damage extends along the gauge face near the fracture plane.

Figure 4.3.6 presents higher-magnification SEM images from selected regions on the gauge surface. In image (a), several short secondary surface cracks are present away from the primary fracture plane, mostly oriented perpendicular to the tensile axis. The cracks have sharp, well-defined edges with limited plastic blunting at their tips. Image (b) shows a higher-magnification view of an individual secondary surface crack within a locally deformed region. slip bands are visible on both sides of the crack, forming narrow deformation bands in the surrounding material. Image (c) shows a region further from the primary fracture, where the brittle tear ridges are seen in the plastically deformed zone.

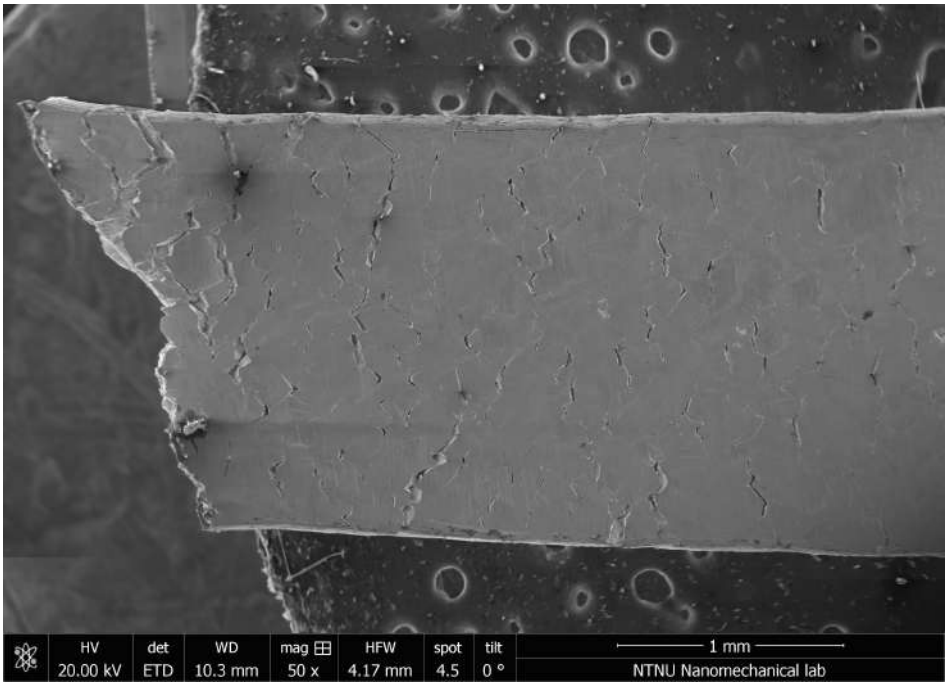

Figure 4.3.5: Overview of the uncoated Ni 725 specimen after 24 h hydrogen charging and tensile testing.

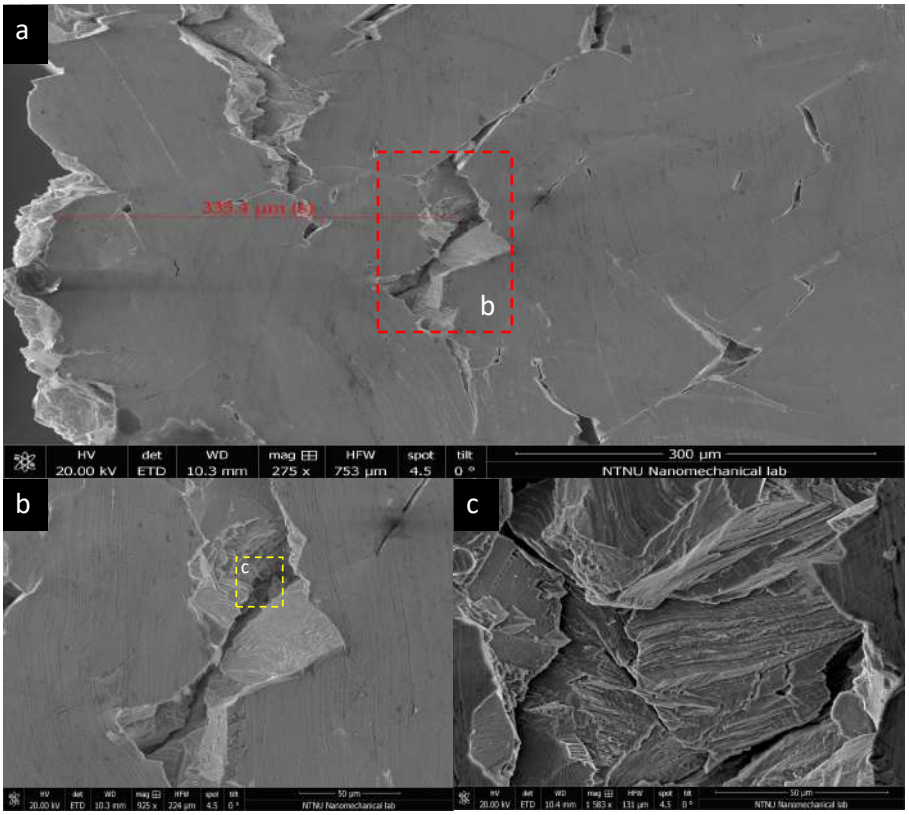

Figure 4.3.6: Fracture surface of the uncoated Ni 725 specimen after 24 h hydrogen pre-charging and tensile testing (a) Overview image (b) Intermediate magnification of the marked region in (a),(c) Higher magnification of the marked region in (b).

4.3.5 Grinded Surface: 72 h Hydrogen Pre-Charged

The surface condition of the Grinded Ni 725 specimen following 72 h electrochemical hydrogen pre-charging and tensile testing to fracture is documented in Figures 4.3.7 and 4.3.8. Figure 4.3.7 presents a low-magnification overview of the gauge section. The fracture profile is macroscopically flat with no appreciable necking across the gauge width, and the fracture edge runs nearly perpendicular to the tensile axis. The gauge surface adjacent to the fracture contains a network of secondary surface cracks extending along the gauge face. Most secondary cracks are oriented approximately perpendicular to the loading direction, with some cracks showing a more oblique orientation.

Figure 4.3.8(a) shows the origin of a secondary surface crack at 500×. The crack initiates at a well-defined surface site, and the crack flanks are sharp with limited plastic blunting at the tip. The crack extends into the gauge surface along a mainly straight path. Figure 4.3.8(b) shows the gauge surface near a secondary crack at 900×. Dense, closely spaced planar slip traces are visible in the immediate vicinity of the crack, confined to narrow, nearly parallel bands. The slip traces cross several grains and are interrupted at grain boundaries. Unlike the distributed

slip traces and surface rumpling observed on the air-tested ground specimen Fig: 4.3.3, the damage here is concentrated into widely spaced cracks, with minimal surface deformation between them, indicative of significantly reduced capacity for homogeneous plastic deformation.

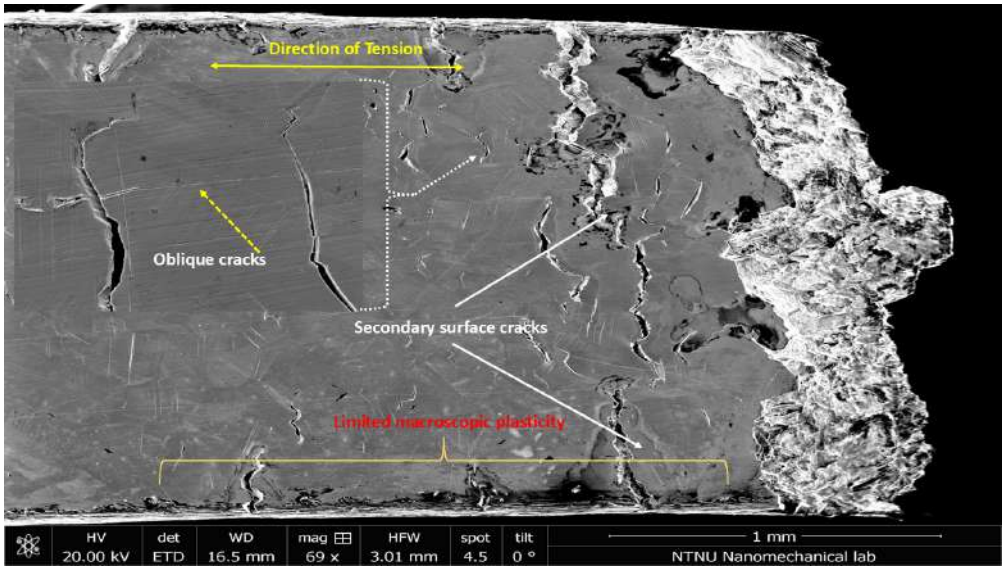

Figure 4.3.7: Overview of the 72 h hydrogen-charged surface at 50×.

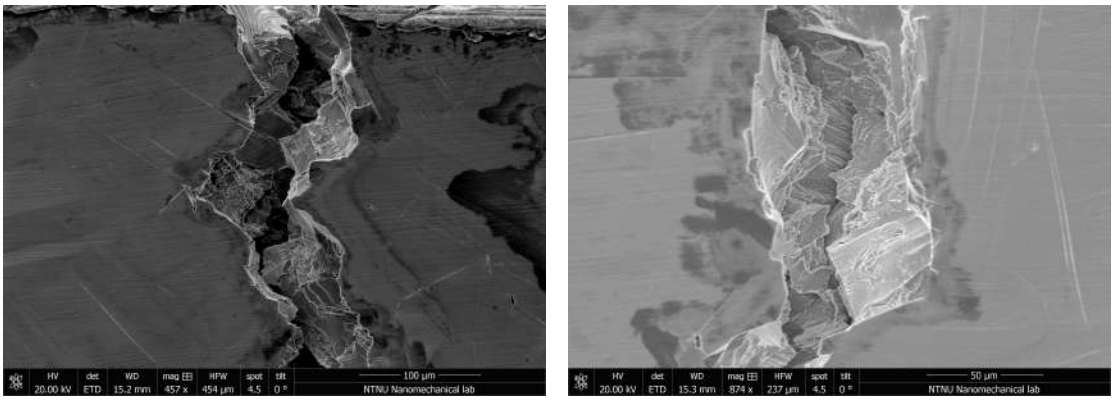

(a) **(b)**

Figure 4.3.8: SEM surface analysis of the uncoated Ni 725 specimen after 72 h hydrogen charging and tensile testing (a) Secondary crack origin at 500× (b) Slip traces at 900×.

4.3.6 Peened Surface: Air-Tested (Uncharged)

Figure 4.3.9 presents a low-magnification SEM overview (51×) of the peened Ni 725 specimen tested in air (uncharged) after tensile testing to fracture. The fracture edge is irregular and jagged across the full gauge width, with macroscopic necking visible at the fracture end of the gauge section, indicating substantial plastic deformation prior to final separation.

The fracture edge is irregular and jagged across the gauge width, and macroscopic necking is visible at the fracture end of the gauge section. The fracture profile is non-planar and varies in height across the cross-section. The inlaid magnified image shows a ductile tear crack at (1,933×). The difference between the Grinded 2000 sample in Figure 4.3.3 is the absence of visible slip traces, surface rumplings and microvoids which signifies Non-homogeneous plastic deformation due to the compressive residual stress field introduced by peening.

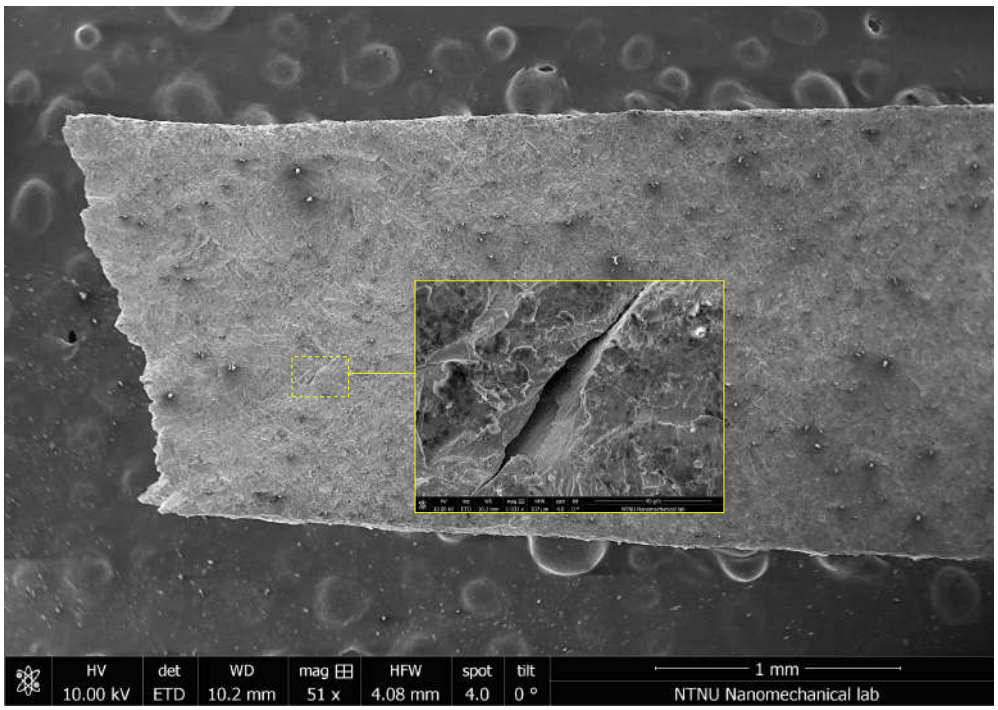

Figure 4.3.9: Low-magnification SEM overview (51×) of the peened Ni 725 specimen tested in air (uncharged) after tensile testing, showing the fracture edge and the gauge section surface.

4.3.7 Peened Surface: 24 h Hydrogen Pre-Charged

The surface condition and fracture morphology of the Peened Ni 725 specimen after 24 h hydrogen pre-charging and tensile testing are presented in Figures 4.3.10 and 4.3.11. Figure 4.3.10 shows a low-magnification overview (46×) of the gauge section after fracture. A network of secondary surface cracks is visible on the broad face of the gauge section adjacent to the primary fracture. The primary fracture edge is stepped and irregular.

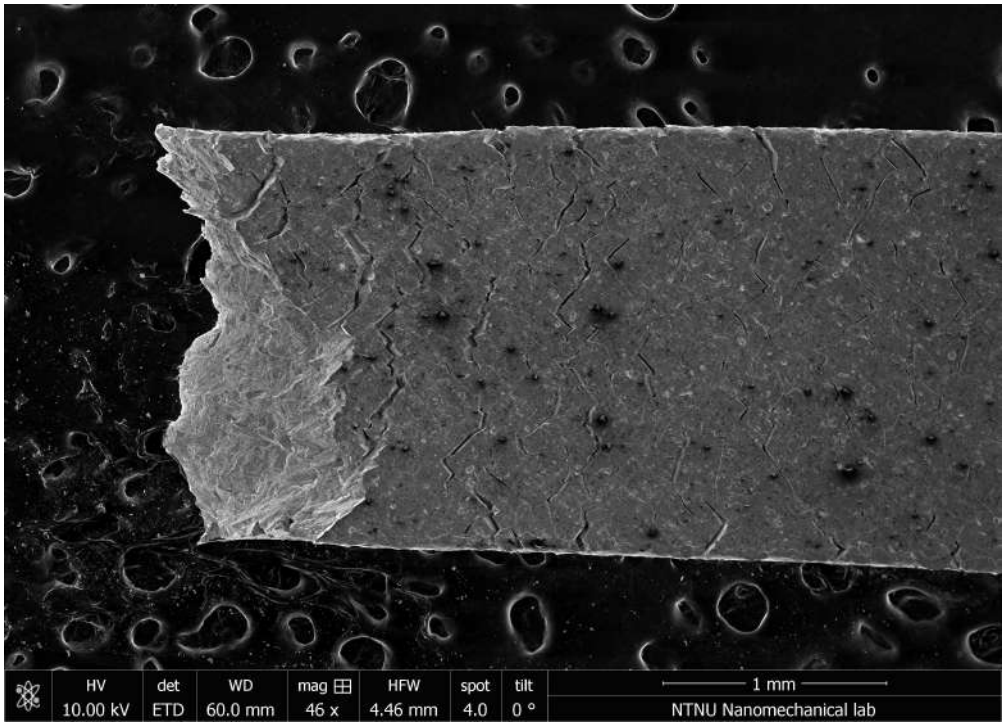

Figure 4.3.10: Low-magnification overview (46×) of the peened Ni 725 specimen after 24 h hydrogen pre-charging and tensile testing, showing the primary fracture edge and the gauge section surface.

Figure 4.3.11 presents SEM images of the secondary cracks at the surface at progressively higher magnifications. The overview image reveals extensive surface cracking and facet formation, while the higher-magnification images highlight sharp crack edges, stepped fracture features, and limited plastic deformation. Figure 4.3.11 (a) presents the overview of the fracture surface at higher magnification with multiple surface cracks distributed across the specimen (b) Higher-magnification image showing a large flat fracture facet with sharp edges and limited evidence of plastic deformation (c) Flat facet adjacent to a crack opening, indicating crack propagation through a brittle fracture region (d) Secondary surface crack extending through the embrittled zone of the fracture surface (e) Crack region bounded by flat facets and step-like fracture features, illustrating localized crack growth within the hydrogen-affected area.

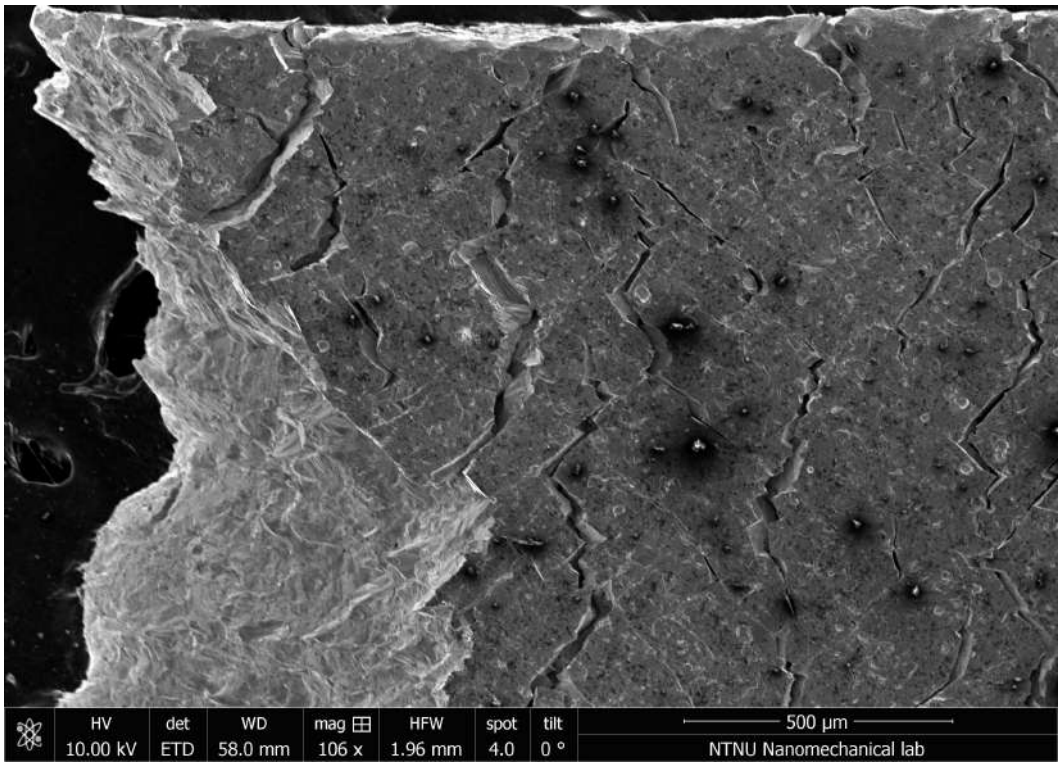

(a)

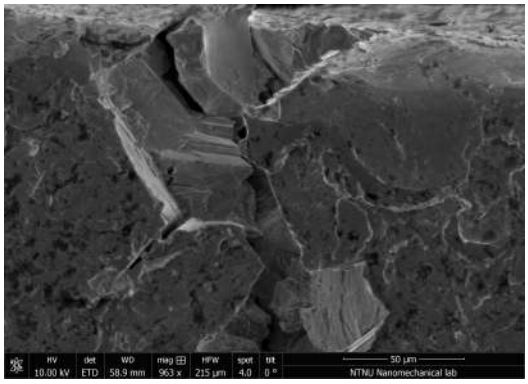

(b)

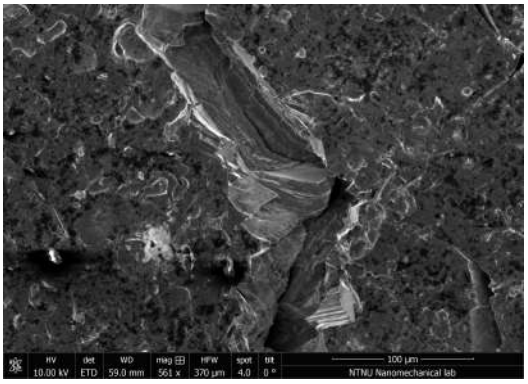

(c)

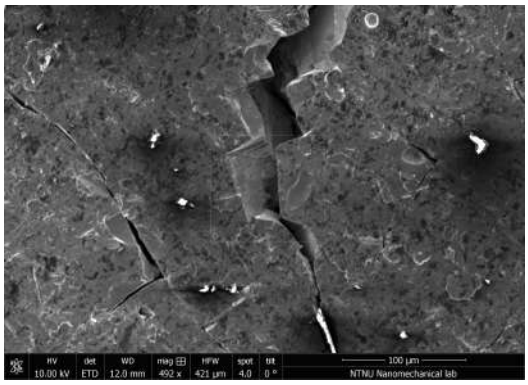

(d)

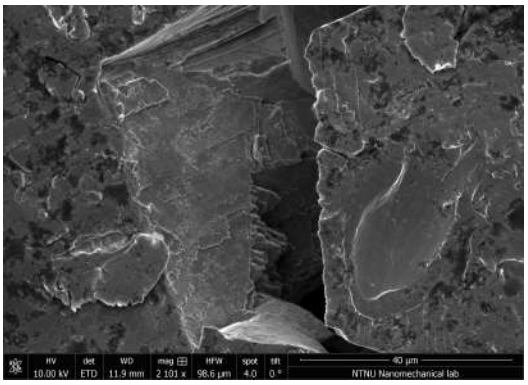

(e)

Figure 4.3.11: SEM images of the shot-peened Ni 725 specimen after 24 h hydrogen pre-charging and tensile testing.

4.3.8 Gold-Sputtered Surface: 24 h Hydrogen Pre-Charged

Figure 4.3.12 presents the fracture-adjacent gauge surface of the Ni 725 specimen coated with a thin magnetron-sputtered gold film and subsequently tensile-tested following 24 h electrochemical hydrogen pre-charging. The fracture edge is macroscopically irregular and locally stepped. The gauge surface outside the immediate fracture zone shows no large-scale delamination or blistering of the Au coating. A sparse distribution of fine secondary surface cracks is visible along the gauge face adjacent to the primary fracture. The fracture surface of the gold sputtered (Figure: 4.3.12) specimen shows fewer secondary cracks on the surface when compared with the 24 h charged grinded sample (Fig: 4.3.5) and the peened sample (Fig: 4.3.10)

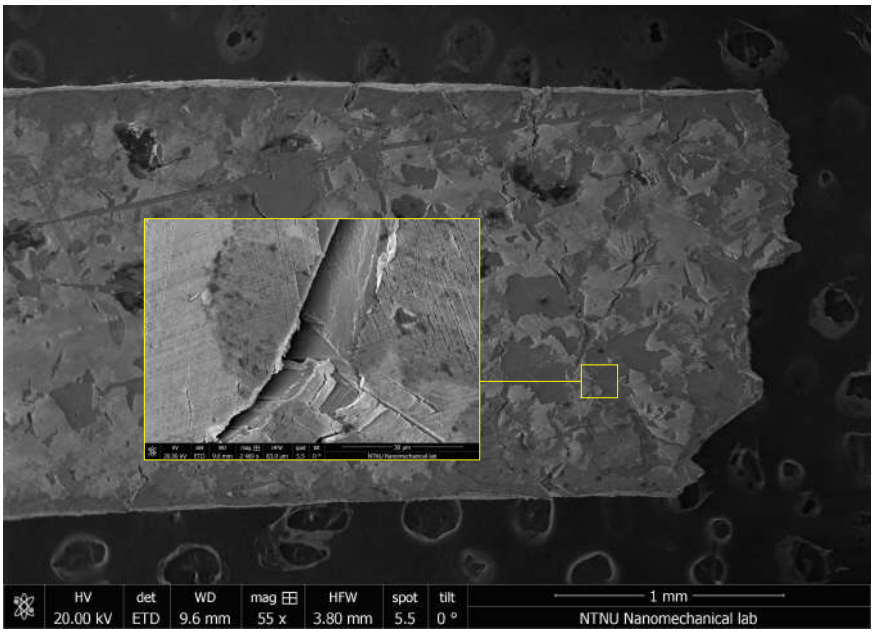

Figure 4.3.12: Overview (55×) of the surface of the gold-sputtered Ni 725 specimen after 24 h hydrogen pre-charging and tensile testing.

Figure 4.3.13 presents higher-magnification SEM images of the region closer to fracture . Image (a) shows the crack origin at 470×. The crack initiates at a surface in the coated gauge section and propagates into the specimen. The crack walls show a faceted, plate-like morphology with limited ductile tearing. Image (b) shows a secondary surface crack on a neighbouring fracture facet at 2,122×. The crack walls are smooth and nearly planar, with only isolated shallow features along the crack walls.

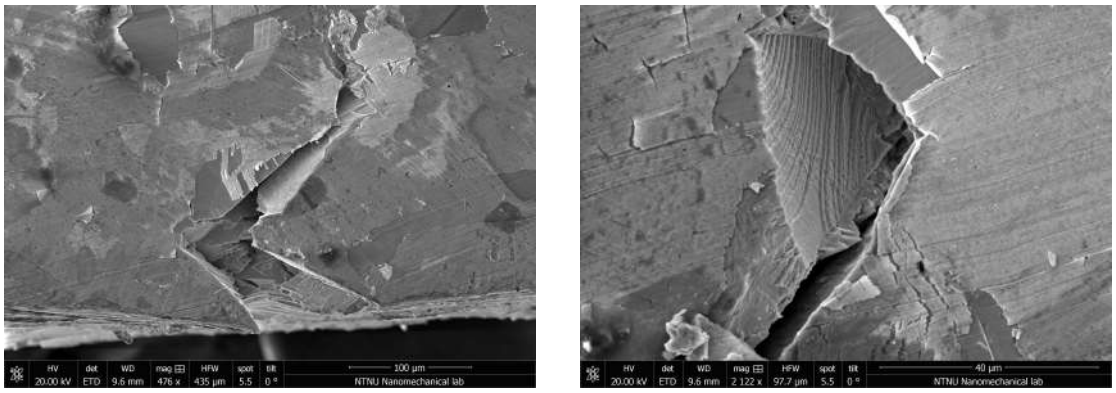

(a) **(b)**

Figure 4.3.13: SEM images of the gold-sputtered Ni 725 specimen after 24 h hydrogen pre-charging and tensile testing. (a) Higher-magnification view of the crack origin. (b) Surface crack wall.

4.3.9 Ni-Coated Surface: 24 h Hydrogen Pre-Charged

The surface morphology of the electrodeposited Ni-coated Alloy 725 specimen after 24 h cathodic hydrogen pre-charging and tensile testing is shown in Figures 4.3.14 and 4.3.15. Figure 4.3.14 presents a low-magnification overview (53×) of the Ni-coated gauge section after testing. When compared to the the 24 h charged EDM sample 4.3.2 grinded sample (Fig: 4.3.5), the peened sample (Fig: 4.3.10) fewer secondary cracks are observed, advancing rapidly to failure without generating extensive secondary damage

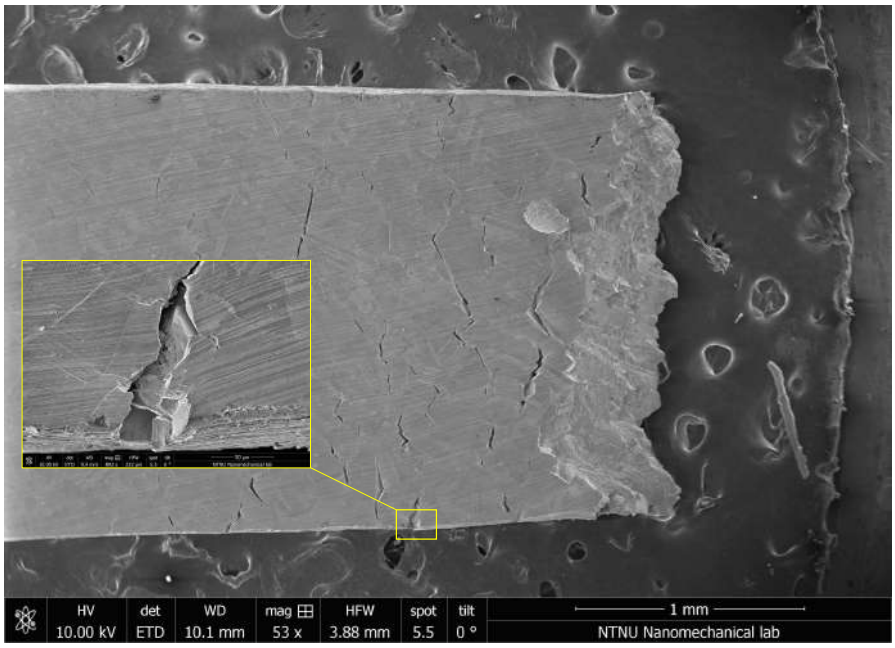

Figure 4.3.14: Low-magnification SEM overview (53×) of the electrodeposited Ni-coated Ni 725 specimen after 24 h hydrogen pre-charging and tensile testing.

Figure 4.3.15 shows a higher-magnification view (1,903×) of the secondary crack indicated in Figure 4.3.14. The crack is open and wedge-shaped, widening towards the surface. Both crack walls display a stepped, striated morphology with multiple Quasi Cleavage facets along the crack propagation direction.

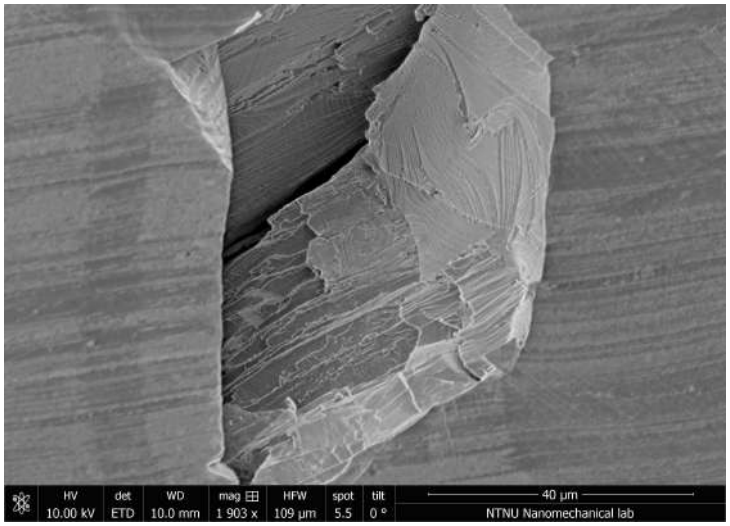

Figure 4.3.15: Higher-magnification SEM image (1 903×) of the secondary surface crack indicated in Figure 4.3.14

4.4 Fractography

4.4.1 EDM-Finished Surface: Air-Tested (Uncharged)

The fracture surface morphology of the EDM-finished Ni 725 specimen tested in air without hydrogen pre-charging is presented in Figures 4.4.1 and 4.4.2. Figure 4.4.1 presents the low-magnification overview (133×) of the full fracture cross-section exhibiting predominant microvoid coalescence and tear ridges distributed throughout. shear lip is present along the corner sides of the fracture. The surrounding gauge surface retains the EDM-machined texture.

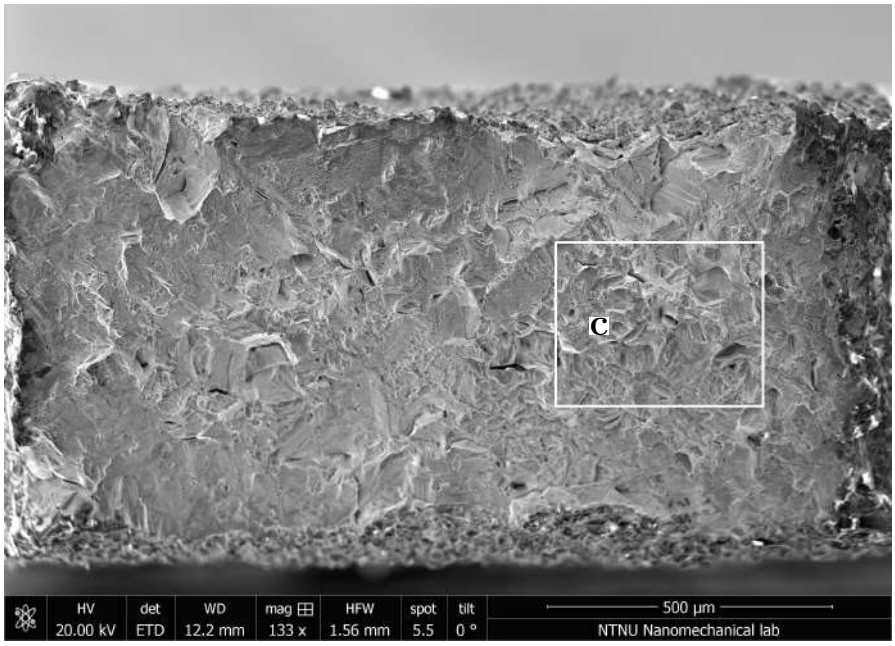

Figure 4.4.1: Low-magnification overview (133×) of the fracture surface of the EDM-finished Ni 725 specimen tested in air, showing the full cross-section, (c), corresponds to the central fracture area shown in Figure 4.4.2c.

Figure 4.4.2 presents higher-magnification images from the left, central, and right quadrants of the fracture surface. Image (a) shows the left-hand fracture quadrant near the specimen edge. Image (b) shows the right-hand fracture quadrant (249×). A similar distribution of elongated cavities near and smaller equiaxed cavities in the interior is observed. Image (c) shows the central fracture region (632×) showing tearing ridges with shallow microvoid coalescence dimples.

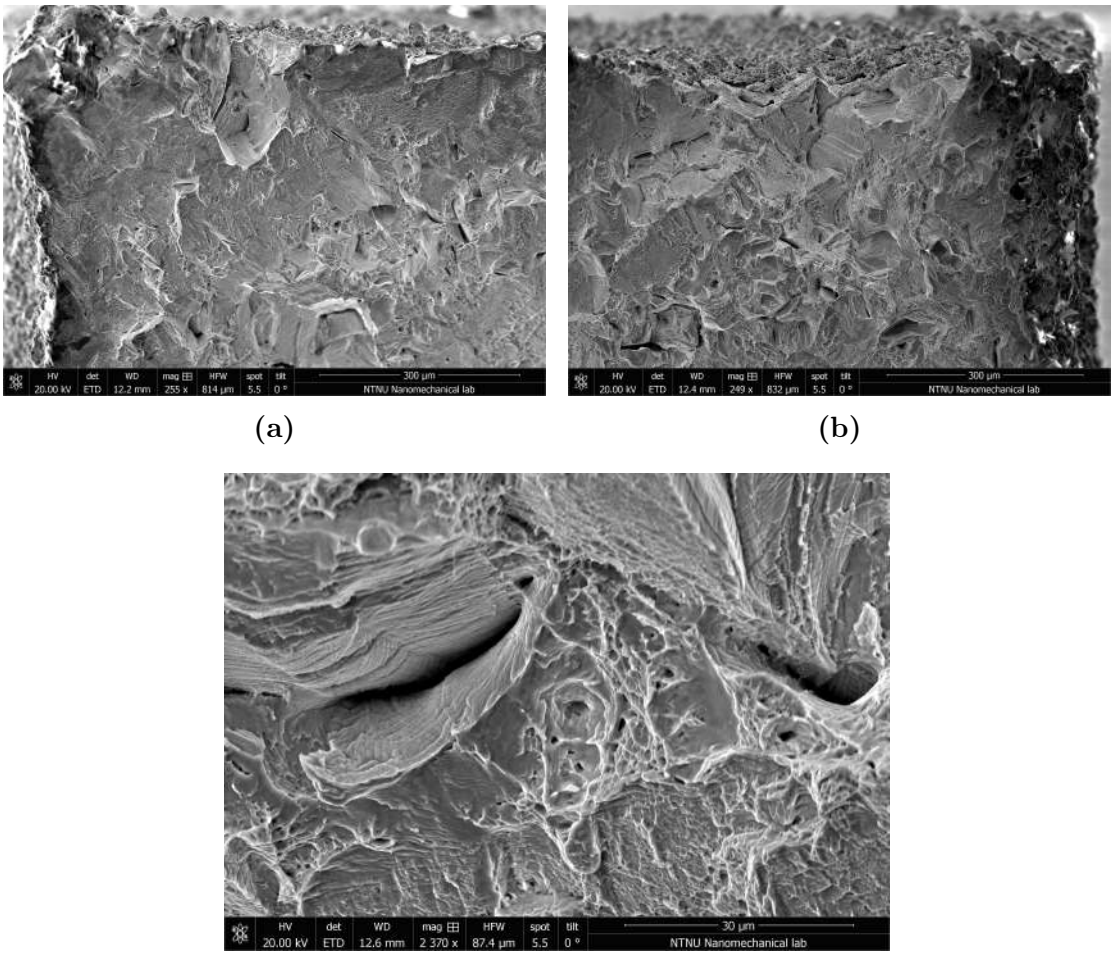

(a) **(b)**

(c)

Figure 4.4.2: SEM fractography of the EDM-finished Ni 725 specimen tested in air. (a) Left-hand fracture quadrant near the specimen edge. (b) Right-hand fracture quadrant. (c) Central region of the fracture surface at higher magnification displaying dimples.

4.4.2 EDM-Finished Surface: 24 h Hydrogen Pre-Charged

Figure 4.4.3 shows the fracture surface of the EDM-finished Ni 725 specimen after 24 h hydrogen pre-charging and tensile testing. After 24 h charging, the EDM shows significant brittle features. Flat cleavge facets are seen in the outer region of the fracture and a gradient between the outer brittle fracture and the inner ductile region is seen.

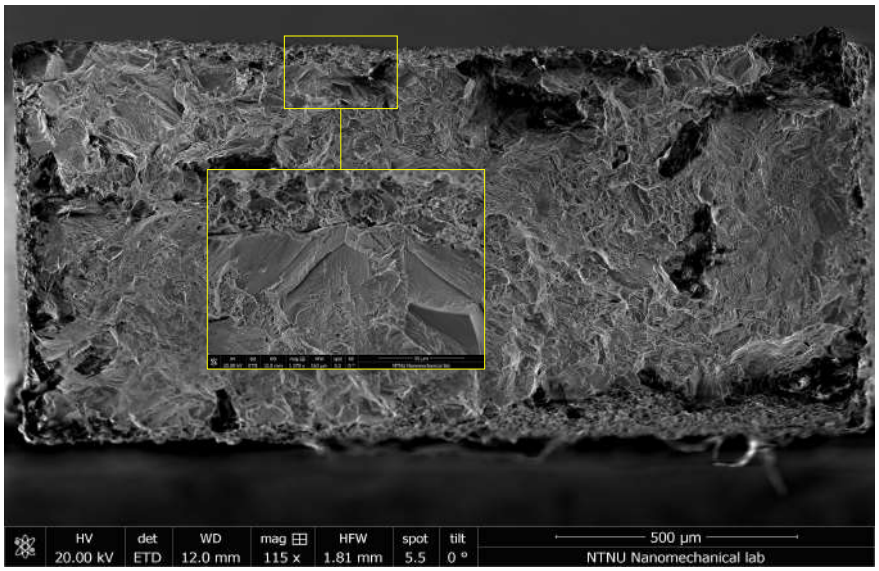

Figure 4.4.3: Low-magnification overview (115×) of the fracture surface of the EDM-finished Ni 725 specimen after 24 h hydrogen pre-charging and tensile testing.

Figure 4.4.4 presents higher-magnification views of the fracture surface. Image (a) shows the left-hand fracture quadrant near the specimen edge (570×). Image (b) shows the right-hand fracture quadrant (298×). Broad stepped crack planes and deep separations are visible across this region. Image (c) shows the central fracture region at 879×. Two morphologically distinct zones are present, the left quadrant shows dimples marking ductile zone and the right portion consists of flat cleavage facets.

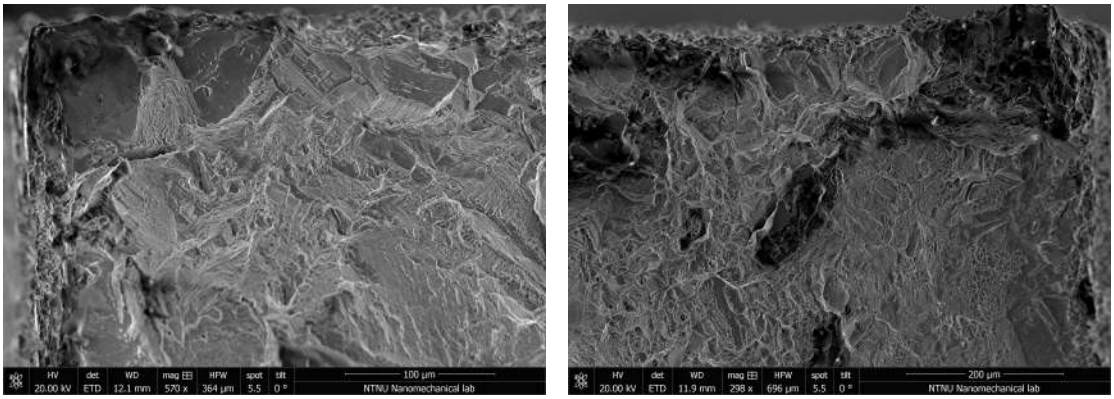

(a) **(b)**

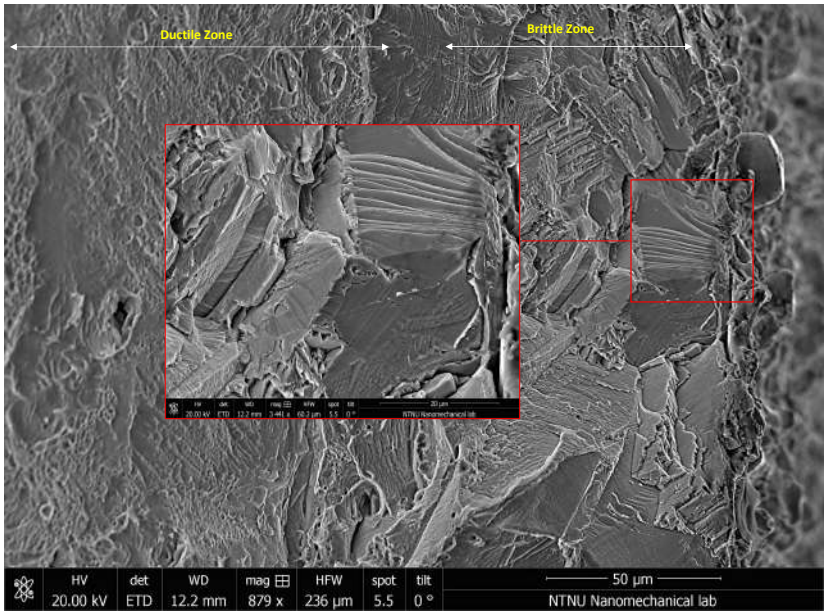

(c)

Figure 4.4.4: SEM fractography of the EDM-finished Ni 725 specimen after 24 h hydrogen pre-charging. (a) Left fracture quadrant near the specimen edge showing large quasi-cleavage plates separated by fine tearing ridges. (b) Right fracture quadrant with broad stepped crack planes and deep interfacial separations. (c) Right-Quadrant wall crack at 879× showing a ductile zone and brittle zone.

4.4.3 Grinded Surface: Air-Tested (Uncharged)

Figure 4.4.5 presents SEM fractographs of the fracture surface of the uncoated Ni 725 specimen ground to 2000-SiC grit and tested in air without hydrogen pre-charging. The specimen shows dimple structures and microvoid coalescence marking ductile behavior.

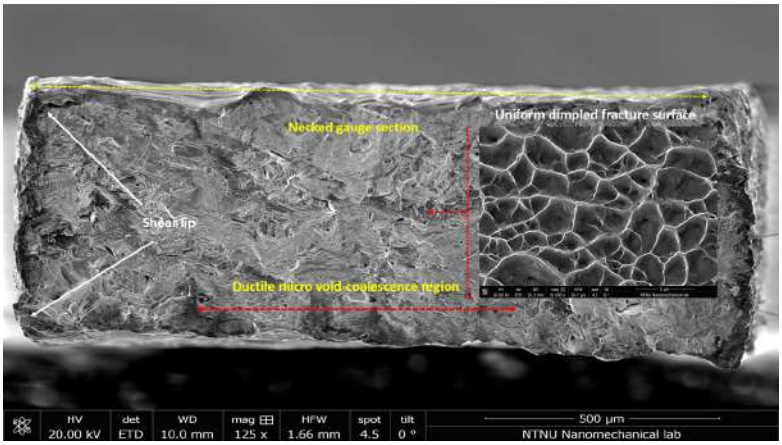

(a)

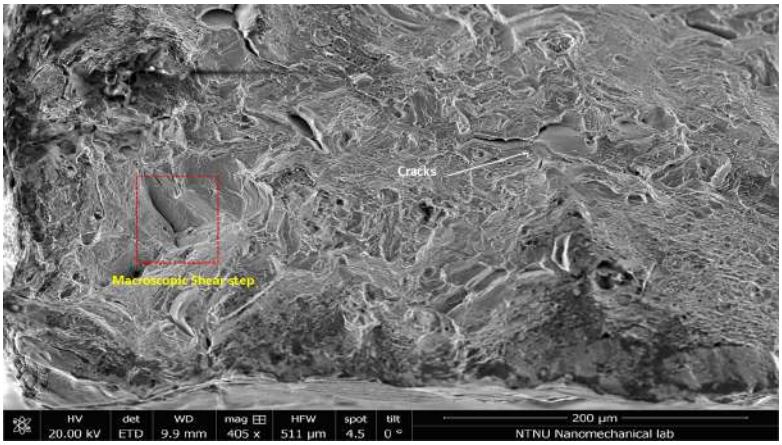

(b)

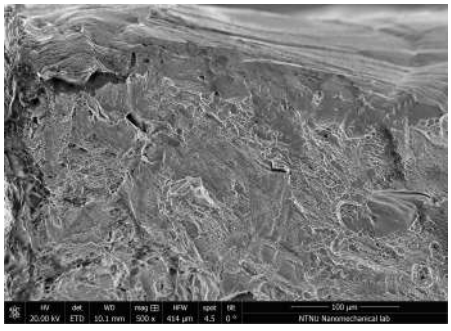

(c)

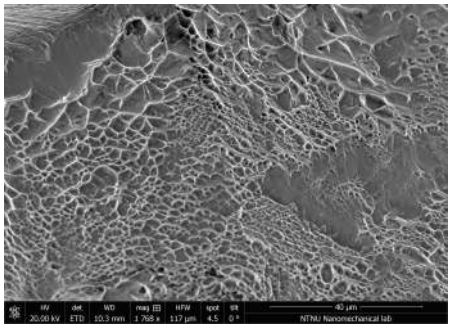

(d)

Figure 4.4.5: SEM fractography of the uncoated Ni 725 specimen tested in air.

Image (a) shows the full fracture cross-section at 125×. The fracture profile is macroscopically irregular, with pronounced necking visible across the gauge section Image (b) shows the lower edge of the fracture surface at 405×. Within this region, cavities are elongated with their long axes oriented obliquely to the tensile axis. Image (c) shows the upper-left quadrant at 500×. Cavities of varying size are distributed across the fracture plane, with larger, more open cavities near the specimen edge. Image (d) shows the central fracture surface at 1,500×.

4.4.4 Grinded Surface: 24 h Hydrogen Pre-Charged

The SEM fractographs in Figures 4.4.6 and 4.4.7 show the fracture surface morphology of the uncoated Ni 725 specimen after 24 h electrochemical hydrogen precharging and tensile testing to fracture. The low-magnification overview (113×) shows a fracture surface that is macroscopically planar, with only limited reduction in cross-sectional area at the fracture plane and no pronounced shear lips at the specimen edges. Three regions of interest, labelled *a,b*, *c*, and *d*, are indicated by yellow boxes and examined at higher magnification in Figure 4.4.7.

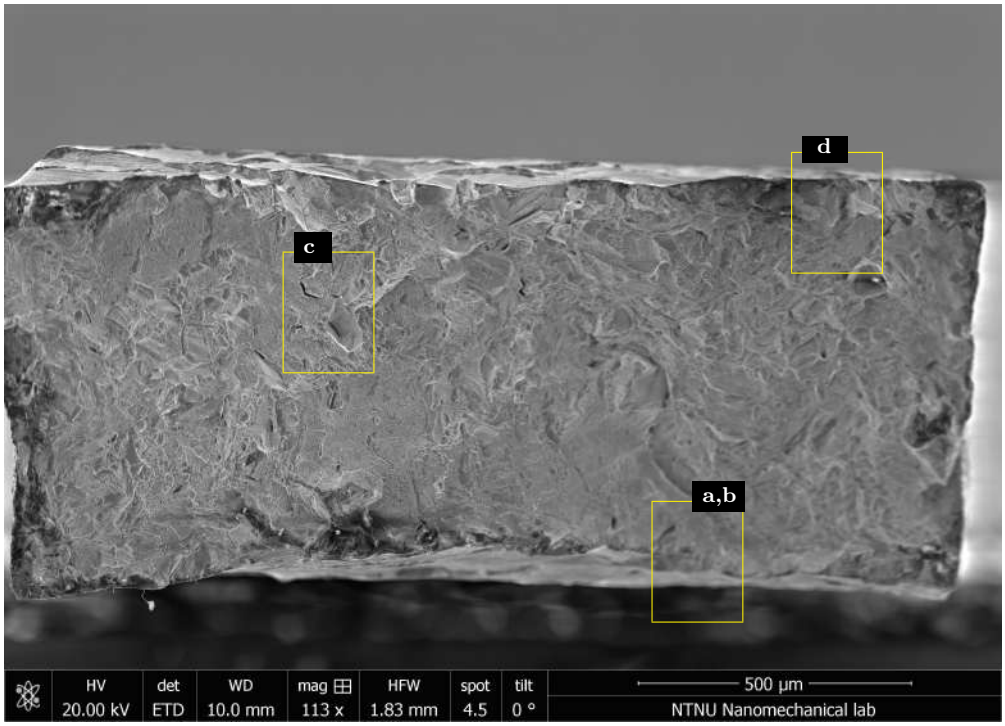

Figure 4.4.6: Overview of the fracture surface of the uncoated Ni 725 specimen after 24 h hydrogen charging and tensile testing. The yellow boxes indicate the regions magnified in Figure 4.4.7.

Figure 4.4.7 Image (a) shows a high-magnification view (2,650×) of region *a,b*. The fracture surface shows finely serrated crack walls, with sharp-edged steps and locally flat facets. Image (b) shows an intermediate-magnification view (459×) of the same region, where a dense network of secondary fracture planes is visible. The secondary planes meet the primary surface at sharp, well-defined intersections. Image (c) shows region *c* at 917×. A large open cavity dominates the centre of the field of view, bordered by thin elongated ligaments. A population of fine secondary

microvoids is distributed across the surrounding fracture surface. Image (d) shows region *d* at 1,575×. The fracture surface consists of plate-like facets.

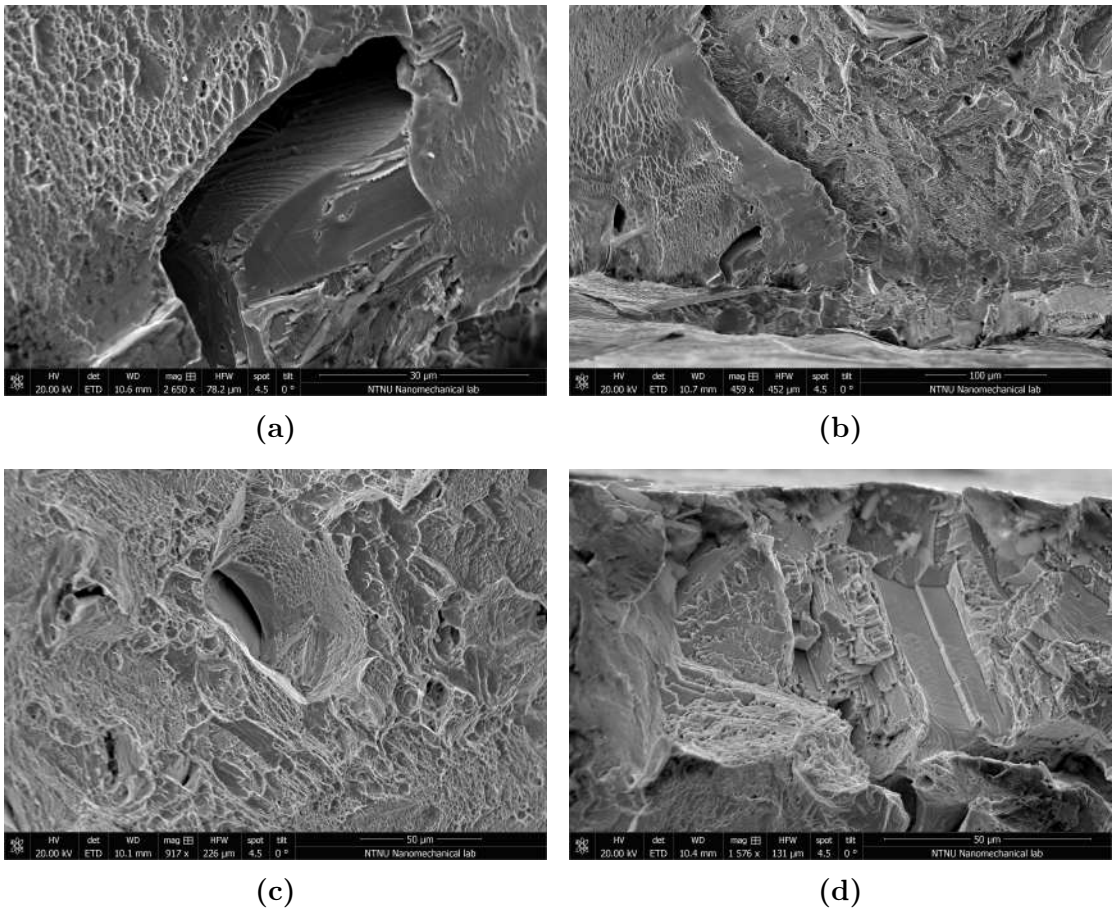

Figure 4.4.7: Magnified SEM views of regions marked in Figure 4.4.6 for the uncoated Ni 725 specimen after 24 h hydrogen charging and tensile testing. (a) High-magnification view of the region labelled "a,b" in Figure 4.4.6 (b) Intermediate magnification showing a dense network of secondary fracture planes. (c) Region containing a large cavity surrounded by plastically deformed ligaments and fine microvoids. (d) Magnified view showing plate-like facets.

4.4.5 Grinded Surface: 72 h Hydrogen Pre-Charged

The fracture surface of the Ni 725 specimen charged for 72 h is shown in Figures 4.4.8–4.4.12. The low-magnification overview in Figure 4.4.8 shows aThe fracture plane is macroscopically flat and oriented nearly perpendicular to the tensile axis. The gauge section retains close to its original rectangular cross-sectional dimensions, with only a minor reduction in thickness at the fracture plane.

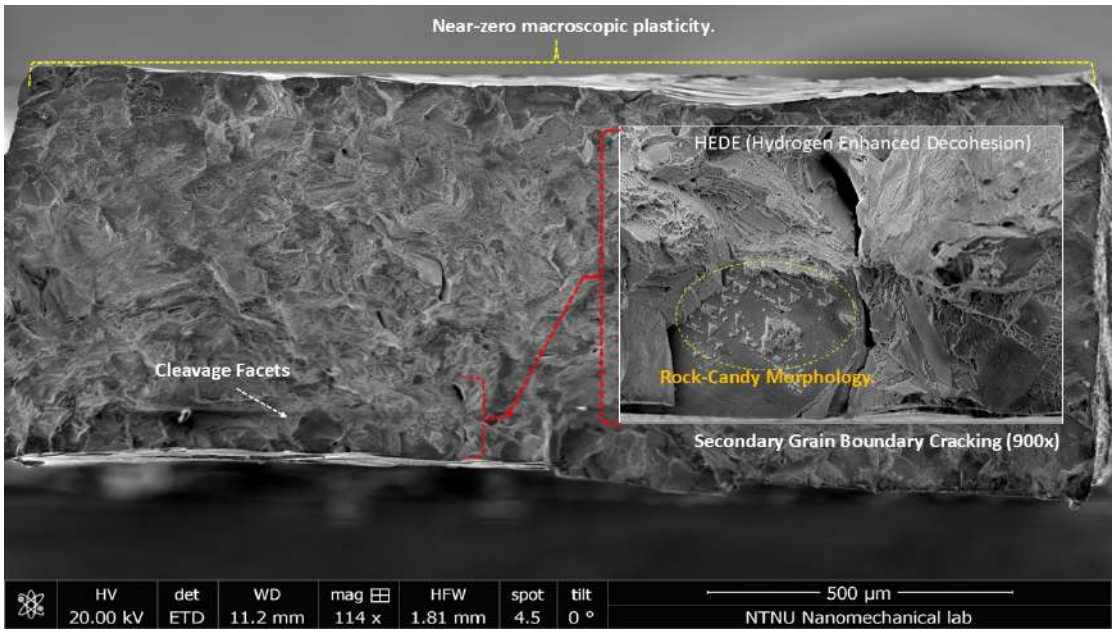

Figure 4.4.8: Overview of the 72 h fracture cross-section showing an essentially un-necked profile and a macroscopically flat, brittle fracture surface.

Figure 4.4.9 presents the central fracture region at 288× magnification. The fracture surface shows two visually distinct zones. The upper portion has an irregular topography with steps. The lower portion consists of comparatively flat, featureless planes. At the boundary between the two zones, short secondary cracks are visible emanating from the step edges.

Figure 4.4.10 shows a higher-magnification view at 768× of an individual fracture facet. A through-thickness crack traverses the centre of the field of view, running along the length of a broad, smooth facet surface. The facet plane is flat and featureless with no visible surface relief or striation markings. On either side of this crack, the surrounding material contains only isolated shallow cavities of small diameter.

Figures 4.4.11 and 4.4.12 document fracture regions at 820× and 968× magnification respectively. In Figure 4.4.11, the fracture surface consists of small, angular, multi-faceted fragments separated from one another by narrow, open gaps.

At higher magnification in Figure 4.4.12, the individual facet surfaces are revealed in detail. The facets are flat and oriented at varying angles to one another, with their boundaries defined by fine secondary cracks running between them.

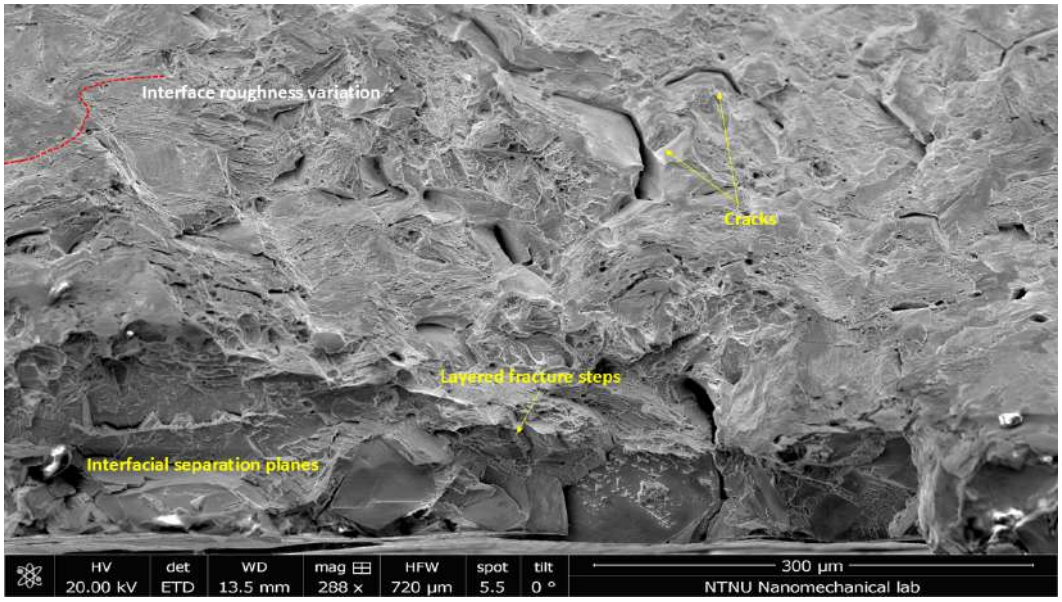

Figure 4.4.9: Central region at 288× magnification, revealing layered fracture steps and interfacial separation planes along weak interfaces.

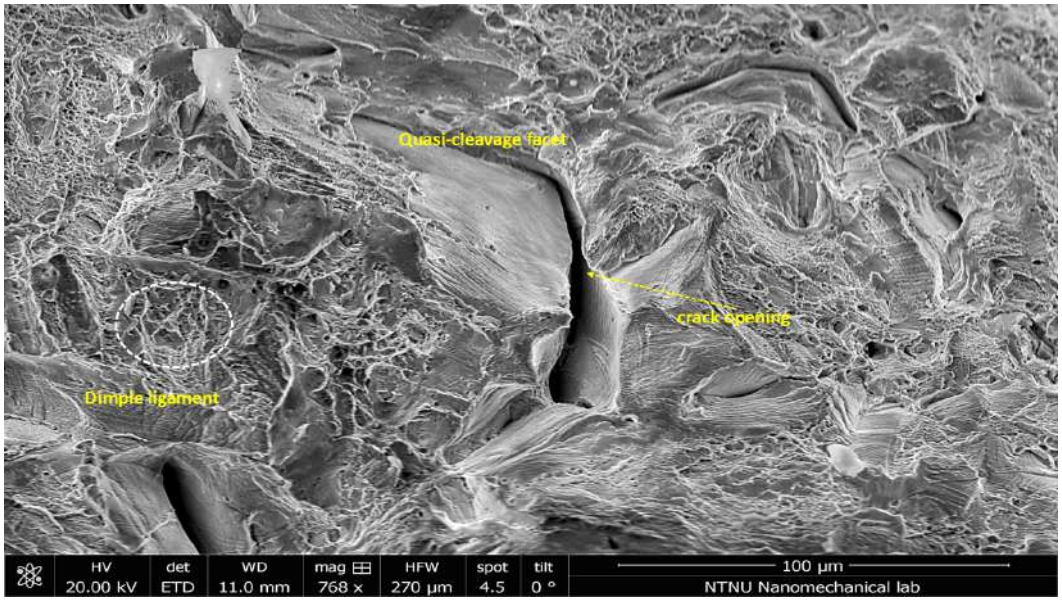

Figure 4.4.10: High-magnification view at 768× of a through-thickness crack propagating along a smooth quasi-cleavage facet with only limited surrounding dimpling.

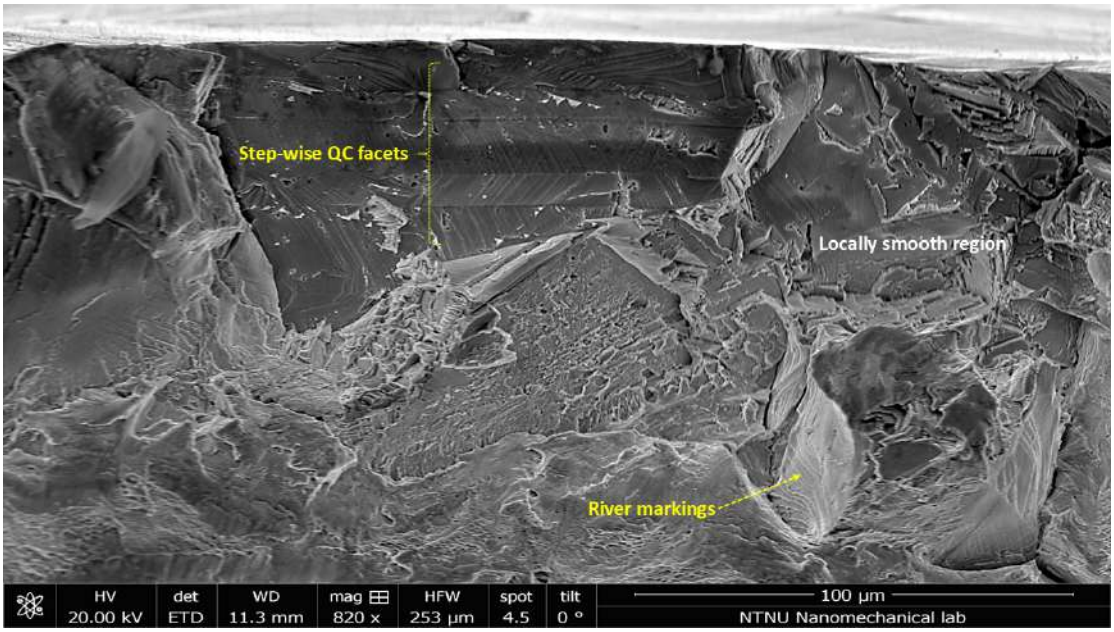

Figure 4.4.11: "Rock-candy" morphology at 820× magnification, formed by hydrogen-assisted grain boundary separation.

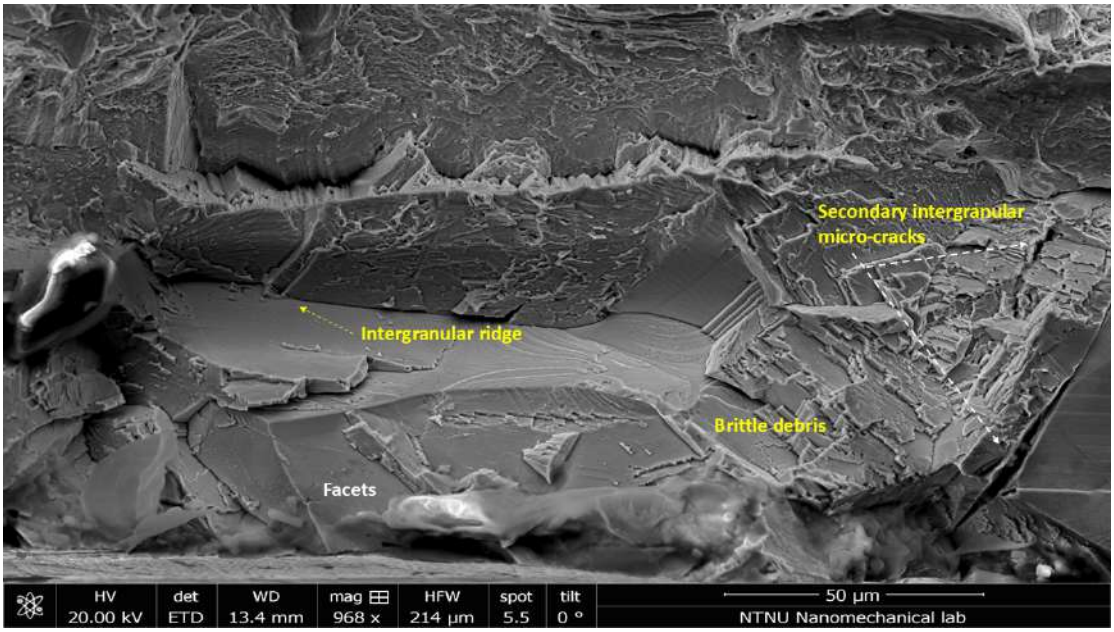

Figure 4.4.12: High magnification (968×) intergranular and quasi-cleavage facets linked by fine secondary cracks and thin ligaments, with only sparse shallow dimples.

4.4.6 Peened surface: air-tested (uncharged)

The fracture surface morphology of the Peened Ni 725 specimen tested in air is shown in Figures 4.4.13 and 4.4.14, covering different magnifications. Figure 4.4.13 shows the fracture surface of the peened Ni725 specimen tested in air. All three regions of the fracture cross-section display a predominantly ductile morphology as seen in Fig: 4.4.14. The left and right quadrants (a, b) show equiaxed dimples of varying size, consistent with microvoid nucleation, growth, and coalescence under tensile loading. The central region (c) similarly exhibits a dimple-dominated fracture surface, with some larger voids interspersed among finer dimples, suggesting void coalescence at multiple length scales. No quasi-cleavage facets or intergranular features are observed, confirming that fracture in the uncharged peened condition proceeds by a fully ductile microvoid coalescence mechanism.

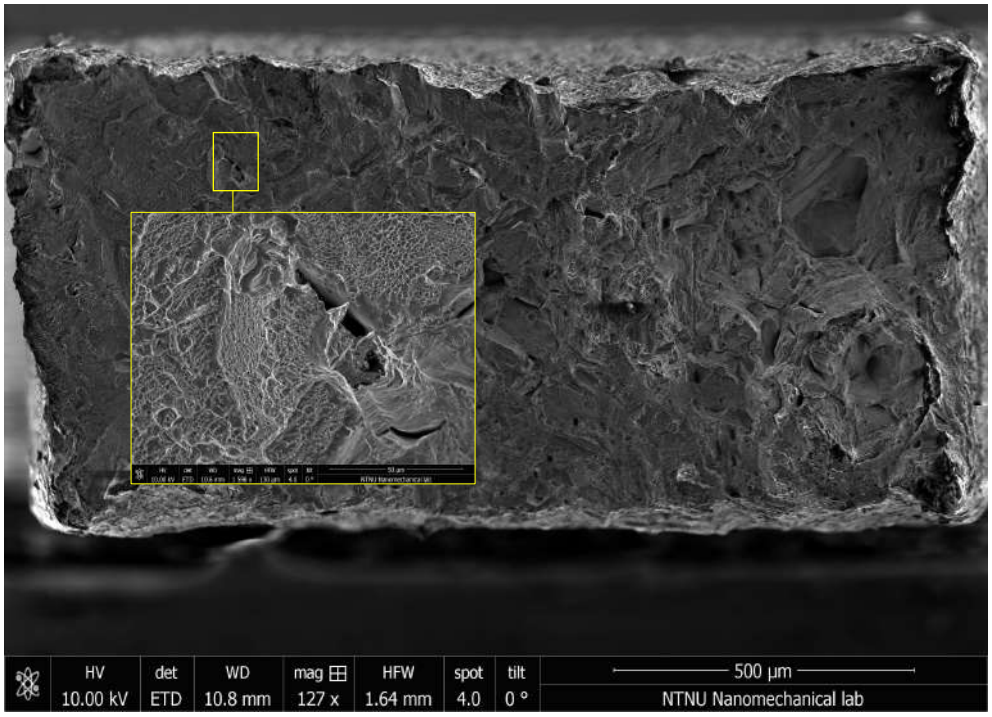

Figure 4.4.13: Overview (127×) of the fracture surface of the peened Ni 725 specimen tested in air.

Figure 4.4.13 shows a low-magnification overview (127×) of the full fracture cross-section. Figure 4.4.14 presents higher-magnification views from three regions of the fracture surface. Image (a) & (b) shows the fracture side quadrants. Image (c) shows the central fracture region at 308×. Open cavities and dimples of varying size are distributed across the surface. The larger cavities have smoothly curved walls, while the smaller ones are more equiaxed and closely spaced.

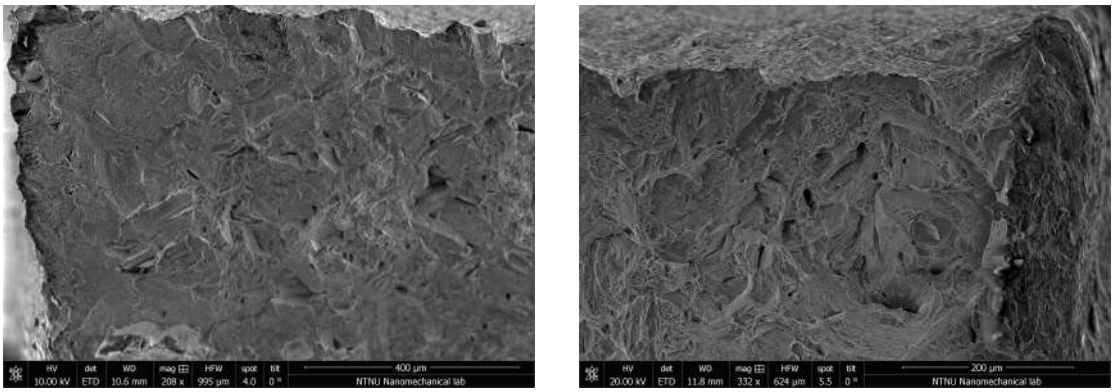

(a) **(b)**

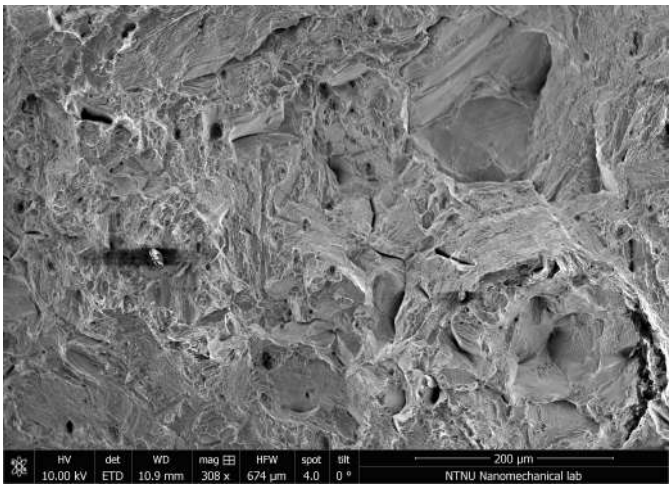

(c)

Figure 4.4.14: Peened Ni 725 specimen tested in air: (a) left fracture quadrant, (b) right fracture quadrant and (c) central region with dimples and voids.

4.4.7 Peened surface: 24 h Hydrogen Pre-charged

The fracture surface morphology of the Peened Ni 725 specimen after 24 h hydrogen pre-charged and tensile testing is shown in Figure 4.4.15, which presents three SEM fields covering the left-top quadrant, the lower-left quadrant with inlay, and the right-side region with near-surface crack inlay.

Figure 4.4.15 (a) shows the left-top fracture quadrant at 292× magnification. The outer edge of the specimen in this quadrant retains the characteristic texture of the peened gauge surface, visible as a finely pitted band along the specimen. Figure 4.4.15 (b) presents the lower-left fracture quadrant as a composite image with an inlay at higher magnification. At the base magnification, the fracture surface exhibits cleavage facets and brittle sone. Figure 4.4.15 (c) presents the right-side fracture quadrant. The inset reveals a near-surface crack region consisting of flat crack walls and step-like fracture features.

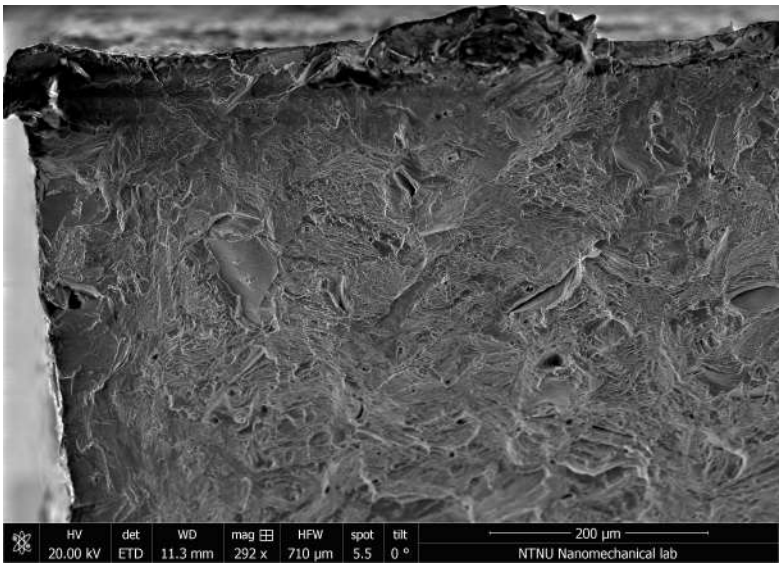

(a)

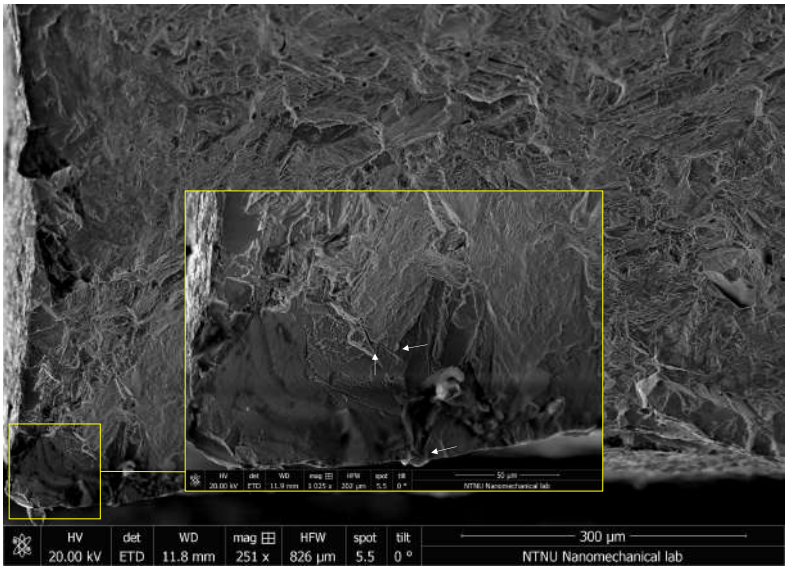

(b)

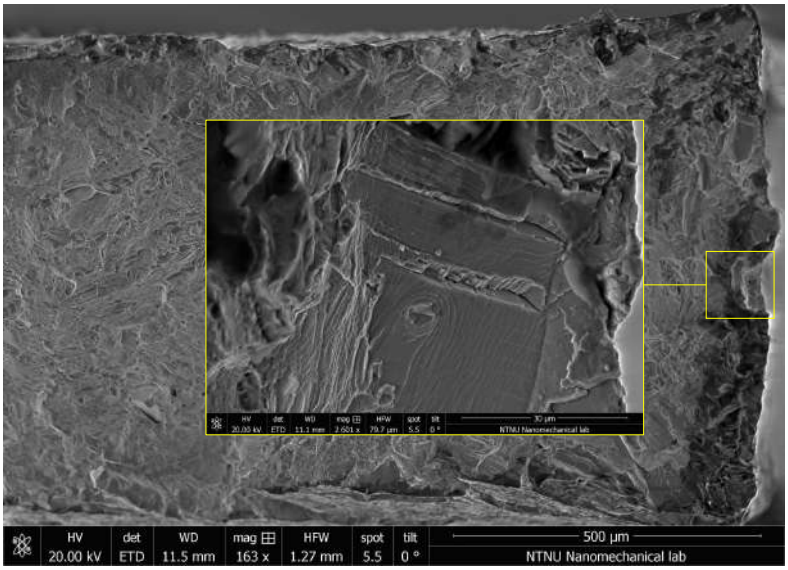

(c)

Figure 4.4.15: Peened Ni 725 specimen after 24 h hydrogen pre-charging: (a) left-top fracture quadrant, (b) quadrant with inlay of a fracture facet (c) quadrant with inlay of a near-surface crack region.

4.4.8 Gold-sputtered surface: 24 h hydrogen pre-charged

The fracture surface of the gold-sputtered Ni 725 specimen after 24 h hydrogen pre-charging and tensile testing is shown in Figures 4.4.16 to 4.4.18. Figure 4.4.16 shows a low-magnification overview (124×) of the fracture surface of the gold-sputtered Ni 725 specimen after 24 h hydrogen pre-charging and tensile testing. An inset in Figure 4.4.16 shows a higher-magnification view of a region near the left specimen corner, revealing a localised crack initiation site with a roughened surface texture and a series of step-like offsets radiating inward from the specimen edge. The brittle layers are seen to be less deep than that of the previous peened surface speciment has reduced greatly which could be seen by comparing Fig: 4.4.15b and that of gold coated Fig: 4.4.17 and also the observations in the near corner inlay of Fig: 4.4.16 shows the microvoid coalescent features even near corners, whereas equivalent regions of peened sample Fig: 4.4.15b is already deeply embrittled.

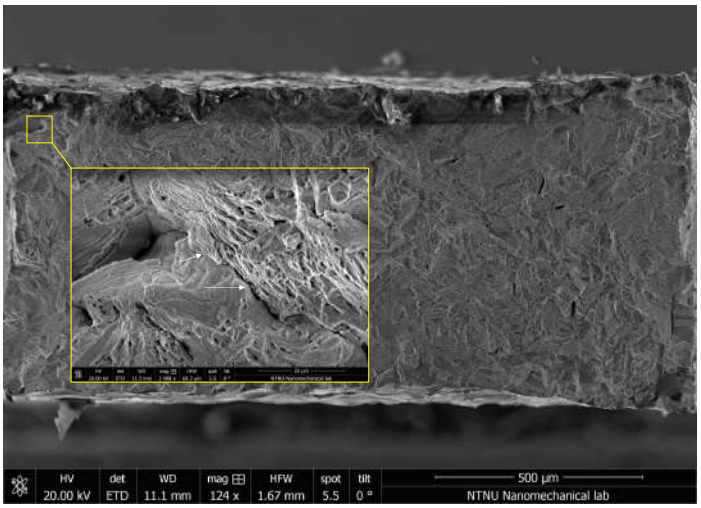

Figure 4.4.16: Overview of the fracture surface of the gold-sputtered Ni 725 specimen after 24 h hydrogen pre-charging.

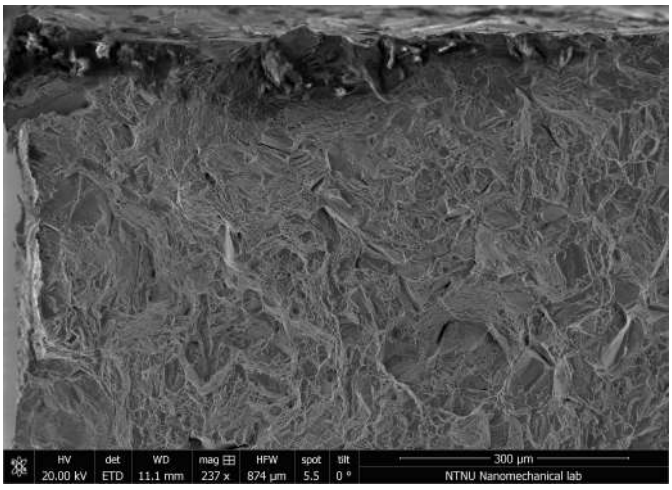

Figure 4.4.17: Fracture cross-section of the gold-sputtered Ni 725 specimen after 24 h hydrogen pre-charging with inset of a near-edge region.

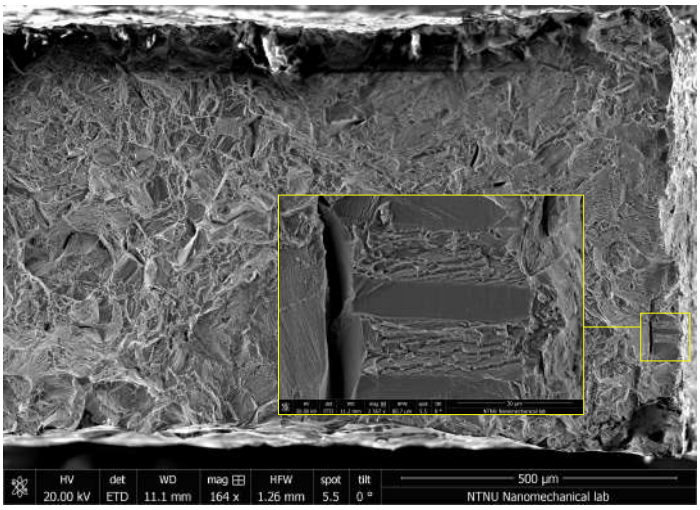

Figure 4.4.18: Higher-magnification view of the gold-sputtered Ni 725 specimen after 24 h hydrogen pre-charging near the fracture edge.

4.4.9 Ni-Plated Specimen surface: 24 h Hydrogen Pre-Charged

The fracture morphology of the electrodeposited Ni-coated Ni 725 specimen after 24 h hydrogen pre-charging is shown in Figures 4.4.19 and 4.4.20. Figure 4.4.19 presents a low-magnification overview (109×) of the full fracture cross-section. The fracture surface is macroscopically flat across most of the gauge width. The overall topography is dominated by large, angular QC facets.

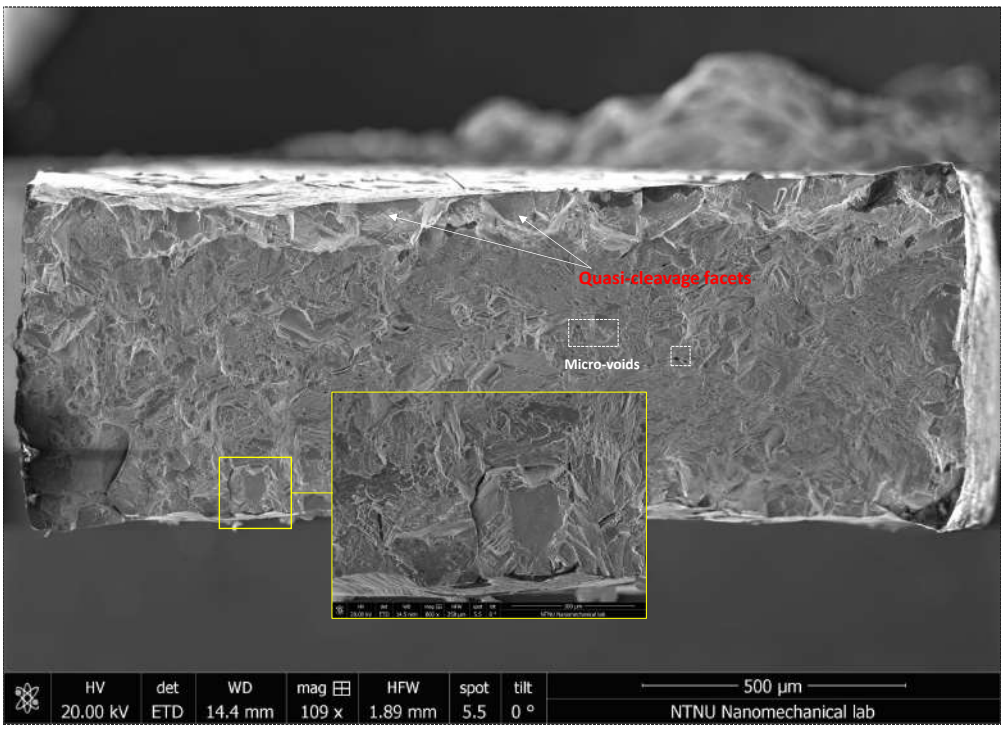

Figure 4.4.19: Overview SEM image (109×) of the fracture cross-section of the electrodeposited Ni-coated Ni 725 specimen after 24 h hydrogen pre-charging, showing a macroscopically flat, faceted fracture surface with limited necking.

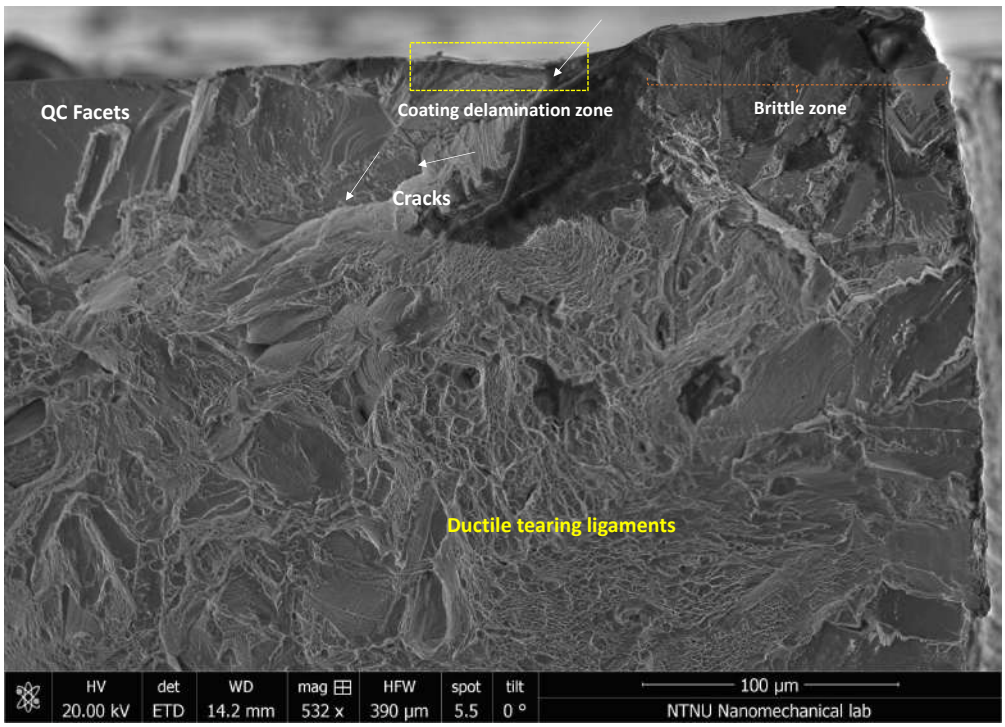

Figure 4.4.20: High-magnification SEM image (532×) of the Ni-plated specimen after 24 h hydrogen pre-charging, showing large quasi-cleavage facets with river-like markings and intervening tearing ridges, underlain locally by finer, fibrous regions with limited ductile tearing.

4.5 EDS Analysis

EDS elemental maps were acquired on FIB-prepared cross-sections from two specimens after 24 h hydrogen pre-charging: the EDM-finished & the shot-peened Ni 725 specimen. These two conditions were specifically selected for EDS analysis because they represent the two surface states in this study for which the near-surface chemical composition is substantially altered by the surface treatment itself, independent of hydrogen charging. Figure 4.5.1 shows EDS maps from a cross-section through the EDM-affected surface region. The mapped area includes the outer surface band, the underlying recast layer, and the bulk substrate. In the oxygen map, a continuous O-enriched band is visible at the outermost surface, with O intensity decreasing towards the interior. The tungsten map shows W signal confined to the same surface band. Chromium intensity is lower in this surface band than in the underlying substrate. Ni, Mo and Nb show uniform distributions below the surface band. The copper map shows a localised Cu-rich patch at the surface, with no Cu signal in the bulk region. Figure 4.5.2 shows EDS maps from a cross-section near the peened surface. The peened surface appears at the top of the mapped area, with cavities in the near-surface region. A single compositionally distinct region is visible at the cavity site. The Ti map shows a Ti-enriched region where Ni intensity is reduced at the same site and uniform in the surrounding matrix. The Cr and Mo maps show uniform distributions across the matrix with no strong local enrichment except a common reduced signal in the cavity.

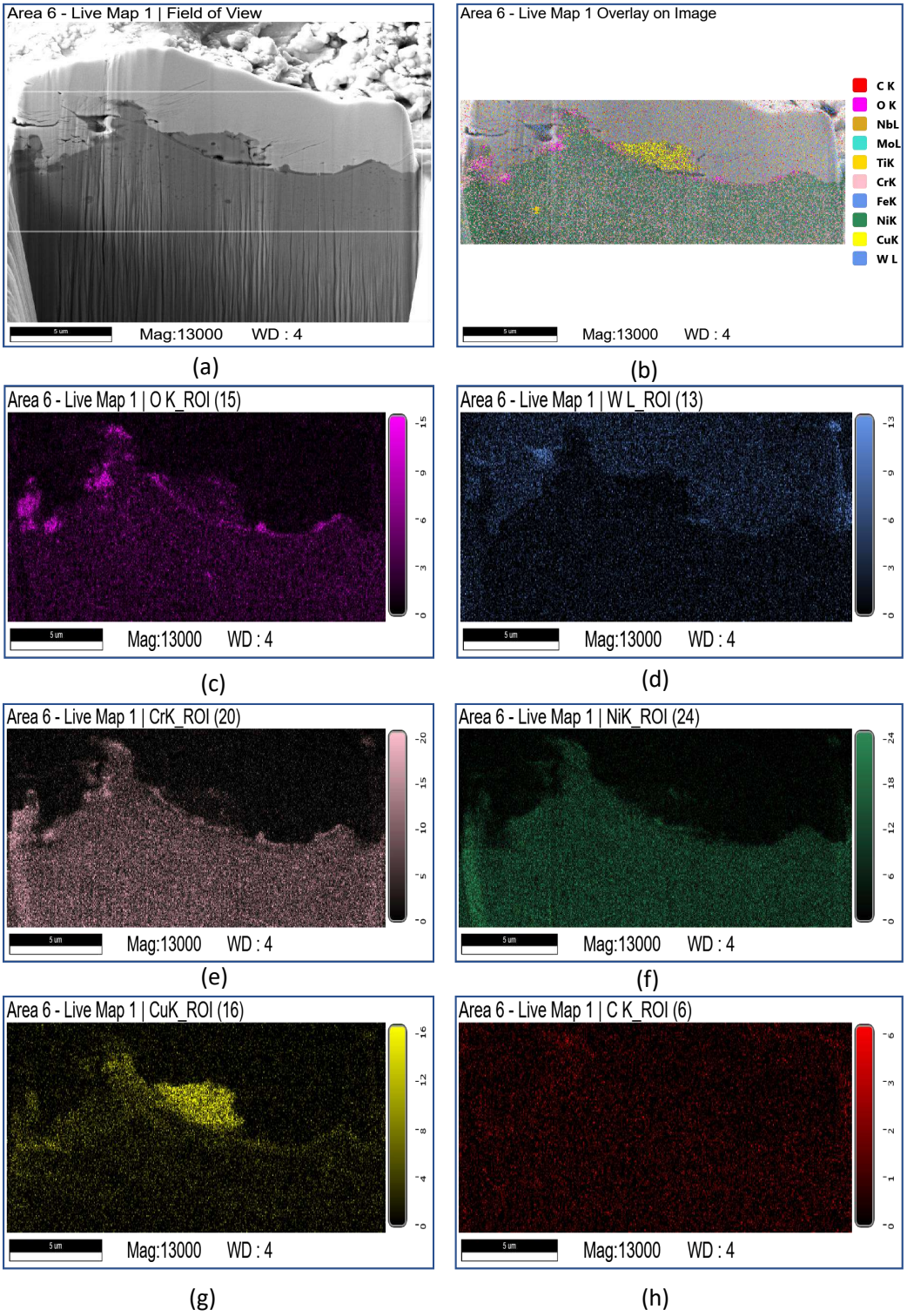

Figure 4.5.1: EDS elemental maps of the FIB cross-section through the EDM recast layer, Ni 725 after 24 h hydrogen pre-charging.

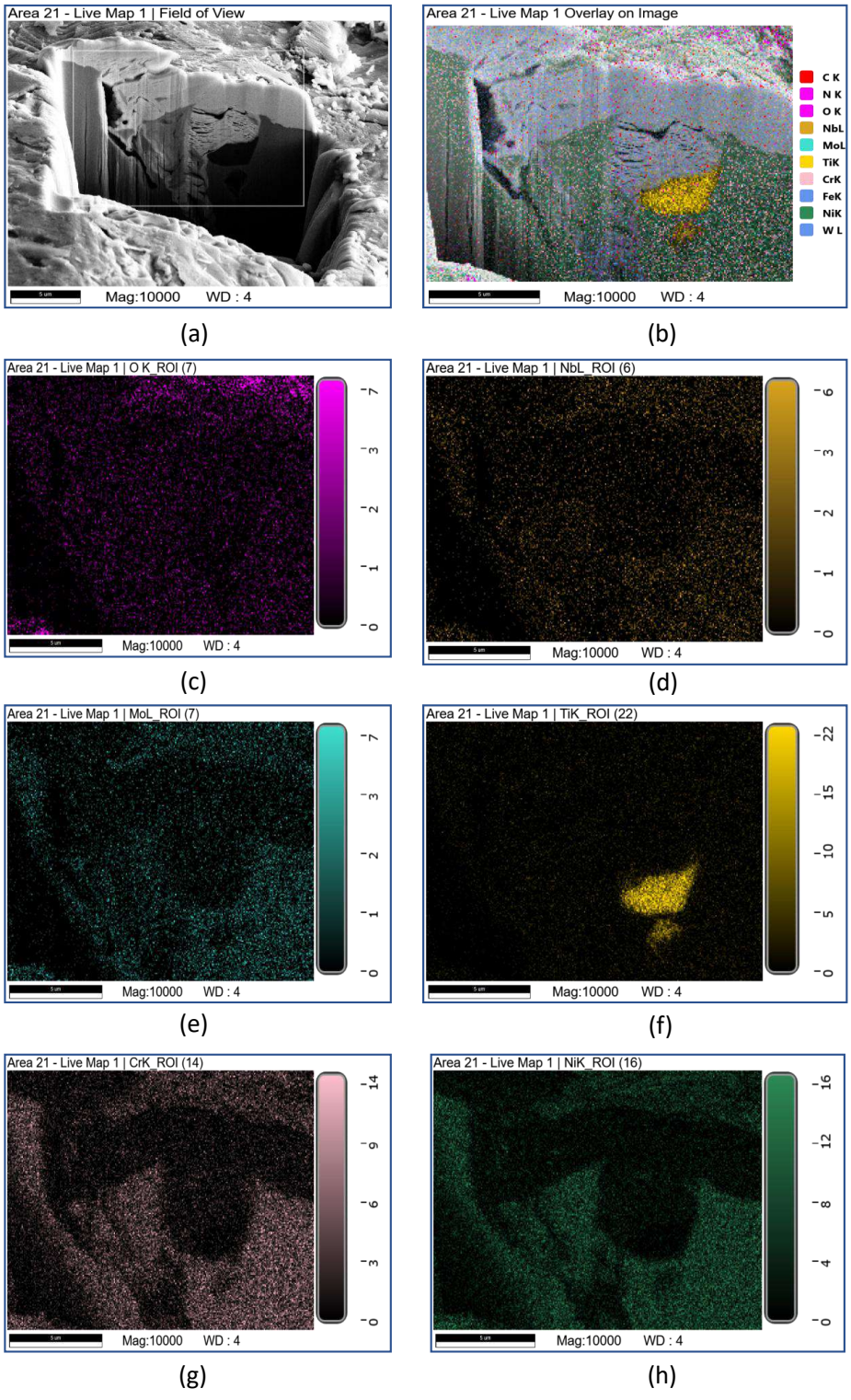

Figure 4.5.2: EDS elemental maps of the FIB-prepared cross-section of the shot-peened Ni 725 specimen after 24 h hydrogen pre-charging (Area 21, 10 000×).

4.6 Brittle Zone Depth Across Surface Conditions

To quantify the extent of hydrogen-assisted damage in each specimen, the depth of the brittle zone was measured from the outer specimen surface to the transition boundary between the quasi-cleavage/flat facet region and the ductile dimple-dominated interior. Ten measurements per specimen were taken from the low-medium magnification fracture images using ImageJ, with the scale calibrated against the SEM data bar for each image. The mean brittle zone depths and associated standard deviations are reported in Table 4.6.1 and plotted in Figure 4.6.1.

Table 4.6.1: Mean brittle zone depth of Ni 725 under different surface conditions.

Surface condition	**Mean depth** (µm)	**SD** (µm)
Ground 2000-grit	70.8	29.2
EDM	88.8	49.2
Peened	70.4	40.5
Gold-sputtered	74.4	26.8
Ni-plated	81.6	22.1

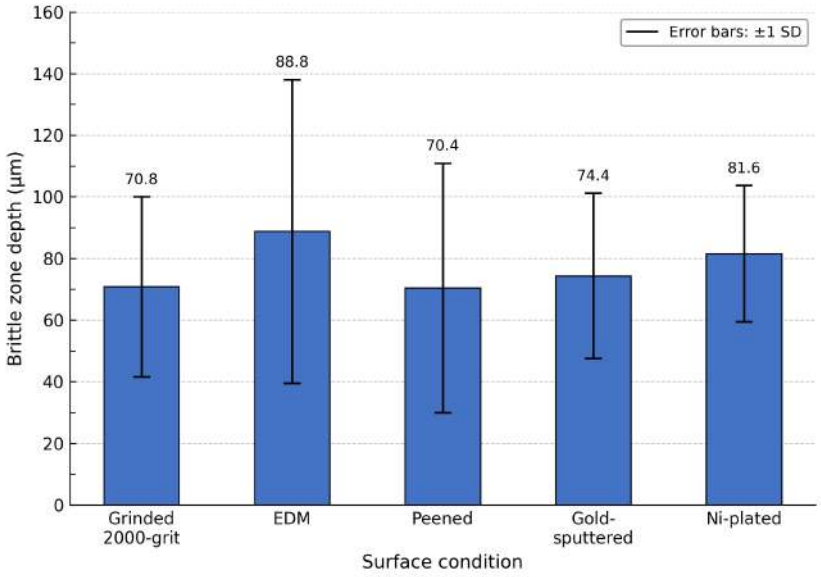

Figure 4.6.1: Mean brittle zone depth for Ni 725 specimens under different surface conditions.

The EDM specimen shows the highest mean brittle zone depth of 88.8 µm and the largest standard deviation (±49.2 µm) of all conditions tested. The Ni-plated specimen shows a mean depth of 81.6 µm and the lowest standard deviation (±22.1 µm). The gold-sputtered specimen shows a mean depth of 74.4 µm with a standard deviation of ±26.8 µm. The ground and peened specimens show similar mean depths of 70.8 and 70.4 µm respectively, with standard deviations of ±29.2 and ±40.5 µm. Across all conditions, the mean brittle zone depth ranges from 70 to 89 µm, and the standard deviation ranges from 22 to 49 µm.

4.7 Hydrogen Content

Table 4.7.1 lists the hydrogen content measured by thermal desorption spectroscopy (TDS) for the four surface conditions after 24 h electrochemical hydrogen pre-charging & mechanical testing.

Table 4.7.1: Hydrogen content of Ni 725 for different surface condition.

Specimen	**Hydrogen content (wppm)**
Ground (2000-grit)	27.54
Peened	27.78
EDM-finished	28.02
Ni-plated	56.83

The ground, peened, and EDM-finished specimens show similar hydrogen contents in the range of 27.5 to 28.1 wppm. The Ni-plated specimen shows a notably higher hydrogen content of 56.83 wppm, approximately twice the values measured for the other three conditions.

CHAPTER

FIVE

DISCUSSION

5.1 Mechanical properties

This section integrates the tensile results, fracture morphologies, brittle zone measurements, TDS hydrogen content and EDS analyses to discuss how surface condition and hydrogen charging duration influence hydrogen embrittlement susceptibility in Ni 725. The discussion is organised around: (i) the effect of charging duration on the ductile-to-brittle transition, (ii) the role of surface condition in controlling hydrogen uptake and embrittlement severity, and (iii) the mechanistic context for the observed fracture modes.

Table 5.1.1: Summary of mechanical and fractographic results for all surface conditions and charging states. ε_f = fracture strain; UTS = ultimate tensile strength; I_{HE} = hydrogen embrittlement index (Eq. 4.2); BZ depth = brittle zone depth (mean ± SD); H content from TDS after 24 h charging. *Ground 2000-grit air value used as reference for I_{HE}.

Surface	**Condition**	$\boldsymbol{\varepsilon_f}$ (%)	**UTS** (MPa)	$\boldsymbol{I_{\mathrm{HE}}}$ (%)	**BZ depth** (µm)	**H cont.** (wppm)
Ground	Air	35.99	1177.2	–	–	–
Ground	24 h H	16.01	1245.2	55.5	70.8 ± 29.2	27.54
EDM	Air	35.33	1157.6	–	–	–
EDM	24 h H	21.30	1086.4	39.7	88.8 ± 49.2	28.02
Shot-peened	Air	27.99	1181.4	–	–	–
Shot-peened	24 h H	15.92	1097.5	43.1	70.4 ± 40.5	27.78
Gold-sputtered	24 h H	20.98	1162.8	41.7*	74.4 ± 26.8	–
Ni-plated	24 h H	10.73	1082.8	70.2*	81.6 ± 22.1	56.83

5.1.1 Effect of Hydrogen Charging Duration and Surface Condition on Tensile Response

The ground 2000-grit condition provides the clearest baseline for interpreting hydrogen-induced degradation, as the surface state is well-defined, thermally unmodified, and free of foreign deposits. In air, the specimen exhibits high ductility ($\varepsilon_f \approx 36\%$) with a classic ductile tensile response, pronounced necking, extensive slip traces and surface rumpling, and a dimpled fracture surface dominated by equiaxed microvoid coalescence (Figures 4.3.3, 4.3.4, 4.4.5). After 24 h charging ($\varepsilon_f = 16.01\%$), a zone of secondary surface cracks develops on the gauge face near the primary fracture, oriented predominantly perpendicular to the loading axis and associated with dense planar slip bands (Figures 4.3.5, 4.3.6). The fracture surface already shows extensive quasi-cleavage facets, large open voids, necked ligaments, serrated crack walls, and facet-like planes with sharp angular steps (Figures 4.4.6, 4.4.7, 4.4.7c, 4.4.7a, 4.4.7b, 4.4.7d). The UTS at 24 h (1245.2 MPa) is slightly elevated compared to the air reference (1177.2 MPa), consistent with hydrogen-enhanced dislocation pinning and solute strengthening in a HELP-type response at early embrittlement stages [101]. After 72 h charging, the degradation is severe ($\varepsilon_f = 9.35\%$, UTS = 1098.0 MPa). The specimen fails with an almost un-necked, macroscopically flat fracture, and the secondary crack density and extent increase markedly (Figures 4.3.7, 4.3.8, 4.4.8). Crack tips are sharp and unblunted with minimal surrounding plasticity [101]. The fracture surface is almost entirely composed of flat facets, step-like interfacial levels, and angular fragment morphology consistent with the "rock-candy" appearance reported for severely embrittled Ni alloys [102, 103]. Smooth flat facet surfaces and the absence of striation markings (Figure 4.4.10) indicate crack advance by hydrogen-enhanced decohesion (HEDE) along grain boundaries or low-index crystallographic planes [104, 105]. The drop in UTS at 72 h indicates that fracture intervenes before the material reaches its full flow stress capacity. This progression is consistent with published in-situ observations on Ni 725, where hydrogen promotes early crack initiation along slip bands and grain boundaries, with a gradual transition to mixed ductile–brittle behaviour with more intergranular and quasi-cleavage fracture at high hydrogen concentrations [106, 107, 108, 103]. The 24 h exposure corresponds to an intermediate embrittlement regime where ductile and brittle mechanisms coexist, while the 72 h exposure drives the material into a severely embrittled state. In air, the peened specimen shows just few secondary cracks on the gauge surface beyond the immediate fracture zone (Figure 4.3.9), reflecting ductile behaviour despite the presence of a cold-worked, compressively stressed near-surface layer. After 24 h charging, a clear network of secondary cracks appears on the gauge face near the fracture, oriented roughly normal to the loading axis (Figure 4.3.10). The associated fracture surfaces contain mixed faceted and torn regions (Figure 4.4.15), indicating that hydrogen has reduced the protective effect of the compressive residual stress field and facilitated crack initiation at localised stress concentrators such as shot-induced surface indentations and second-phase particles [109]. In the gold-sputtered condition, the coated gauge surface remains visually discontinuous and limited delamination after 24 h charging (Figure 4.3.12). Secondary cracks still form near the fracture, however, with sharp, unblunted faces and minimal plasticity (Figure 4.3.13b). The crack

paths and facet morphologies are consistent with hydrogen-assisted decohesion at the gold–substrate interface or within the underlying substrate grains, confirming a limited hydrogen ingress through the thin, imperfect Au barrier [110]. The Ni-plated specimen exhibits the most severe surface damage among all conditions: distributed oblique secondary cracks and wedge-shaped crack openings with striated walls (Figures 4.3.14, 4.3.15), discussed in detail in Section 5.1.4.

5.1.2 Effect of hydrogen charging duration on tensile response

The grinded 2000-grit condition provides the clearest picture of how increasing hydrogen content modifies the mechanical response of Ni 725, because the surface state is well-defined, thermally unmodified and free of foreign deposits. The evolution from the air-tested reference to 24 h and 72 h hydrogen-charged conditions captures a systematic transition from fully ductile to predominantly brittle behaviour. In air, the ground specimen exhibits high ductility ($\varepsilon_f \approx 36\%$) and a classic ductile tensile response with pronounced necking and a dimpled fracture surface dominated by equiaxed microvoid coalescence (Figure 4.4.5). The 72 h specimen, by contrast, fails at only 9.35% elongation with an almost un-necked, macroscopically flat fracture along the sides and corners of the fracture surface (Figure 4.4.8). The 24 h condition lies between these two extremes, with an intermediate elongation of 16.01% and a fracture surface that already shows extensive quasi-cleavage facets and secondary cracking (Figures 4.4.6 and 4.4.7). This progression is consistent with published observations on Ni 725 and related Ni-base alloys, where increasing hydrogen concentration drives a transition from ductile behaviour to predominantly ductile–brittle fracture [108, 103]. The UTS at 24 h (1245.2 MPa) is slightly elevated compared to the air reference (1177.2 MPa). A moderate increase in flow stress at intermediate hydrogen contents has been attributed to hydrogen-enhanced dislocation pinning and solute strengthening effects in Ni-base alloys, consistent with a HELP-type response at early embrittlement stages [101]. At 72 h, the UTS drops to 1098.0 MPa, indicating that fracture intervenes before the material reaches its full flow stress capacity. The fractographic evolution reinforces this interpretation. In the 24 h condition, the fracture surface contains mixed features: large open voids and necked ligaments in some regions (Figure 4.4.7c), but also serrated crack walls and facet-like planes with sharp angular steps (Figures 4.4.7a, 4.4.7b and 4.4.7d). By 72 h, the fracture surface is almost entirely composed of flat facets, step-like interfacial levels and angular fragment morphology, sometimes described as “rock-candy” fracture in severely embrittled Ni alloys [102, 103]. The smooth flat facet surfaces with through-thickness cracks (Figure 4.4.10) and the absence of striation markings are consistent with crack advance by hydrogen-enhanced decohesion (HEDE) along grain boundaries or low-index crystallographic planes [104, 105]. These observations are consistent with recent in-situ studies on Ni 725, which report that hydrogen promotes early crack initiation along planar slip bands and grain boundaries, with a gradual transition from mixed ductile–brittle behaviour at intermediate hydrogen levels to predominantly intergranular and quasi-cleavage fracture at high hydrogen concentrations [106, 107]. The present results show that, under the applied charging conditions, the 24 h exposure corresponds to an intermediate embrittlement regime where duc-

tile and brittle mechanisms coexist, whereas the 72 h exposure drives the material into a severely embrittled state.

5.1.3 Influence of surface condition on HE index

The I_{HE} provides a useful scalar measure of the loss in ductility due to hydrogen for conditions where an air reference is available. For 24 h charging, the ground specimen shows the highest index (55.5%), followed by the shot-peened (43.1%) and EDM (39.7%) specimens (Table 4.2.2). The gold-sputtered and Ni-plated values use the ground air reference strain, as no separate air baseline was obtained for these conditions. At first glance, it is counterintuitive that the smoothest and chemically cleanest surface exhibits the largest *relative* ductility loss. However, this can be rationalised by considering both the denominator in Eq. 4.2 and the surface-condition dependence of the air baseline ductility. The ground 2000-grit specimen has the highest air fracture strain (35.99%), whereas the peened specimen already exhibits reduced air ductility (27.99%) due to peening-induced work hardening in the near-surface layer, and the EDM specimen has a slightly lower air elongation (35.33%) associated with its recast-layer heterogeneity (Table 4.2.1). Because I_{HE} is normalised by the air fracture strain, a larger baseline ductility amplifies the apparent loss when hydrogen reduces ε_f to a similar absolute level. Thus, the high I_{HE} for the ground specimen partly reflects its very ductile air reference rather than an intrinsically higher susceptibility to hydrogen. When compared on the basis of absolute post-charging fracture strain, the EDM specimen retains the most elongation (21.30%) and the Ni-plated specimen the least (10.73%), which better reflects their actual embrittlement severity. The TDS data (Table 4.7.1) show that the ground, peened and EDM specimens all absorbed similar hydrogen contents (27.5–28.1 wppm) after 24 h charging, despite their different surface conditions. This indicates that for these three conditions the difference in I_{HE} is governed more by how hydrogen is distributed and localised at microstructural features than by a difference in total absorbed hydrogen. The Ni-plated specimen absorption is the highest at 56.83 wppm, approximately twice the other three conditions, which directly explains its most severe embrittlement. The role of the Ni coating in amplifying hydrogen uptake is discussed further in Section 5.1.4. Nonetheless, the absolute fracture strains after 24 h charging still differ across surface conditions in a non-trivial way. The EDM specimen retains 21.30% elongation, the peened specimen 15.92%, and the ground specimen 16.01%. The gold-sputtered and Ni-plated conditions, which only exist in the hydrogen-charged state, show 20.98% and 10.73% elongation respectively. Taken together, these values point that Surface treatments that introduce strong near-surface heterogeneity or residual stress (EDM recast layer, Peened surface) modify not only the air ductility but also the way hydrogen localises and triggers fracture. The gold-sputtered surface, despite gold's low intrinsic hydrogen solubility, does not prevent hydrogen ingress into the Ni 725 substrate at 24 h, but the resulting fracture strain (20.98%) is intermediate rather than the most severe, reflecting the thin, relatively uniform coating and its limited capacity to trap hydrogen [110, 111].

5.1.4 Electrodeposited Ni Coating and its Role in Hydrogen-Assisted Failure

The Ni-plated specimen consistently exhibits the most severe embrittlement among all 24 h-charged conditions: the lowest fracture strain, the second-deepest brittle zone (81.6 µm, Table 4.6.1) with the lowest standard deviation (±22.1 µm), and a fracture cross-section dominated by large quasi-cleavage facets with river-line markings (Figure 4.4.20). This outcome is counterintuitive if the coating is assumed to act simply as a hydrogen diffusion barrier. The following analysis argues that the electrodeposited Ni layer is better understood as reasons Ni coating may have acted as a catalyst for H uptake,

Hydrogen introduced during electrodeposition:

Electroplating from a Watts-bath electrolyte proceeds by competing cathodic reactions. Alongside nickel deposition ($Ni^{2+} + 2e^- \rightarrow Ni$), proton reduction ($2H^+ + 2e^- \rightarrow H_2$) generates atomic hydrogen at the deposit surface throughout the plating process. A fraction of this nascent hydrogen absorbs into the growing Ni layer and can further diffuse into the underlying alloy substrate before either recombining at the deposit surface or becoming trapped at lattice defects within the coating [112, 113]. The columnal deposition of the Watts-bath deposit observed in plan-view SEM (Figure 4.1.6) and the scattered surface nodules are microstructural features associated might have provided additional irreversible trapping sites for hydrogen within the deposit [114]. As a result, the Ni 725 specimen may already carry a non-trivial subsurface hydrogen concentration before the start of the electrochemical pre-charging experiment, placing it at a higher baseline hydrogen content than the uncoated specimens that begin charging from a fully annealed, hydrogen-free state.

Low hydrogen diffusivity and retention in Ni

Pure electrodeposited Ni has a substantially higher hydrogen diffusivity than the Ni-Fe-Cr-Mo matrix of Ni 725. This asymmetry means that during cathodic precharging, hydrogen that enters the system from the electrolyte side diffuses readily through the Ni coating and into the substrate, which is also evident from a high hydrogen content. The exceptionally low standard deviation of the brittle zone depth (±22.1 µm, compared with up to ±49.2 µm for the EDM condition) is consistent with a spatially uniform hydrogen flux across the full gauge surface.

Coating defects as preferential hydrogen pathways

Real electrodeposited coatings contain pores, pinholes and intergranular microcracks, particularly at the coating–substrate interface [113]. The large-scale delamination and tearing at the right-hand specimen edge visible in the low-magnification surface overview (Figure 4.3.14) confirms that the coating–substrate interface failed locally during tensile loading. Interface defects of this type provide diffusion paths, creating zones of locally elevated hydrogen concentration at the interface. The secondary surface cracks observed across the gauge face (Figure 4.3.14) are

consistent with initiation at such interface or coating-interior defect sites under the combined action of hydrogen-enhanced decohesion and the tensile stress field.

Taken together, these factors explain why the electrodeposited Ni coating under the conditions of this study functions as a hydrogen reservoir rather than a protective barrier. This has direct implications for the use of Ni electroplating as a surface protection strategy in hydrogen-containing environments: without a careful control of plating parameters to minimise hydrogen co-deposition, Ni coatings may worsen rather than mitigate hydrogen embrittlement susceptibility [112, 113].

5.1.5 Role of surface microstructure and chemistry: EDM and peened EDS

For the EDM 24 h specimen, the recast layer carries a continuous O-rich surface band, co-located W and Cu contamination from the brass wire electrode, and Cr depletion relative to the substrate (Figure 4.5.1). Oxide-covered surfaces are known to lower the activation barrier for hydrogen absorption by providing a higher density of active dissociation sites [115]. Cr depletion reduces local passivation capacity, increasing the electrochemical activity of the surface during cathodic charging. Together, these features are consistent with the deep and highly variable brittle zone observed for the EDM specimen (Section 4.6) and the edge-initiated, faceted fracture after 24 h charging (Figures 4.4.3, 4.4.4). For the peened 24 h specimen, EDS cross-sections reveal a localised Nb–Ti-rich particle at a near-surface cavity (Figure 4.5.2). Nb–Ti-rich carbides and δ-phase precipitates are known irreversible hydrogen trap sites in precipitation-hardened Ni alloys, providing sites for hydrogen accumulation and stress concentration at the particle–matrix interface [116, 117]. The absence of a surface oxide band or O enrichment at the peened surface distinguishes it clearly from the EDM condition. These contrasting EDS signatures highlight that EDM and peening promote hydrogen embrittlement through different microstructural routes. EDM creates a chemically and mechanically vulnerable recast layer that enhances hydrogen entry over a broad area, whereas peening creates discrete, local trapping and crack initiation sites within an otherwise chemically unmodified surface.

5.1.6 Brittle zone depth and hydrogen penetration behaviour

The brittle zone depth measurements provide a quantitative link between surface condition and the penetration depth of hydrogen-assisted damage. Despite the different surface treatments, the mean brittle zone depth falls within a relatively narrow range (70–88 µm) for all 24 h-charged specimens (Table 4.6.1 and Figure 4.6.1), suggesting that the overall diffusion-controlled hydrogen penetration depth after 24 h is broadly similar across conditions. The key difference lies in the variability of this depth, as captured by the standard deviations.

The EDM specimen shows the deepest and most variable brittle zone (88.8 ± 49.2 µm), consistent with a spatially irregular recast layer morphology, non-uniform crack density and local variations in oxide and contamination thickness. These

heterogeneities produce locally enhanced and suppressed hydrogen entry, resulting in a highly non-uniform brittle–ductile transition boundary.

The Ni-plated specimen shows a relatively deep but very uniform brittle zone (81.6 ± 22.1 µm), corroborating the picture that a dense, continuous Ni coating acts as a uniform hydrogen source during charging. Hydrogen absorbed in the coating during pre-charging can diffuse into the substrate during loading, and because the coating is chemically homogeneous and fully covering, the hydrogen flux into the substrate is spatially uniform. This leads to a well-defined, reproducible brittle zone depth across the gauge cross-section, as reflected in the low standard deviation.

The ground, shot-peened and gold-sputtered specimens show intermediate mean depths (70.4–74.4 µm) with moderate scatter. The shot-peened specimen shows the highest scatter among these three (±40.5 µm) despite a mean depth nearly identical to the ground specimen (±29.2 µm), reflecting the heterogeneous dislocation structure and local second-phase particle exposure introduced by peening [109, 117].

Overall, the 24 h charging protocol produces a quasi-cleavage brittle zone of order 70–90 µm in Ni 725 regardless of surface condition, but the uniformity and reproducibility of this brittle zone are strongly governed by the surface microstructure and chemistry.

5.1.7 Mechanistic interpretation & implications for surface engineering

Combining the tensile data, fracture morphologies, surface damage observations, brittle zone depths and EDS analyses, a coherent mechanistic picture of hydrogen embrittlement in Ni 725 emerges.

First, hydrogen promotes crack initiation along regions of localised plasticity (slip bands) and at microstructural or chemical discontinuities (second-phase particles, recast layer cracks, coating–substrate interfaces). This is consistent with in-situ studies on Ni 725 that identify planar slip localisation and grain boundary segregation as central to hydrogen-assisted crack initiation [108, 118, 103]. Secondly, hydrogen shifts the fracture mode from dimpled microvoid coalescence toward quasi-cleavage and intergranular decohesion as hydrogen concentration increases. This transition is most clearly demonstrated in the ground specimen series (air $\rightarrow$ 24 h $\rightarrow$ 72 h) but is evident across all surface conditions at 24 h. Mixed quasi-cleavage and intergranular morphologies are widely reported in Ni-base alloys under hydrogen charging, and are attributed to a combination of hydrogen-enhanced decohesion (HEDE) along grain boundaries and carbide interfaces and hydrogen-enhanced localised plasticity (HELP) concentrating strain ahead of the crack tip [104, 101, 105]. Third, the surface condition modulates embrittlement primarily through its effect on near-surface hydrogen entry and trapping, not by changing the underlying mechanisms. EDM introduces a chemically active, Cr-depleted recast layer that accelerates hydrogen entry over a broad area [115]. Peening introduces a cold-worked dislocation-rich layer and exposes second-phase

particles at the surface, creating localised hydrogen trapping and crack initiation sites without modifying the global surface chemistry [109, 117]. The gold-sputtered film offers only partial protection at the thickness used here [110, 111]. The Ni coating functions as a hydrogen reservoir and introduces interface defects, leading to the most severe embrittlement [112, 113].

From an engineering perspective, these findings suggest that for Ni 725 under cathodic conditions:

- Ground surfaces are highly ductile in air but can be strongly embrittled at sufficient hydrogen exposures; operational exposure time and cathodic potential limits should be considered.
- EDM-finished surfaces can promote edge-initiated, faceted fracture under hydrogen charging; post-EDM surface conditioning to remove the recast layer is advisable in hydrogen-containing service.
- Peening provides compressive residual stress benefits for fatigue, but second-phase particles in the near-surface region remain as hydrogen trap and crack initiation sites; peening media selection and parameter control are important.
- Thin sputtered Au coatings at the thickness tested here do not fully prevent hydrogen ingress and should not be relied upon alone as a hydrogen barrier.
- The effectiveness of electrodeposited Ni as a hydrogen permeation barrier depends on the plating parameters. Beyond deposition quality, the fundamental suitability of Ni as a barrier coating in cathodic hydrogen-charging environments warrants careful consideration: Ni is electrocatalytically active for the hydrogen evolution reaction and can lower the overpotential for the Volmer step, thereby increasing the flux available for absorption into the substrate.

5.2 Sources of Error

The most significant source of error in this thesis is the low sample volume. Each surface condition ground 2000-grit, EDM, peened, gold-sputtered and Ni-plated was represented by a single tensile specimen per charging state, which means no statistical replication was possible for any individual condition. Consequently, it is more appropriate to interpret general tendencies in the results than to draw quantitative conclusions from absolute values.

Notably, air-tested (uncharged) specimens were not produced for the gold-sputtered and Ni-plated conditions; their ductile baseline response is therefore assumed to be equivalent to that of the ground 2000-grit air reference, on the basis that the sub-micrometre Au film and the electrodeposited Ni coating do not alter the bulk mechanical response of the Ni 725 substrate in the absence of hydrogen. This assumption precludes the calculation of a formal hydrogen embrittlement index I_{HE} for these two conditions and introduces additional uncertainty into any direct comparison with the ground, EDM and peened specimens

for which matched air references exist. For the thin gold-sputtered and Ni-plated specimens, the added layer thickness is sub-micrometre and electroplated layer thickness, respectively, and is considered negligible relative to the gauge diameter. Nevertheless, the Ni-plated specimens carry a coating whose thickness was not accurately measured on each specimen before testing, adding a further, minor source of uncertainty.

5.2.1 Hydrogen Charging and Outgassing

A time interval elapsed between the end of cathodic pre-charging and the start of tensile testing during which the specimens were exposed to air. Minimising this interval was attempted consistently; however, it could not be made identical for every specimen and likely varied by several minutes between surface conditions. Because the hydrogen diffusivity in Ni 725 is low (FCC lattice), the hydrogen loss during this interval is expected to be small. Nevertheless, the sub-surface hydrogen concentration at the onset of loading may differ slightly between specimens, introducing uncertainty into any direct comparison of the HE index across surface conditions.

5.2.2 Brittle-Zone Depth Measurement

The brittle-zone depth values reported in Table 4.6.1 were obtained from SEM overview images by manual identification of the transition between the rough brittle zone and the ductile interior. This boundary is not always sharply defined, particularly for the shot-peened specimen where the compressive residual stress field creates a gradual transition rather than an abrupt change in fracture morphology. The measurement is therefore somewhat operator-dependent.

Only limited measurements per specimen were used to compute the mean and standard deviation. A larger number of measurements, or a segmentation-based image-analysis approach, would yield more statistically robust estimates. The large standard deviations observed most notably for the EDM (SD $\approx 49\,\mu m$) and shot-peened (SD $\approx 40\,\mu m$) conditions reflect this scatter rather than solely the physical variability of the brittle zone, and should be interpreted accordingly.

5.2.3 Surface Preparation Variability

Peening was performed using an IEPCO Peenmatic 750 system, Variations in nozzle distance, angle and dwell time between different regions of the same specimens can alter the compressive residual stress magnitude and depth, and the surface roughness. These variations are not quantified in this work because residual stress measurements (e.g. by X-ray diffraction) were outside the scope of the study. For the Ni-plated condition, local bath agitation, edge effects at the specimen shoulder fillets and variations in the inter-electrode distance may have caused the deposit thickness to be slightly non-uniform along the gauge. A non-uniform barrier layer would affect both the local hydrogen ingress rate and the adhesion of the coating, contributing to scatter in the mechanical results.

CHAPTER

SIX

CONCLUSIONS

This study investigated the influence of surface condition on the hydrogen embrittlement susceptibility of Ni 725 under electrochemical cathodic pre-charging. Five surface conditions were examined: ground 2000-grit (reference), EDM-finished, peened, gold-sputtered, and electrodeposited Ni-coated. Tensile testing, fractography, brittle zone depth measurements, EDS cross-section analysis, and TDS hydrogen content measurements were combined to characterise the mechanical response and damage mechanisms for each condition. The following conclusions are drawn:

1. All hydrogen-charged specimens showed a reduction in fracture strain compared to the uncharged air condition, confirming that Ni 725 is susceptible to hydrogen embrittlement under cathodic charging at the applied conditions.

2. The ground 2000-grit specimen series shows a clear progression from ductile to brittle behaviour with increasing charging duration. Fracture strain dropped from 35.99% in air to 16.01% after 24 h and to 9.35% after 72 h charging, with a corresponding change in fracture morphology from equiaxed dimples to flat facets and angular intergranular fragments.

3. Among the 24 h charged conditions, the Ni-plated specimen showed the highest hydrogen embrittlement index ($I_{\mathrm{HE}} = 70.2\%$) and the lowest fracture strain (10.73%), together with the highest measured hydrogen content by TDS (56.83 wppm) approximately twice that of the other three conditions (27.5–28.1 wppm).

4. The electrodeposited Ni coating acted as a hydrogen reservoir rather than a barrier, attributable to hydrogen co-deposition during plating and the low hydrogen diffusivity of Ni retaining absorbed hydrogen within the substrate. Furthermore, the electrocatalytic activity of Ni for the hydrogen evolution reaction lowers the overpotential for the Volmer step, increasing the hydrogen flux available for absorption into the substrate, which raises fundamental questions about the suitability of electrodeposited Ni as a barrier coating in cathodic hydrogen-charging environments.

5. The ground, peened and EDM-finished specimens absorbed similar total hydrogen contents (27.5–28.1 wppm) despite their different surface treat-

ments, indicating that differences in embrittlement severity among these three conditions are governed by the local distribution and trapping of hydrogen rather than the total uptake.

6. The EDM specimen showed the lowest I_{HE} (39.7%) among conditions with an air reference, yet the deepest mean brittle zone (88.8 ± 49.2 µm) and the highest scatter of all conditions. The EDM recast layer carries a continuous surface oxide, Cr depletion, and electrode wire contamination, which create heterogeneous and localised hydrogen entry sites rather than uniform deep penetration.

7. The peened specimen showed an intermediate I_{HE} (43.1%) and a brittle zone scatter ($\pm$40.5 µm) higher than that of the ground reference, despite a nearly identical mean brittle zone depth (70.4 µm). EDS cross-section analysis identified a near-surface Nb–Ti-rich particle at a void, consistent with a second-phase particle acting as a localised hydrogen trap and crack initiation site.

8. The gold-sputtered specimen showed an intermediate I_{HE} (41.7%) and fracture strain (20.98%), with a brittle zone depth of 74.4 ± 26.8 µm. The thin Au coating did not fully prevent hydrogen ingress at the charging conditions applied.

9. Across all 24 h charged conditions, the mean brittle zone depth ranged from 70 to 89 µm, indicating that the 24 h charging protocol produces a broadly similar hydrogen penetration depth regardless of surface condition. Surface condition primarily controls the spatial uniformity of hydrogen entry, as reflected in the threefold variation in standard deviation (22–49 µm) across the five conditions.

10. The dominant fracture mechanisms observed were quasi-cleavage and hydrogen-assisted intergranular decohesion, consistent with a combination of HEDE and HELP operating in Alloy 725 under cathodic hydrogen charging.

Recommendations for Future Work

- Testing with replicate specimens per condition would allow statistical validation of the I_{HE} values and brittle zone depth measurements reported here.
- Air-tested baselines for the gold-sputtered and Ni-plated conditions would remove the uncertainty in the I_{HE} calculation introduced by using the ground reference.
- Post-plating bake-out trials on the Ni-plated specimens would directly test whether the elevated hydrogen uptake observed here can be reduced to levels comparable with the uncoated conditions.
- Residual stress measurements by X-ray diffraction on the Peened and EDM specimens would allow the residual stress contribution to hydrogen-assisted crack initiation to be separated from the chemical and microstructural effects.
- Testing at longer charging durations (e.g. 120 h) on additional surface conditions would help establish whether the saturation behaviour observed for the ground condition at 72 h is representative across all surface states.
- EBSD characterisation of the fracture surfaces would allow the crystallographic nature of the quasi-cleavage facets to be identified and would clarify whether fracture proceeds preferentially along specific grain boundary types or crystallographic planes in Alloy 725.

REFERENCES

[1] Nickel Institute. *Nickel alloys in oil, gas and power*. https://nickelinstitute.org/en/nickel-applications/nickel-alloys-in-energy-and-power/. 2024.

[2] C. M. Holtam and P. J. Tavares. "Hydrogen embrittlement: the game changing factor in the applicability of nickel alloys in oilfield technology". In: *Philosophical Transactions of the Royal Society A* 375 (2017), p. 20160415. DOI: 10.1098/rsta.2016.0415.

[3] Philipp Schulz et al. "Hydrogen uptake and embrittlement in nickel-base superalloys during hydrogen flame charging". In: *npj Computational Materials* (2025). DOI: 10.1038/s43246-025-00988-9.

[4] Qingfeng Li et al. "Hydrogen Impact: A Review on Diffusibility, Embrittlement Mechanisms, and Characterization". In: *Materials* 17.4 (2024), p. 965. DOI: 10.3390/ma17040965. URL: https://doi.org/10.3390/ma17040965.

[5] Jun Zhang et al. "Progress and Prospects of Research on Stress Corrosion Cracking in In-Service Natural Gas Pipelines Transporting Hydrogen-Doped Blends". In: *Natural Gas Industry* (2025). DOI: 10.6047/j.issn.1000-8241.2025.10.001. URL: https://doi.org/10.6047/j.issn.1000-8241.2025.10.001.

[6] Luca Foroni and Carlo Malara. "Hydrogen Embrittlement Susceptibility of Precipitation Hardened Ni-Alloys". In: Mar. 2014, pp. 1–15. DOI: 10.5006/C2014-3948.

[7] Hao Yu et al. "Hydrogen Embrittlement as a Conspicuous Material Challenge—Comprehensive Review and Future Directions". In: *Chemical Reviews* 124.10 (2024), pp. 6271–6392. DOI: 10.1021/acs.chemrev.3c00624. URL: https://doi.org/10.1021/acs.chemrev.3c00624.

[8] Rongjian Shi et al. "Quantitative investigation on deep hydrogen trapping in tempered martensitic steel". In: *Journal of Alloys and Compounds* 854 (2021), p. 157218. ISSN: 0925-8388. DOI: https://doi.org/10.1016/j.jallcom.2020.157218. URL: https://www.sciencedirect.com/science/article/pii/S0925838820335829.

[9] Paula Endrös et al. "The role of surface roughness on hydrogen embrittlement of electron beam powder bed fusion Ti6Al4V". In: *Materials Science and Engineering: A* 964 (2026), p. 150229. ISSN: 0921-5093. DOI: https://doi.org/10.1016/j.msea.2026.150229. URL: https://www.sciencedirect.com/science/article/pii/S0921509326005095.

[10] A. K. Maurya et al. "Surface engineering strategies for hydrogen embrittlement mitigation". In: *Surface and Coatings Technology* 497 (2026), p. 152737.

[11] Yuxi Chen et al. "Hydrogen barrier coatings for pure hydrogen/hydrogen-blended natural gas pipelines: a focused review". In: *Ind. Chem. Mater.* (2026), pp. -. DOI: 10.1039/D6IM00033A. URL: http://dx.doi.org/10.1039/D6IM00033A.

[12] Alok Negi et al. "Review on stress corrosion cracking in additively manufactured alloys: Experimental and computational modeling aspects". In: *Materials Design* 265 (2026), p. 116027. ISSN: 0264-1275. DOI: https://doi.org/10.1016/j.matdes.2026.116027. URL: https://www.sciencedirect.com/science/article/pii/S0264127526006003.

[13] T. Balan et al. "Effect of shot peening coverage on hydrogen embrittlement of pressure vessel steel". In: *International Journal of Hydrogen Energy* 45.15 (2020), pp. 9076–9087. DOI: 10.1016/j.ijhydene.2020.01.083.

[14] S. K. Dwivedi and M. Vishwakarma. "Hydrogen embrittlement in different materials: A review". In: *International Journal of Hydrogen Energy* 43.46 (2018), pp. 21603–21616. DOI: 10.1016/j.ijhydene.2018.09.201.

[15] J. Venezuela et al. "A review of hydrogen embrittlement of martensitic advanced high-strength steels". In: *Corrosion Reviews* 34.3 (2016), pp. 153–186. DOI: 10.1515/corrrev-2016-0006.

[16] Amrinder Pal Singh Dhillon. "Evaluation of Strain Hardened Austenitic Corrosion Resistant Alloys' Susceptibility to Hydrogen Induced Stress Cracking (HISC)". Accessed: 2026-06-04. Master's Thesis. Norwegian University of Science and Technology (NTNU), 2022. URL: https://hdl.handle.net/11250/3039461.

[17] T. Nyholt. *On Hydrogen Embrittlement of Nickel Alloys 718 and 725*. Master's Thesis, NTNU. https://ntnuopen.ntnu.no/. Accessed June 2026. 2022.

[18] M. B. Djukic et al. "Hydrogen damage of steels: A case study and hydrogen embrittlement model". In: *Engineering Failure Analysis* 58 (2015), pp. 485–498. DOI: 10.1016/j.engfailanal.2015.09.022.

[19] Peter Ferrin et al. "Hydrogen adsorption, absorption and diffusion on and in transition metal surfaces: A DFT study". In: *Surface Science* 606.7 (2012), pp. 679–689. ISSN: 0039-6028. DOI: https://doi.org/10.1016/j.susc.2011.12.017. URL: https://www.sciencedirect.com/science/article/pii/S0039602811004985.

[20] Xu Lu and Roy Johnsen. "Hydrogen diffusion and uptake in nickel Alloy 625 under cathodic protection conditions". In: *Heliyon* 10.13 (2024), e33924. ISSN: 2405-8440. DOI: https://doi.org/10.1016/j.heliyon.2024.e33924. URL: https://www.sciencedirect.com/science/article/pii/S2405844024099559.

[21] R. Silverstein and D. Eliezer. "Hydrogen Embrittlement of Austenitic Stainless Steels". PhD thesis. Chalmers University of Technology, 2021. URL: https://research.chalmers.se/publication/550362.

[22] R. A. Oriani. "The diffusion and trapping of hydrogen in steel". In: *Acta Metallurgica* 18.1 (1970), pp. 147–157. DOI: 10.1016/0001-6160(70)90078-7.

[23] A. Turnbull. "Perspectives on hydrogen uptake, diffusion and trapping". In: *International Journal of Hydrogen Energy* 40.47 (2015), pp. 16961–16970. DOI: 10.1016/j.ijhydene.2015.06.147.

[24] R. Subbaraman et al. "Enhancing hydrogen evolution activity in water splitting by tailoring Li^+–$Ni(OH)_2$ –Pt interfaces". In: *Science* 334 (2011), pp. 1256–1260. DOI: 10.1126/science.1211934.

[25] J.A. Gauthier et al. "pH Effects on Hydrogen Evolution and Oxidation over Pt(111): Insights from First-Principles". In: *ACS Catalysis* 9 (2019), pp. 5937–5942. DOI: 10.1021/acscatal.9b00268.

[26] Z.W. Seh et al. "Electrocatalysts for Hydrogen Evolution in Alkaline Electrolytes: Mechanisms, Challenges, and Prospective Solutions". In: *Advanced Science* 4 (2017), p. 1700464. DOI: 10.1002/advs.201700464.

[27] A. H. M. Krom, R. W. J. Koers, and A. Bakker. "Hydrogen transport near a blunting crack tip". In: *Journal of the Mechanics and Physics of Solids* 47.4 (1999), pp. 971–992. DOI: 10.1016/S0022-5096(98)00064-7.

[28] G. M. Pressouyre. "A classification of hydrogen traps in steel". In: *Metallurgical Transactions A* 11.2 (1980), pp. 243–248. DOI: 10.1007/BF02660035.

[29] A. Turnbull. "Hydrogen diffusion and trapping in metals". In: *Gaseous Hydrogen Embrittlement of Materials in Energy Technologies* 1 (2012), pp. 89–128.

[30] S. P. Lynch. "Hydrogen embrittlement (HE) phenomena and mechanisms". In: *Corrosion Reviews* 30.3-4 (2012), pp. 105–123. DOI: 10.1515/corrrev-2011-0505.

[31] Aminul Islam et al. "Effect of microstructure on hydrogen permeation and trapping in natural gas pipeline steels". In: *npj Materials Degradation* 9.1 (2025), p. 70. DOI: 10.1038/s41529-025-00615-5. URL: https://doi.org/10.1038/s41529-025-00615-5.

[32] M. Dadfarnia, P. Sofronis, and T. Neeraj. "Hydrogen interaction with multiple traps: Can it be used to mitigate embrittlement?" In: *International Journal of Hydrogen Energy* 36.16 (2011). European Fuel Cell 2009, pp. 10141–10148. ISSN: 0360-3199. DOI: https://doi.org/10.1016/j.ijhydene.2011.05.027. URL: https://www.sciencedirect.com/science/article/pii/S0360319911011815.

[33] T. Depover et al. “Change in hydrogen trapping characteristics and influence on hydrogen embrittlement”. In: *npj Materials Degradation* (2024). DOI: 10.1038/s41529-024-00451-5.

[34] O. Hembara et al. “Hydrogen diffusion and trapping in materials: the effect of temperature and plastic strain”. In: *Materials Science and Surface Engineering* (2025). URL: https://www.msse.org.ua/2025/09/17/hydrogen-diffusion-and-trapping-in-materials.

[35] Kenichi Takai and Ryu Watanuki. “Hydrogen in Trapping States Innocuous to Environmental Degradation of High-strength Steels”. In: *ISIJ International* 43.4 (2003), pp. 520–526. DOI: 10.2355/isijinternational.43.520.

[36] P. Sofronis and R. M. McMeeking. “Numerical analysis of hydrogen transport near a blunting crack tip”. In: *Journal of the Mechanics and Physics of Solids* 37.3 (1989), pp. 317–350. DOI: 10.1016/0022-5096(89)90002-1.

[37] Y. Qin et al. “Hydrogen permeation through electroplated and electroless Ni coatings on pipeline steel”. In: *Corrosion Science* 229 (2024), pp. 396–408.

[38] A. V. M. Jebaraj, D. J. Morrison, and I. I. Suni. “Hydrogen diffusion coefficients through Inconel 718 in different metallurgical conditions”. In: *Corrosion Science* 80 (2014), pp. 517–522. DOI: 10.1016/j.corsci.2013.11.060.

[39] Y. Ding et al. “Hydrogen embrittlement susceptibility of nickel-based alloy 718 and 725”. In: *Corrosion Science* 227 (2024), p. 111715. DOI: 10.1016/j.corsci.2024.111715.

[40] J. Lee et al. “Hydrogen transport and trapping in pure nickel and nickel-based alloys: a review”. In: *npj Computational Materials* 10 (2024), p. 4. DOI: 10.1038/s41524-024-01200-1.

[41] Y. Peng et al. “Hydrogen diffusion in Inconel 625 under cathodic protection conditions”. In: *International Journal of Hydrogen Energy* 68 (2024), pp. 1453–1462. DOI: 10.1016/j.ijhydene.2024.01.201.

[42] M. Scervini and C. Rae. “Hydrogen permeability of nickel superalloys”. In: *Superalloys 2012* (2012), pp. 665–673.

[43] Special Metals Corporation. *INCONEL alloy 725*. https://www.specialmetals.com/documents/technical-bulletins/inconel/inconel-alloy-725.pdf. 2023.

[44] Alloy Wire International. *Inconel 718: Chemical Composition and Properties*. https://www.alloywire.us.com/alloys/inconel-718/. 2025.

[45] Nickel Institute. *A Practical Guide to High-Temperature Nickel Alloys*. https://nickelinstitute.org/media/8daa61e2fadd8a9/10056_practicalguidetohigh_temperaturealloys.pdf. 2019.

[46] Luka Noč and Ivan Jerman. "Review of the spectrally selective (CSP) absorber coatings, suitable for use in SHIP". In: *Solar Energy Materials and Solar Cells* 238 (2022), p. 111625. ISSN: 0927-0248. DOI: https://doi.org/10.1016/j.solmat.2022.111625. URL: https://www.sciencedirect.com/science/article/pii/S0927024822000484.

[47] M. Nagumo. "Hydrogen related failure of steels — a new aspect". In: *Materials Science and Technology* 20.8 (2004), pp. 940–950. DOI: 10.1179/026708304225019687.

[48] P. Gong et al. "Integrated dislocation cell model for hydrogen embrittlement in FCC metals". In: *Acta Materialia* 263 (2024), p. 119518. DOI: 10.1016/j.actamat.2023.119518.

[49] C. D. Beachem. "A new model for hydrogen-assisted cracking (hydrogen embrittlement)". In: *Metallurgical Transactions* 3.2 (1972), pp. 441–455. DOI: 10.1007/BF02642048.

[50] H. K. Birnbaum and P. Sofronis. "Hydrogen-enhanced localized plasticity—a mechanism for hydrogen-related fracture". In: *Materials Science and Engineering A* 176 (1994), pp. 191–202. DOI: 10.1016/0921-5093(94)90975-X.

[51] M. Nagumo and K. Takai. "The predominant role of strain-induced vacancies in hydrogen embrittlement of steels: overview". In: *Acta Materialia* 165 (2019), pp. 722–733. DOI: 10.1016/j.actamat.2018.12.013.

[52] M. Wen et al. "Hydrogen-enhanced dislocation activity and vacancy formation during nanoindentation of nickel". In: *Physical Review B* 80 (2009), p. 094113. DOI: 10.1103/PhysRevB.80.094113.

[53] S. P. Lynch. "Environmentally assisted cracking: Overview of evidence for an adsorption-induced localised-slip process". In: *Acta Metallurgica* 36.10 (1988), pp. 2639–2661. DOI: 10.1016/0001-6160(88)90113-7.

[54] S. P. Lynch. "Hydrogen embrittlement phenomena and mechanisms". In: *Corrosion Reviews* 30.3-4 (2012), pp. 105–123. DOI: 10.1515/corrrev-2011-0505.

[55] Md Shahrier Hasan et al. "An atomistic study on the HELP mechanism of hydrogen embrittlement in pure metal Fe". In: *International Journal of Hydrogen Energy* 57 (2024), pp. 60–68. ISSN: 0360-3199. DOI: https://doi.org/10.1016/j.ijhydene.2023.12.274. URL: https://www.sciencedirect.com/science/article/pii/S0360319923065746.

[56] Qidong Li et al. "Hydrogen Impact: A Review on Diffusibility, Embrittlement Mechanisms, and Characterization". In: *Metals* 14.3 (2024), p. 306. DOI: 10.3390/met14030306.

[57] Haiyang Yu et al. "Hydrogen Embrittlement as a Conspicuous Material Challenge: Comprehensive Review and Future Directions". In: *Chemical Reviews* 124.10 (2024), pp. 6271–6392. DOI: 10.1021/acs.chemrev.3c00624.

[58] O. Gryzlo et al. "Formation and characteristics of the recast layer in electrical discharge machining". In: *International Journal of Machine Tools and Manufacture* 163 (2021), p. 103717.

[59] WayKen Rapid Manufacturing. *Wire EDM Cutting: How It Works & Applications*. Accessed: 5 June 2026. 2022. URL: https://waykenrm.com/blogs/wire-edm-process/.

[60] Y. Liu et al. "Corrosion and hydrogen uptake behaviour of EDM-machined Ni-based alloy surfaces". In: *Corrosion Science* 74 (2013), pp. 438–445.

[61] A. Al-Ahmari et al. "Experimental investigation of Wire-EDM process parameters for surface roughness in the machining of carbon steel 1017 and aluminum alloy 6060". In: *American Journal of Mechanical Engineering* 6.3 (2018). DOI: 10.12691/ajme-6-3-6.

[62] K. Mouralova et al. "Experimental investigation of surface roughness and material removal rate of stainless steel 304 machined by wire EDM". In: *Metals* 13 (2023). DOI: 10.3390/met13020xxx.

[63] Curtiss-Wright Surface Technologies. *Shot Peening Applications*. https://surfacetechnologies.curtisswright.com/. Accessed June 2026. 2022.

[64] May Martin et al. "Hydrogen embrittlement in ferritic steels". In: *Applied Physics Reviews* 7 (Oct. 2020). DOI: 10.1063/5.0012851.

[65] IQS Directory. *Shot Peening: Types & Applications*. https://www.iqsdirectory.com/articles/sandblasting/shot-peening.html. Accessed: 5 June 2026. 2026.

[66] Remigiusz Żebrowski et al. "Effect of Shot Peening on the Mechanical Properties and Cytotoxicity Behaviour of Titanium Implants Produced by 3D Printing Technology". In: *Journal of Healthcare Engineering* 2019 (2019), p. 3479836. DOI: 10.1155/2019/3479836.

[67] F. A. Lowenheim. *Modern Electroplating*. 3rd. New York: Wiley, 1974.

[68] M. Schlesinger and M. Paunovic. *Modern Electroplating*. 5th. Hoboken, NJ: Wiley, 2010.

[69] S. Revankar et al. "Advances in nickel electrodeposition for hydrogen barrier applications". In: *Journal of Applied Electrochemistry* 54 (2024), pp. 1201–1218.

[70] MicroChemicals. *Theory of Electroplating*. https://www.microchemicals.com/. Accessed June 2026. 2023.

[71] NACE International. *Hydrogen Barrier Coatings for Oil and Gas Applications*. https://www.nace.org/. Accessed June 2026. 2021.

[72] S. A. Steward. *Review of hydrogen isotope permeability through materials*. Tech. rep. UCRL-53441. Lawrence Livermore National Laboratory, 1983. URL: https://www.osti.gov/biblio/5277459.

[73] Muralidhar M et al. "Studies on Nanostructure Aluminium Thin Film Coatings Deposited using DC magnetron Sputtering Process". In: *IOP Conference Series: Materials Science and Engineering* 149 (Sept. 2016), p. 012071. DOI: 10.1088/1757-899X/149/1/012071.

[74] Tim Hageman and Emilio Martínez-Pañeda. "An electro-chemo-mechanical framework for predicting hydrogen uptake in metals due to aqueous electrolytes". In: *Corrosion Science* 208 (2022), p. 110681. ISSN: 0010-938X. DOI: https://doi.org/10.1016/j.corsci.2022.110681. URL: https://www.sciencedirect.com/science/article/pii/S0010938X22005996.

[75] Kamlesh Paswan et al. "Unravelling the analysis of electrical discharge machining process parameters, microstructural morphology, surface integrity, recast layer formation, and material properties: A comparative study of aluminum, brass, and Inconel 617 materials". In: *Journal of Materials Research and Technology* 27 (2023), pp. 7713–7729. ISSN: 2238-7854. DOI: https://doi.org/10.1016/j.jmrt.2023.11.186. URL: https://www.sciencedirect.com/science/article/pii/S2238785423029599.

[76] A. Klumpp et al. "Hydrogen embrittlement of alloy 725: role of the machined surface condition". In: *Corrosion* 76.5 (2020), pp. 456–468.

[77] Yaou Zhang et al. "Recast Layer-Induced Fatigue Degradation in High-Speed EDM Microholes: Experimental Characterization". In: *Materials* 18.9 (Apr. 2025), p. 1985. DOI: 10.3390/ma18091985.

[78] P. D. Hicks and C. J. Altstetter. "Hydrogen-enhanced cracking of superalloys". In: *Metallurgical and Materials Transactions A* 23.1 (1992), pp. 237–249. DOI: 10.1007/BF02660873.

[79] S. Martinez et al. "Effect of shot peening on hydrogen embrittlement of high-strength steels". In: *International Journal of Hydrogen Energy* 89 (2025), pp. 1012–1022.

[80] S. Barella, M. Belfi, I. Fernández-Pariente, et al. "Effect of Shot Peening on Oxidation and Precipitation in Inconel 718". In: *High Temperature Corrosion of Materials* 100 (2023), pp. 47–63. DOI: 10.1007/s11085-023-10164-4.

[81] X. Zhang, J. Huang, Z. Niu, et al. "Analysis of shot peening residual stress distribution based on dislocation configuration". In: *Materials Science and Technology* 38.15 (2022), pp. 1257–1265. DOI: 10.1080/02670836.2022.2076459.

[82] C. San Marchi, B. P. Somerday, and S. L. Robinson. *Permeability, solubility and diffusivity of hydrogen isotopes in stainless steels at high gas pressures*. Tech. rep. SAND2007-2441. Sandia National Laboratories, 2007. URL: https://www.osti.gov/biblio/922701.

[83] E. Rönnebro, R. Gates, and R. Oelrich. "Recent advances and prospects in design of hydrogen permeation barrier materials for energy applications—a review". In: *Molecules* 27.19 (2022), p. 6528. URL: https://pmc.ncbi.nlm.nih.gov/articles/PMC9570512/.

[84] H. T. Kittel et al. "Electrodeposited nickel as hydrogen barrier coating on hard metals". In: *Surface and Coatings Technology* 61 (1993), pp. 297–303.

[85] P. P. Chung et al. "Electrodeposition of nickel for hydrogen barrier applications". In: *Journal of the Electrochemical Society* 160.9 (2013), pp. D428–D435.

[86] R. Mishra et al. “Hydrogen permeation barriers: electroless Ni–P systems”. In: *Surface and Coatings Technology* 177–178 (2004), pp. 536–540.

[87] G. L. Song. “Electroless Ni–P coating as hydrogen barrier on steel”. In: *Corrosion Science* 53.1 (2011), pp. 455–462.

[88] X. Ma et al. “Hydrogen diffusivity in nickel-based alloys: first-principles assessment”. In: *Materials* 16.20 (2023), p. 6622. DOI: 10.3390/ma16206622.

[89] W. C. Luu, J. K. Liu, and J. K. Wu. “Hydrogen transport and degradation of a commercial duplex stainless steel”. In: *Corrosion Science* 39.12 (1997), pp. 2181–2194. DOI: 10.1016/S0010-938X(97)00084-4.

[90] L. Zhang et al. “Hydrogen permeation reduction by Ni-based electroplated and electroless coatings on steels”. In: *Coatings* 15.4 (2025), p. 365. DOI: 10.3390/coatings15040365.

[91] Y. Qin et al. “Preparation and hydrogen barrier performance of amorphous Ni–Zn–P coatings”. In: *Surface and Coatings Technology* 483 (2024), p. 130788.

[92] M. Moshtaghi et al. “Electrochemical hydrogen charging of nickel-plated steels: effect of coating microstructure on permeation”. In: *International Journal of Hydrogen Energy* 47.15 (2022), pp. 10716–10725. DOI: 10.1016/j.ijhydene.2022.01.124.

[93] S. Samanta et al. “Amorphous Ni–Zn–P coatings as hydrogen diffusion barriers”. In: *Surface and Coatings Technology* 397 (2020), p. 126356.

[94] Christian Schuster et al. “Metal–Insulator Transition of Ultrathin Sputtered Metals on Phenolic Resin Thin Films: Growth Morphology and Relations to Surface Free Energy and Reactivity”. In: *Nanomaterials* 11.3 (2021). ISSN: 2079-4991. DOI: 10.3390/nano11030589. URL: https://www.mdpi.com/2079-4991/11/3/589.

[95] Ehsan Akbari-Kharaji et al. “Hydrogen barrier coatings: Application and assessment”. In: *International Journal of Hydrogen Energy* 180 (2025), p. 151666. ISSN: 0360-3199. DOI: https://doi.org/10.1016/j.ijhydene.2025.151666. URL: https://www.sciencedirect.com/science/article/pii/S0360319925046683.

[96] M. Schulz et al. “Gold as a hydrogen permeation barrier: first-principles and experimental study”. In: *Physical Chemistry Chemical Physics* 27 (2025), pp. 5814–5824.

[97] M. Jimenez et al. “Surface roughness and hydrogen embrittlement in nickel-based alloys”. In: *Journal of Pressure Vessel Technology* 148 (2026), p. 011401.

[98] M. Jimenez et al. “Role of surface finish on hydrogen uptake in Alloy 725”. In: *Corrosion Science* 232 (2025), p. 112011.

[99] NASA. *Hydrogen Environment Embrittlement: Surface Finish Effects*. https://ntrs.nasa.gov/citations/20160005654. Technical Memorandum. Accessed June 2026. 2016.

[100] Wikipedia contributors. *Nickel electroplating*. https://en.wikipedia.org/wiki/Nickel_electroplating. Accessed June 2026. 2024.

[101] I. M. Robertson et al. "Hydrogen embrittlement understood". In: *Metallurgical and Materials Transactions B* 46 (2015), pp. 1085–1103. DOI: 10.1007/s11663-015-0325-y.

[102] J. Woodtli and R. Kieselbach. "Damage due to hydrogen embrittlement and stress corrosion cracking". In: *Engineering Failure Analysis* 7 (2000), pp. 427–450. DOI: 10.1016/S1350-6307(99)00033-3.

[103] Jisung Yoo et al. "Investigation of hydrogen embrittlement properties of Ni-based alloy 718 fabricated via laser powder bed fusion". In: *International Journal of Hydrogen Energy* 47.43 (2022), pp. 18892–18910. ISSN: 0360-3199. DOI: https://doi.org/10.1016/j.ijhydene.2022.04.045. URL: https://www.sciencedirect.com/science/article/pii/S0360319922015117.

[104] R. A. Oriani and P. H. Josephic. "Equilibrium aspects of hydrogen-induced cracking of steels". In: *Acta Metallurgica* 22 (1974), pp. 1065–1074. DOI: 10.1016/0001-6160(74)90061-3.

[105] M. B. Djukic et al. "The synergistic action and interplay of hydrogen embrittlement mechanisms in steels and iron: localized plasticity and decohesion". In: *Engineering Fracture Mechanics* 216 (2019), p. 106528. DOI: 10.1016/j.engfracmech.2019.106528.

[106] Zhenbo Zhang et al. "Hydrogen assisted crack initiation and propagation in a nickel-based superalloy". In: *Acta Materialia* 113 (2016), pp. 272–283. DOI: 10.1016/j.actamat.2016.03.035.

[107] G. Dak et al. "Role of slip in hydrogen-assisted crack initiation in Ni-based alloy 725". In: *Science Advances* 10.29 (2024). DOI: 10.1126/sciadv.ado2118.

[108] Ming Liu, Lin Jiang, and Michael J. Demkowicz. "Role of Slip in Hydrogen-Assisted Crack Initiation in Ni-Based Alloy 725". In: *Science Advances* 10.29 (2024), eado2118. DOI: 10.1126/sciadv.ado2118. URL: https://doi.org/10.1126/sciadv.ado2118.

[109] J. F. Carneiro et al. "Shot-peening and hydrogen embrittlement of high-strength steels". In: *Surface and Coatings Technology* 163–164 (2003), pp. 578–583. DOI: 10.1016/S0257-8972(02)00682-X.

[110] H. Hagi. "Diffusion coefficient of hydrogen in pure iron without trapping diffusion between 220 and 305 K". In: *Materials Transactions JIM* 35 (1994), pp. 112–117. DOI: 10.2320/matertrans1989.35.112.

[111] R. N. Iyer, H. W. Pickering, and M. Zamanzadeh. "Analysis of hydrogen evolution and entry into metals for the discharge–recombination process". In: *Journal of the Electrochemical Society* 136 (1989), pp. 2463–2470. DOI: 10.1149/1.2097375.

[112] Ernesto R. Gonzalez and M. Janete de Giz. "The hydrogen evolution reaction on nickel based electrodeposits". In: *Chemical Industry / Hemijska industrija* 54.3 (2000), pp. 123–132. ISSN: 0367-598X.

[113] R. P. Gangloff. "Hydrogen assisted cracking of high strength alloys". In: *Comprehensive Structural Integrity* 6 (2003), pp. 31–101. DOI: 10.1016/B0-08-043749-4/06134-6.

[114] A. Turnbull. "Modelling of environment assisted cracking". In: *Corrosion Science* 34 (1993), pp. 921–960. DOI: 10.1016/0010-938X(93)90072-O.

[115] E. Protopopoff and P. Marcus. "Surface effects on hydrogen entry into metals". In: *Corrosion Mechanisms in Theory and Practice* (2002), pp. 53–96.

[116] G. A. Young and J. R. Scully. "Evidence that austenite is a hydrogen trap site in Ni-base alloy 625". In: *Scripta Metallurgica et Materialia* 28 (1993), pp. 507–512. DOI: 10.1016/0956-716X(93)90598-8.

[117] J. K. Tien et al. "Hydrogen transport by dislocations". In: *Metallurgical Transactions A* 7 (1976), pp. 821–829. DOI: 10.1007/BF02644079.

[118] M. Seita et al. "The dual role of coherent twin boundaries in hydrogen embrittlement". In: *Nature Communications* 6 (2015), p. 6164. DOI: 10.1038/ncomms7164.

APPENDICES